
Isogeometric Analysis for Scaled Boundary Parametrizations

Clarissa Arioli

Vom Fachbereich Mathematik der Technischen Universität Kaiserslautern zur
Verleihung des akademischen Grades

Doktor der Naturwissenschaften
(Doctor rerum naturalium, Dr. rer. nat.)

genehmigte Dissertation.

1. Gutachter: Prof. Dr. Bernd Simeon, Technische Universität Kaiserslautern
2. Gutachter: Prof. Dr. Matthias Möller, Technische Universität Delft

Datum der Disputation: 25. August 2020

Abstract

In this thesis, we present the basic concepts of isogeometric analysis (IGA) and we consider Poisson's equation as model problem. Since in IGA the physical domain is parametrized via a geometry function that goes from a parameter domain, e.g. the unit square or unit cube, to the physical one, we present a class of parametrizations that can be viewed as a generalization of polar coordinates, known as the scaled boundary parametrizations (SB-parametrizations). These are easy to construct and are particularly attractive when only the boundary of a domain is available. We then present an IGA approach based on these parametrizations, that we call scaled boundary isogeometric analysis (SB-IGA). The SB-IGA derives the weak form of partial differential equations in a different way from the standard IGA. For the discretization projection on a finite-dimensional space, we choose in both cases Galerkin's method. Thanks to this technique, we state an equivalence theorem for linear elliptic boundary value problems between the standard IGA, when it makes use of an SB-parametrization, and the SB-IGA. We solve Poisson's equation with Dirichlet boundary conditions on different geometries and with different SB-parametrizations.

Zusammenfassung

In dieser Arbeit stellen wir die Grundkonzepte der isogeometrischen Analysis (IGA) vor und betrachten die Poisson-Gleichung als Modellproblem. Da in IGA das physikalische Gebiet über eine Geometriefunktion parametrisiert wird, die von einem Parametergebiet (z.B. dem Einheitsquadrat oder -würfel) in das physikalische Gebiet abbildet, präsentieren wir eine Klasse von Parametrisierungen, die als Verallgemeinerung von Polarkoordinaten angesehen werden können, die *scaled boundary* Parametrisierungen (SB-Parametrisierungen). Diese sind einfach zu konstruieren und besonders attraktiv, wenn nur der Rand eines Gebietes verfügbar ist. Wir präsentieren weiterhin einen IGA-Ansatz, der auf diesen Parametrisierungen basiert und den wir als *scaled boundary* IGA (SB-IGA) bezeichnen. Die SB-IGA leitet die schwache Formulierung anders her als die Standard-IGA. Für die Diskretisierungsprojektion auf einen endlich-dimensionalen Raum wählen wir in beiden Ansätzen die Galerkin-Methode. Auf diese Weise erhalten wir für lineare elliptische Randwertprobleme ein Äquivalenztheorem zwischen dem Standard-IGA, wenn eine SB-Parametrisierung verwendet wird, und dem SB-IGA an. Wir lösen die Poisson-Gleichung mit Dirichlet-Randbedingungen auf verschiedenen Geometrien und mit verschiedenen SB-Parametrisierungen.

In memory of my grandmother Pasqua and my friend Pietre

Acknowledgments

I want to acknowledge the support by the German Research Council (DFG) under grant no. SI 756/5-1.

First I want to express my gratitude to my supervisor Professor Bernd Simeon, for his patient guidance and for giving me the opportunity to write this thesis. His helpful ideas and his encouragement made this dissertation possible.

Within the DFG project I had the possibility of collaborating with Margarita Chasapi and Professor Sven Klinkel. Thank you for having hosted me at RWTH Aachen.

Furthermore, I want to thank Professor Matthias Möller for serving as a referee for this thesis.

I would also like to thank all my former and present colleagues: Alexander Shaman-skiy, Felix Dietrich, Mané Harutyunyan, Steffen Plunder, Michael Gfrerer, Jiarui Yu and Dennis Merkert. It was a pleasure to work and discuss with all of you, thanks also to the positive working atmosphere. I would like to acknowledge Benjamin Bauer for his precious help with the ISOGAT code. Special thanks to Jonathan Jahnke, Felix Dietrich and Vishnupriya Anupindi for proof-reading.

For the balancing distraction and fun I needed during my PhD, I am very thankful to the modern choir of TU Kaiserslautern “Haste Töne” and to the scuba diving group. Singing and playing underwater rugby relaxed my body and soul.

An enormous *grazie* to the most important people in my life. To all my family, my parents Marco and Silvia and my sisters Fabiola and Marianna. Their encouragement and support is limitless. To my boyfriend Davide, for proof-reading and commenting the thesis, for his constant support, even if far away. A shoulder to lean on whenever I am feeling hopeless and confused. I am really indebted to him.

“In case I don’t see ya, good afternoon, good evening and good night.”
Truman Burbank

Contents

Symbols	xi
Acronyms and Abbreviations	xii
1 Introduction	1
Structure of the Thesis	3
2 Foundations from Computational Geometry	5
2.1 B-Splines	6
2.1.1 Definition and Properties of B-Spline Basis Functions	6
2.1.2 B-Spline Geometries	9
2.2 NURBS	11
2.3 Refinements	12
3 Isogeometric Analysis	19
3.1 Strong and Weak Form of a Boundary Value Problem	19
3.1.1 Galerkin's Method	21
3.2 The Geometry Function	22
3.2.1 Assembling the System	24
3.2.2 A Priori Error Estimates	25
3.3 Examples	26
3.3.1 L-Shape	26
3.3.2 Unit Disk	28
4 Scaled Boundary Isogeometric Analysis	35
4.1 Scaled Boundary Parametrizations	35
4.2 Scaled Boundary IGA and Galerkin-Based IGA	39
4.2.1 Galerkin-Based IGA	41
4.2.2 Scaled Boundary IGA	42
4.2.3 Equivalence Theorem	44
4.3 The Singularity in the Scaling Center	46
4.4 Examples	48
4.4.1 Unit Disk	48
4.4.2 L-Shape	55
4.4.3 Wedge-Shape	62
4.4.4 Summary	70

5	Conclusion	71
----------	-------------------	-----------

Symbols

\mathcal{C}^p	continuously differentiable functions
p, q	degree
m, n	dimension of a spline space
Ξ, H	knot vector
ξ_i, η_j	knot in knot vector
$M_{i,p}(\xi)$	B-spline basis function, nonrational, Definition 2.1
$N_{j,q}(\eta)$	B-spline basis function, nonrational
$R_{i,p}(\xi)$	B-spline basis function, rational: NURBS, Definition 2.10
ω_i	NURBS weight
$\mathcal{S}(\Xi, p)$	B-spline space, Definition 2.3
γ	B-spline curve, Definition 2.6
\mathbf{c}_i	control point forming a control polygon
$\bar{\mathbf{c}}_i$	control point of the control polygon after the refinement
α_i	coefficients for determining $\bar{\mathbf{c}}_i$ after knot insertion, Equation (2.6b)
$\mathbf{\Gamma}$	B-spline surface, Definition 2.9
$\mathbf{d}_{i,j}$	control point forming a control net
$\bar{\mathbf{d}}_{i,j}$	control point of the control net after the refinement
Ω	physical domain
$\partial\Omega$	boundary of Ω
$\partial\Omega_D$	subset of $\partial\Omega$ with Dirichlet boundary conditions, Equation (3.1b)
$\partial\Omega_N$	subset of $\partial\Omega$ with Neumann boundary conditions, Equation (3.1c)
Ω_0	parameter domain
$\hat{}$	something defined on Ω_0
\mathbf{x}	set of coordinates in Ω
$\boldsymbol{\xi}$	set of coordinates in Ω_0
d	dimension of geometry $\Omega \subset \mathbb{R}^d$, usually $d = 1, 2, 3$
g_D, g_N	boundary conditions, Dirichlet and Neumann, Remark 3.2
u	unknown solution of boundary value problem
L	operator acting on u
f	source term
v	test function
a	bilinear form associated to the operator L
l	linear form defined as the standard L^2 -scalar product
\mathcal{V}	Hilbert space where the test functions live, Definition 3.4
\mathcal{V}_h	finite-dimensional space, Equation (3.5)

\cdot_h	discretization of \cdot in \mathcal{V}_h
ϕ_i	basis functions for \mathcal{V}_h
ψ_i	basis functions for $\hat{\mathcal{V}}_h$
$\mathbf{A}, A_{i,j}$	stiffness matrix and one of its element
\mathbf{u}, u_i	vector of solution coefficients and one of its element
\mathbf{r}, r_i	right-hand side vector and one of its element
\mathbf{F}	geometry function from Ω_0 to Ω , Equation (3.8)
\mathbf{DF}	Jacobian of \mathbf{F}
$J(\eta)$	part of determinant of \mathbf{DF} depending only on η , Equation (4.11)
$\Pi_k u$	optimal interpolate, Equation (3.25)
C	constant for the error estimates, Equation (3.25)
h	discretization scale, Equation (3.27)
\mathbf{x}_0	scaling center in SB-IGA
$x_{0,1}, x_{0,2}$	first and second coordinates of \mathbf{x}_0
\mathbf{C}	matrix containing \mathbf{c}_i in SB-IGA, Equation (4.4)
$\mathbf{C}_1, \mathbf{C}_2$	first and second rows of \mathbf{C}
$\mathbf{N}(\eta)$	vector containing $N_{j,q}(\eta)$ in SB-IGA, Equation (4.4)
$\mathbf{N}'(\eta)$	derivative of $\mathbf{N}(\eta)$ with respect to η
\mathbf{g}	metric tensor of first fundamental form, Equation (4.12)
$\mathbf{b}_1, \mathbf{b}_2$	Equation (4.17)
$U_{i,j}$	solution coefficients for $\hat{u}_h(\xi, \eta)$, Equation (4.20)
$\mathbf{U}(\xi), \mathbf{V}$	Equation (4.25)
$\mathbf{E}, \mathbf{G}, \mathbf{K}, \mathbf{S}(\xi)$	Equation (4.28)
$\mathbf{W}(\xi)$	test function in ξ , Equation (4.31)
$\mathbf{y}(\xi), \mathbf{Z}$	Equation (4.38)
\mathbf{H}	Hamiltonian matrix, Equation (4.40)
\mathbf{J}	skew-symmetric matrix, Equation (4.41)
\mathbf{I}_n	n -by- n identity matrix
λ_i, Φ_i	eigenvalue and corresponding eigenvector of \mathbf{H}
q_r, w_r	quadrature points and weights, Equations (4.44),(4.45)

Acronyms and Abbreviations

NURBS	NonUniform Rational B-Splines
CAGD	Computer-Aided Geometric Design
IGA	IsoGeometric Analysis
FEM	Finite Element Method
PDE	Partial Differential Equation
ODE	Ordinary Differential Equation
DoF	Degrees of Freedom
SB-parametrization	Scaled Boundary parametrization
SB-IGA	Scaled Boundary IsoGeometric Analysis
SB-FEM	Scaled Boundary Finite Element Method
B-Rep	Boundary Representation

Introduction

The finite element method (FEM) is one of the most popular numerical methods used to find approximate solutions of partial differential equations (PDEs), such as the heat transfer equation, the equations of linear elasticity and the Navier-Stokes equations. This technique discretizes the geometry into smaller sub-geometries called elements. However, the geometry considered by the FEM is an approximation of the one given by a computer-aided geometric design (CAGD). Such an approximation affects the accuracy of the solution and leads to various numerical errors.

To minimize the discretization error, various attempts have been made in past, for example in [36] a B-spline finite element approach has been presented, and in [16] Cirak et al. considered a subdivision surface scheme to model thin shell geometries in the finite element framework. With the motivation to combine the CAGD geometries with the simulation approaches, Hughes et al. [32] introduced a new numerical method, known as the isogeometric analysis (IGA).

As the name itself suggests, this technique provides an analysis framework for the geometry generated by a CAGD, without making any geometrical approximation. Usually, the geometries in CAGD are described with nonuniform rational B-spline (NURBS) basis functions. The concept of IGA is to utilize the same NURBS functions when solving the equation numerically, i.e. they are considered as basis for the finite-dimensional space. Since its appearance, IGA has been successfully applied to a variety of problems, e.g. fluid-structure interactions [8, 30], electromagnetics [44, 64], mechanical analysis of solids [23, 32] and structures [18, 37, 68], and shape optimization problems [25, 65, 67]. At the same time the concept of IGA has already been implemented using several numerical discretization methods, such as collocation [3], boundary elements [53], finite volumes [30] and, of course, isogeometric finite elements [32].

Apart from the inclusion of NURBS basis functions for the modeling and analysis in IGA, other CAGD tools have been employed, for instance, T-splines [7], hierarchical splines [62], locally refined B-splines [29], PHT-splines [66]. Furthermore, in 3D computer graphics, smooth surfaces can also be represented through a subdivision surface. Indeed, starting from a coarse polygon mesh, a smooth surface can be calculated as the limit of an iterative process that subdivides each polygonal face into smaller faces that better approximate the smooth surface. Subdivision surfaces offer great flexibility in capturing irregular topologies with high order smoothness. For this reason, they are frequently used in geometric modeling and recently in IGA as well. In the literature, we can find isogeometric analysis based on the Catmull-Clark subdivision scheme [4, 46] or on Loop's subdivision scheme [34, 45].

Another challenge in the IGA community is the development of analysis-suitable parametrizations of the computational domain. Indeed, the accuracy of the analysis is affected by the quality of the parametrization. In [70], they present a parametrization of the computational domain by a planar B-spline surface from the given CAGD object (four boundary planar B-spline curves). When the boundaries are more complex a possible planar parametrization can be found in [69]. Several linear and nonlinear parametrization methods can be found in [28]. Recently, a parametrization inspired by large elastic deformation has been proposed in [52], where the desired domain is modeled as a deformed configuration of an initial simple geometry.

In this thesis, we investigate a special class of parametrizations that can be viewed as generalizations of classical polar coordinates, the so-called scaled boundary parametrizations (SB-parametrizations). These are easy to construct and are particularly attractive when only a boundary description of the computational domain is available. Given the boundary of a star-shaped domain, first we pick a point, the scaling center, inside the kernel of the domain, where the kernel is the set of all points from which the entire boundary is visible. Then, a set of rays is constructed from the scaling center to the boundary. The SB-parametrization presents two directions, the angular and the scaling ones. As the names suggest, the first spans the angles formed by the rays, while the second spans the distance from the scaling center to the boundary. We will focus on standard Galerkin-based IGA in combination with such parametrizations and we will address its connection to the scaled boundary IGA (SB-IGA).

The idea of the SB-IGA goes back to the scaled boundary finite element method (SB-FEM) [55, 56]. The main differences to standard Galerkin-based IGA are in the derivation of the weak form of a problem and in the usage of the parametrization. Indeed, instead of deriving the weak form in one step, the SB-IGA derives the weak form first in the angular direction and then also in the scaling direction. Moreover, these weak forms are derived directly on the parameter domain given by the scaled boundary parametrizations and not on the physical domain, as in the other approach. By means of the Laplace-Beltrami operator, it is possible to derive an equivalence of the weak forms of these two approaches for linear problems.

The scaled boundary parametrizations have two drawbacks; namely, they can only be applied to star-shaped domains and they have a singularity in the scaling center. The first disadvantage can be overcome by dividing the domain into subdomains such that each of them is star-shaped. The domain decomposition can be done with different techniques. For example, in [5] the creation of star-shaped subdomains is proposed via two different decompositions, the first based on the quadtree approach and the second on the art gallery problem. Another possibility could be to increase the flexibility of polar parametrization using circular arcs to connect the center with the points on the boundary, as proposed in [35]. In this work we investigate the singularity in the scaling center. Moreover, in the numerical solutions, we do not notice any singularity when an appropriate quadrature rule is used in the numerical integration, i.e., when the quadrature points are chosen inside the interval of quadrature. Some of these theoretical results can be found also in [2].

We validate our results with some numerical examples. As a model problem, we consider Poisson's equation with Dirichlet boundary conditions, but the results can be extended to other linear problems. We consider different star-shaped domains and we construct on each of them a standard tensor product parametrization, typically used in IGA, and a scaled boundary parametrization. Since the scaling center determines a unique SB-parametrization, we construct various SB-parametrizations by moving

the scaling center inside the kernel. In this way we want to study the influence of the choice of the scaling center on the numerical results, i.e., comparing, for example, the energy norm, the L^2 -error norm and the condition number of the stiffness matrix. Furthermore we compare the SB-parametrization with the standard parametrization typically used in IGA. For our simulations we use an extension of the ISOGAT package [63] implemented in MATLAB®.

Structure of the Thesis

After this introductory chapter, we present in Chapter 2 the tools used in CAGD and IGA, the B-splines and NURBS basis functions. Their definitions are given through a recursive formula known as Cox-De Boor algorithm. We list their most important properties that permit engineers and designers to use them widely. Given a set of control points, we then define the B-spline and NURBS geometries, such as curves and surfaces. We conclude the chapter by showing different refinement techniques that permit us to describe a curve with a new set of control points and knots without changing its shape.

In Chapter 3, we give a summary of the main ideas behind isogeometric analysis. Given a problem in the strong form, we show how to derive its weak form. The domain on which we solve the problem will be parametrized by a geometry function that goes from the parameter domain to the physical one. Afterward, the approximation of the space where the analytical solution lives will be done through Galerkin's method, using as basis functions the ones given by the parametrization. Hence, the isogeometric analysis, as well as the finite element method, leads to solve a linear system where the stiffness matrix is sparse. We also present some a priori error estimates for IGA. In the end, we solve Poisson's equation with zero Dirichlet boundary conditions on different geometries.

In Chapter 4, we introduce the SB-parametrizations and the SB-IGA. Given a star-shaped domain and a point in its kernel, we show how to construct a scaled boundary parametrization. This parametrization will be used in the standard Galerkin-based IGA and in the SB-IGA. We prove that the two approaches are equivalent both at a weak analytical level and at a discrete level. Indeed, making use of the Laplace-Beltrami operator, we show that these two approaches lead to the same weak form in parametric coordinates. Moreover, with an equivalence theorem, we show that these weak forms coincide when a Galerkin discretization is applied. We also investigate the singularity of the parametrization in the scaling center. In the numerical simulations, we solve Poisson's equations with zero Dirichlet boundary conditions and we compare the results for different parametrizations.

We conclude this thesis in Chapter 5, where we summarize the results and we give an outlook on possible future research directions.

Foundations from Computational Geometry

The nonrational B-splines and the nonuniform rational B-splines (NURBS) describe geometries in computer-aided geometric design (CAGD) and also represent the numerical solution in isogeometric analysis (IGA).

The word spline comes from the same root as splinter. Indeed, splines were thin strips of wood used by boat builders to create and draw curves. These were bent and held in place at a number of predetermined points, called ducks. Between the ducks, the elasticity of the spline material caused the strip to take the shape that minimized the energy of bending, thus creating the smoothest possible curve that fit the constraints. The shape could be tweaked by moving the ducks. It was only after World War II that the polynomial formula, known as the spline curve or spline function, was developed by the mathematician I. J. Schoenberg [50]. A spline curve is a piecewise polynomial curve whose pieces are smoothly joined together. Using a mathematical representation of the surface of a boat or an airplane instead of a physical model saves thousands of measurements in the design and construction process. In the aircraft industry, besides their use in modeling designs, splines were also useful for plotting flight trajectories. During the 1960's, the French automatic engineers Pierre Bézier (at Renault) and Paul de Casteljau (at Citröen) concurrently developed the NURBS, which were used first in car design, then they became part of standard computer graphics packages. In a digital system, the ducks used by boat builders are transformed into control points that can be instantly weighted, moved and plotted to create any kind of curve.

However, at the end of the 90's, in the field of computer animation the use of NURBS surfaces was replaced by the subdivision surfaces, built upon research by E. Catmull and J. Clark examining the possibilities of recursive uniform B-Spline surfaces. For instance, Pixar released its first feature-length film, *Toy Story*, in 1995. The animators modeled the characters and props of the film using NURBS geometries. This process was expensive, time-consuming and error-prone. In their next animated short, *Geri's Game* (1997), Pixar used subdivision surfaces for modeling the characters.

While in the animation field the subdivision surface are preferred for their artistic flexibility and speed, engineers and designers continue to favor NURBS because they offer the precise control over curvature they need for accurately manufacturing real-life products. A bridge between these two worlds could be seen in the recent T-spline and T-NURCCs [51].

Nevertheless, here we will not investigate the subdivision surfaces and T-splines. We will instead consider B-spline and NURBS geometries.

This chapter is divided as follows. We first introduce the nonrational B-splines together

with some relevant properties in Section 2.1, then we move to a more general setting defining the NURBS in Section 2.2. Section 2.3 shows different refinement techniques, which permit to model a B-spline curve in different ways without changing its shape.

2.1 B-Splines

In this section we define the nonrational B-spline basis functions, curves and surfaces. We will also show their important properties. For the sake of brevity we drop the word nonrational.

A spline function is a piecewise polynomial function. The term B-spline is short for basis spline, since the B-splines are basis functions for spline functions, meaning that all possible spline functions can be built from a linear combination of B-splines, and there is only one unique combination for each spline function.

2.1.1 Definition and Properties of B-Spline Basis Functions

The B-splines are piecewise polynomials of a certain degree p in a variable ξ . The values of ξ where the pieces of polynomials meet are known as knots, denoted with ξ_1, ξ_2, \dots , and sorted into a nondecreasing sequence. They have local support which allows a quick evaluation and changes in one parameter affect only a part and not the whole of the B-spline. They are also very flexible. The definition of B-splines is given by a recursive formula, independently discovered by C. de Boor and M. Cox, and so called Cox-De Boor recursion formula.

Definition 2.1 (B-spline basis function). *Given a knot vector $\Xi := \{\xi_1, \dots, \xi_{m+p+1}\}$ with knots $\xi_i \in [0, 1]$ and $\xi_i \leq \xi_{i+1} \forall i$, a B-spline basis function $M_{i,p}(\xi)$ of degree p (order $p+1$) is defined recursively for $\xi \in [0, 1]$ and $i = 1, \dots, m$. The starting points are the piecewise constants for $p = 0$ (or characteristic functions)*

$$M_{i,0}(\xi) = \begin{cases} 1, & \text{if } \xi_i \leq \xi < \xi_{i+1}, \\ 0, & \text{otherwise,} \end{cases}$$

with the modification that the last B-spline $M_{m,0}$ is defined also for ξ_{m+1} , i.e.,

$$M_{m,0}(\xi) = \begin{cases} 1, & \text{if } \xi_m \leq \xi \leq \xi_{m+1}, \\ 0, & \text{otherwise.} \end{cases}$$

For $p > 0$ the B-splines are defined as

$$M_{i,p}(\xi) = \frac{\xi - \xi_i}{\xi_{i+p} - \xi_i} M_{i,p-1}(\xi) + \frac{\xi_{i+p+1} - \xi}{\xi_{i+p+1} - \xi_{i+1}} M_{i+1,p-1}(\xi), \text{ where } \xi \in [0, 1],$$

with the same modification for $M_{m,p}$. When there are repeated knots, some of the denominators above may be zero. We adopt the convention that $0/0$ is equal to zero.

The recursion formula has been modified to allow for a definition of the B-splines over the full interval of $[0, 1]$ instead of only $[0, 1)$.

We call the interval between two successive knots $[\xi_i, \xi_{i+1})$ the i -th knot-span. This can have zero length, since knots do not need to be distinct. If the knots ξ_i are uniformly distributed over Ξ , we call the knot vector uniform. If the first knot and the last one have multiplicity $p+1$, i.e., $\xi_1 = \dots = \xi_{p+1}$ and $\xi_{m+1} = \dots = \xi_{m+p+1}$, the knot vector is called open.

Remark 2.2. In [47] the recursive formula is defined for knots in \mathbb{R} . We restricted them to the interval $[0, 1]$ for our isogeometric purposes later.

There are many useful properties of the B-spline basis functions, which determine the desirable geometric characteristics in B-spline curves and surfaces. Among them we point out the following ones:

- local support property: $M_{i,p}(\xi) = 0$ if ξ is outside the interval $[\xi_i, \xi_{i+p+1})$,
- in any given knot-span $[\xi_j, \xi_{j+1})$ at most $p + 1$ B-spline basis functions $M_{i,p}$ are nonzero,
- nonnegativity: $M_{i,p}(\xi) \geq 0$ for all i, p , and ξ ,
- partition of unity: for an arbitrary i -th knot-span, $\sum_{i=1}^m M_{i,p}(\xi) = 1$ for all $\xi \in [\xi_i, \xi_{i+1})$,
- $M_{i,p}(\xi)$ are p -times continuously differentiable (\mathcal{C}^p -continuous) inside a knot-span, while at inner knots of multiplicity k ($k \leq p$) they are only \mathcal{C}^{p-k} .

Here we only use B-spline basis functions on open knot vectors with inner knots of multiplicity $1 \leq k \leq p$.

Definition 2.3 (B-spline space). *The vector space of the B-spline basis functions of degree p on the open knot vector Ξ is denoted by*

$$\mathcal{S}(\Xi, p) := \text{span}\{M_{i,p}\}_{i=1,\dots,m} \quad (2.1)$$

Note that $\dim(\mathcal{S}(\Xi, p)) = m$ and $M_{i,p}$ are actually a basis of $\mathcal{S}(\Xi, p)$, since they are linearly independent.

Example 2.4 (Different types of B-spline basis functions). *An example of B-spline basis functions with different degrees and continuities is shown in Figure 2.1:*

- (a) $\Xi = \{0, 0, 1/3, 2/3, 1, 1\}, p = 1, m = 4$: \mathcal{C}^0 -continuity at all inner knots,
- (b) $\Xi = \{0, 0, 0, 1/3, 2/3, 1, 1, 1\}, p = 2, m = 5$: \mathcal{C}^1 -continuity at all inner knots,
- (c) $\Xi = \{0, 0, 0, 1/3, 2/3, 2/3, 1, 1, 1\}, p = 2, m = 6$: \mathcal{C}^0 -continuity at $\xi = 2/3$ and \mathcal{C}^1 -continuity at $\xi = 1/3$,
- (d) $\Xi = \{0, 0, 0, 0, 1/3, 2/3, 1, 1, 1, 1\}, p = 3, m = 6$: \mathcal{C}^2 -continuity at all inner knots.

Definition 2.5 (Derivative of a B-spline basis function). *The derivative of a B-spline basis function can be computed as follows:*

$$\frac{d}{d\xi} M_{i,p}(\xi) = M'_{i,p}(\xi) = \frac{p}{\xi_{i+p} - \xi_i} M_{i,p-1}(\xi) - \frac{p}{\xi_{i+p+1} - \xi_{i+1}} M_{i+1,p-1}(\xi). \quad (2.2)$$

As a consequence of the partition of unity, we obtain the following property for the B-spline derivatives:

$$\sum_{i=1}^m M'_{i,p}(\xi) = 0 \text{ for all } \xi \in [\xi_i, \xi_{i+1}], \text{ for an arbitrary } i\text{-th knot-span.}$$

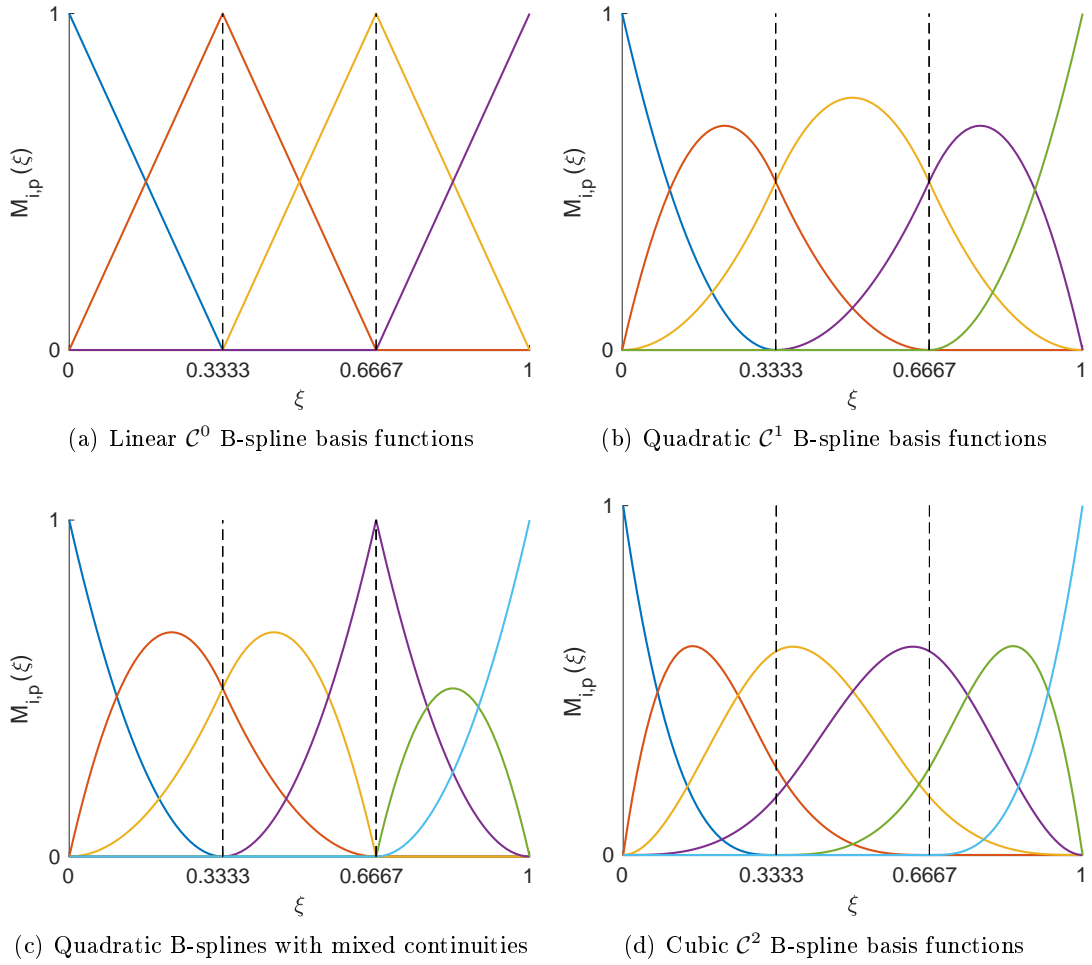


Figure 2.1. Different types of B-spline basis functions

2.1.2 B-Spline Geometries

The use of B-splines to define curves and surfaces for CAGD was first proposed by Gordon and Riesenfeld [27], who realized that de Boor's recursive B-spline evaluation was the natural generalization of the de Casteljau algorithm. Indeed, B-spline curves include Bézier curves as a proper subset.

Definition 2.6 (B-spline curve). *A p -th degree B-spline curve is defined by*

$$\gamma(\xi) = \sum_{i=1}^m M_{i,p}(\xi) \mathbf{c}_i, \quad 0 \leq \xi \leq 1, \quad (2.3)$$

where $\mathbf{c}_i \in \mathbb{R}^d, d \geq 1$, are the control points and $M_{i,p}$ the p -th degree B-spline basis functions defined on the open knot vector

$$\Xi = \{\underbrace{0, \dots, 0}_{p+1}, \xi_{p+2}, \dots, \xi_m, \underbrace{1, \dots, 1}_{p+1}\}.$$

The polygon formed by the $\{\mathbf{c}_i\}_{i=1, \dots, m}$ is called control polygon.

Remark 2.7. *A more general definition follows when the knot vector is given as $\Xi = \{\underbrace{a, \dots, a}_{p+1}, \xi_{p+2}, \dots, \xi_m, \underbrace{b, \dots, b}_{p+1}\}$. Hence, $\gamma(\xi)$ is defined for $a \leq \xi \leq b$.*

The properties of B-spline curves follow from those given in Section 2.1.1 for the B-spline basis functions. We list here some of them:

- $\gamma(\xi)$ is a piecewise polynomial curve, since the $M_{i,p}(\xi)$ are piecewise polynomials,
- endpoint interpolation: $\gamma(0) = \mathbf{c}_1$ and $\gamma(1) = \mathbf{c}_m$,
- strong convex hull property: the B-spline curve is contained in the convex hull of its control polygon,
- local modification scheme: moving the control point \mathbf{c}_i changes $\gamma(\xi)$ only in the interval $[\xi_i, \xi_{i+p+1})$,
- the continuity and differentiability of $\gamma(\xi)$ follow from the one of the $M_{i,p}(\xi)$. Thus $\gamma(\xi)$ is infinitely differentiable in the interior of knot intervals and it is at least $p - k$ times continuously differentiable at a knot of multiplicity k ,
- the control polygon represents a piecewise linear approximation to the curve. This approximation is improved by knot insertion and degree elevation (see Section 2.3). As a general rule, the lower the degree, the closer a B-spline curve follows its control polygon (see Figure 2.2(c)),
- variation diminishing property: each hyperplane in \mathbb{R}^n has at most as many intersections with the B-spline curve as with the control polygon.

Example 2.8. *Some of the properties of a B-spline curve are shown in Figure 2.2.*

- (a) *Given the knot vector $\Xi = \{0, 0, 0, 0, 1/7, 2/7, 3/7, 4/7, 5/7, 6/7, 1, 1, 1, 1\}$, a cubic ($p = 3$) curve is constructed and one control point is moved. Note that exactly four pieces of the curve changed and this is the maximum number of pieces that can change if the curve is cubic.*

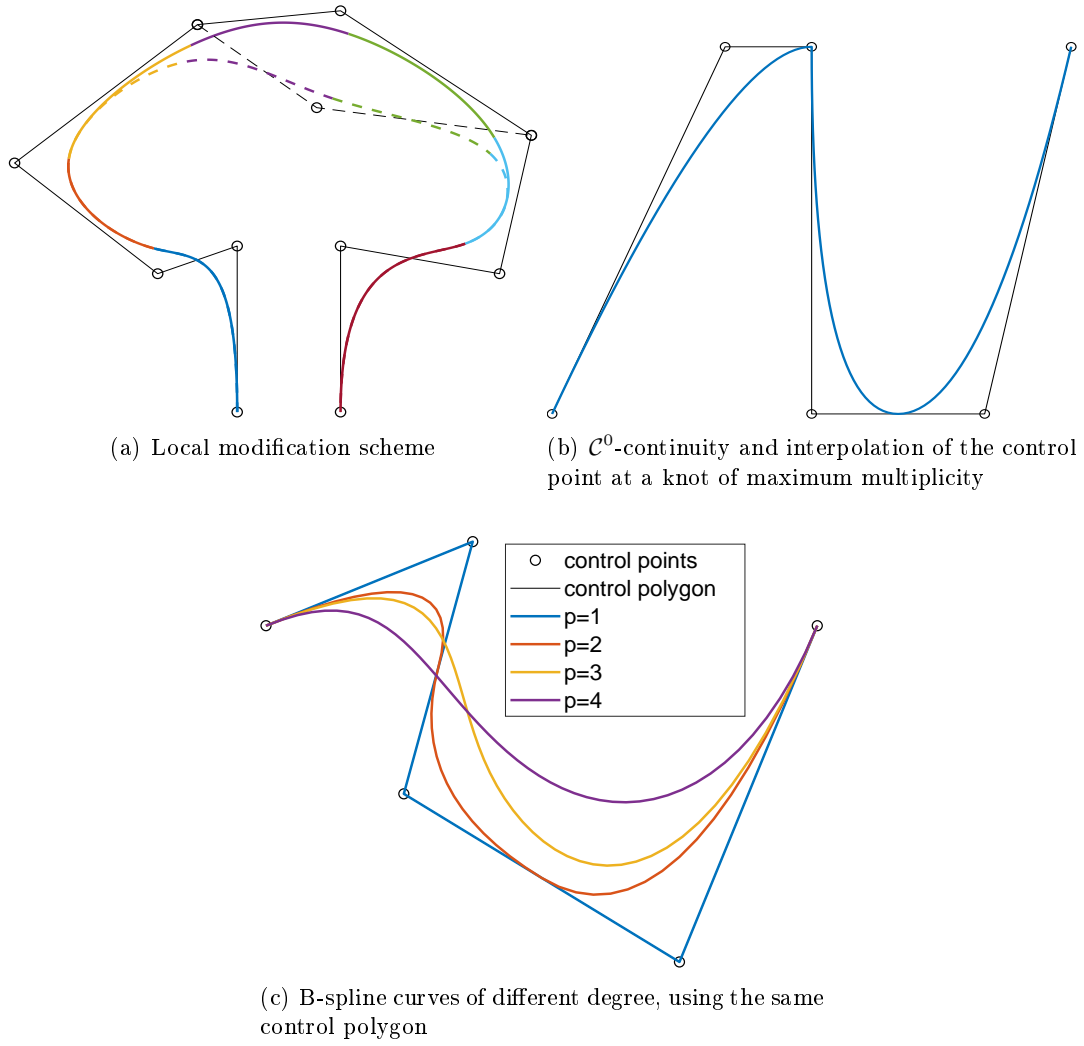


Figure 2.2. Properties of B-spline curves

(b) A quadratic ($p = 2$) curve with knot vector $\Xi = \{0, 0, 0, 1/3, 1/3, 2/3, 1, 1, 1\}$ is considered. Since the knot $1/3$ has multiplicity 2, the curve is only C^0 -continuous and the control point related to that knot is interpolated.

(c) Fixed a control polygon with 5 control points, 4 different B-spline curves of degree $p = 1, 2, 3, 4$, are represented. The knot vectors are respectively:

- $p = 1$: $\Xi = \{0, 0, 1/4, 2/4, 3/4, 1, 1\}$,
- $p = 2$: $\Xi = \{0, 0, 0, 1/3, 2/3, 1, 1, 1\}$,
- $p = 3$: $\Xi = \{0, 0, 0, 0, 1/2, 1, 1, 1, 1\}$,
- $p = 4$: $\Xi = \{0, 0, 0, 0, 0, 1, 1, 1, 1, 1\}$.

For $p = 1$ the curve coincides exactly with the control polygon. Moreover, the higher the degree, the further the curve moves away from the polygon.

Definition 2.9 (B-spline surface). A B-spline surface is obtained by taking a bidirectional net of control points $\{\mathbf{d}_{i,j}\} \subset \mathbb{R}^d, d \geq 2$, two open knot vectors Ξ, H , and the products of the univariate B-spline functions $M_{i,p}(\xi), N_{j,q}(\eta)$:

$$\mathbf{\Gamma}(\xi, \eta) = \sum_{i=1}^m \sum_{j=1}^n M_{i,p}(\xi) N_{j,q}(\eta) \mathbf{d}_{i,j}, \quad (2.4)$$

with

$$\Xi = \{\underbrace{0, \dots, 0}_{p+1}, \xi_{p+2}, \dots, \xi_m, \underbrace{1, \dots, 1}_{p+1}\},$$

$$H = \{\underbrace{0, \dots, 0}_{q+1}, \eta_{q+2}, \dots, \eta_n, \underbrace{1, \dots, 1}_{q+1}\}.$$

The control points $\{\mathbf{d}_{i,j}\}_{i=1,\dots,m,j=1,\dots,n}$ form the control net (or control mesh).

The properties of the tensor product basis functions (called also bivariate tensor product B-splines) follow from the corresponding properties of the univariate basis functions:

- $M_{i,p}(\xi)N_{j,q}(\eta) = 0$ if (ξ, η) is outside the rectangle $[\xi_i, \xi_{i+p+1}) \times [\eta_j, \eta_{j+q+1})$,
- in any given rectangle $[\xi_{i_0}, \xi_{i_0+p+1}) \times [\eta_{j_0}, \eta_{j_0+q+1})$ at most $(p+1)(q+1)$ basis functions $M_{i,p}(\xi)N_{j,q}(\eta)$ are nonzero,
- nonnegativity: $M_{i,p}(\xi)N_{j,q}(\eta) \geq 0$ for all i, j, p, q, ξ , and η ,
- partition of unity: $\sum_{i=1}^m \sum_{j=1}^n M_{i,p}(\xi)N_{j,q}(\eta) = 1$ for all $(\xi, \eta) \in [0, 1] \times [0, 1]$,
- all partial derivatives of $M_{i,p}(\xi)N_{j,q}(\eta)$ exist inside the interior of the rectangles formed by the ξ and η knot lines, where the function is a bivariate polynomial. At a ξ knot (η knot) it is $p-k$ ($q-k$) times differentiable in the ξ (η) direction, where k is the multiplicity of the knot.

The B-spline surfaces have the following properties:

- the surface interpolates the four corner control points: $\mathbf{\Gamma}(0, 0) = \mathbf{d}_{1,1}$, $\mathbf{\Gamma}(0, 1) = \mathbf{d}_{1,n}$, $\mathbf{\Gamma}(1, 0) = \mathbf{d}_{m,1}$, $\mathbf{\Gamma}(1, 1) = \mathbf{d}_{m,n}$,
- strong convex hull property: the B-spline surface is in the convex hull of its control net,
- local modification scheme: changing the position of the control point $\mathbf{d}_{i,j}$ affects the surface only in the rectangle $[\xi_i, \xi_{i+p+1}) \times [\eta_j, \eta_{j+q+1})$,
- the continuity and differentiability of $\mathbf{\Gamma}(\xi, \eta)$ follow from the ones of the basis functions. In particular, $\mathbf{\Gamma}(\xi, \eta)$ is $p-k$ ($q-k$) times differentiable in the ξ (η) direction at a ξ (η) knot of multiplicity k .

We remark here that there is no known variation diminishing property for B-spline surfaces [48].

Although B-splines can represent a large number of curves and surfaces, important types like circles are excluded. Therefore, we next extend the theory to rational piecewise polynomials which are better suited to conics.

2.2 NURBS

NURBS is an acronym that stands for nonuniform rational B-splines and describes weighted B-splines over nonuniformly spaced knot vectors. They are important for IGA because they contain rational polynomials which allow to exactly represent conic sections like disks and spheres.

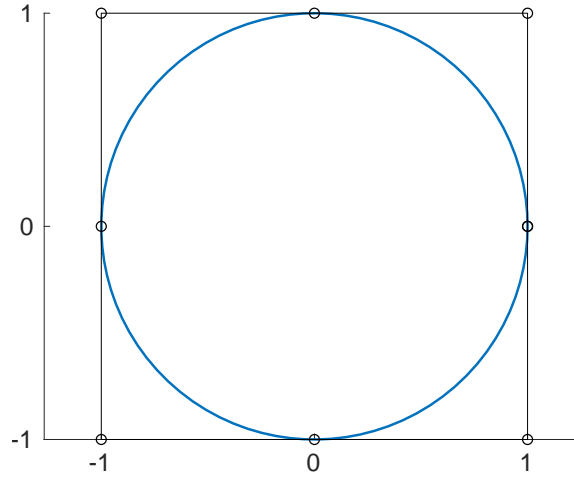


Figure 2.3. Representation of a circle as a NURBS curve

Definition 2.10 (NURBS basis function). *The definition of NURBS basis functions $R_{i,p}$ is based on B-spline basis functions $M_{i,p}$ on a knot vector Ξ and additional weights $\omega_i > 0$, $i = 1, \dots, m$:*

$$R_{i,p}(\xi) = \frac{M_{i,p}(\xi) \omega_i}{\sum_{j=1}^m M_{j,p}(\xi) \omega_j}, \quad i = 1, \dots, m. \quad (2.5)$$

Note that if ω_i is constant for all i , then $R_{i,p}(\xi) = M_{i,p}(\xi)$, i.e., NURBS basis functions reduce to B-splines.

As already seen for B-splines in the previous section, it's also possible to define geometries using NURBS, such as NURBS curves and NURBS surfaces. To avoid repetition, the definition of those geometries will not be presented here, but it can be easily derived substituting the B-spline basis functions with the NURBS functions in the formulae (2.3) and (2.4).

Furthermore, all the properties of the B-spline functions, curves and surfaces hold when a NURBS geometry is considered.

Example 2.11 (A circle as a NURBS curve). *A standard example used to illustrate the advantages of NURBS is the exact representation of a circle. In Figure 2.3 a circle of radius 1 is shown. The knot vector of the quadratic NURBS basis functions is $\Xi = \{0, 0, 0, 1/4, 1/4, 1/2, 1/2, 3/4, 3/4, 1, 1, 1\}$, weights are $\omega = \{1, \sqrt{2}/2, 1, \sqrt{2}/2, 1, \sqrt{2}/2, 1, \sqrt{2}/2, 1\}$ and control points of the curve are*

$$\{\mathbf{c}_i\}_{i=1,\dots,9} = \{(1, 0), (1, 1), (0, 1), (-1, 1), (-1, 0), (-1, -1), (0, -1), (1, -1), (1, 0)\}.$$

2.3 Refinements

An important property of the B-spline and NURBS geometries is the possibility to refine them without changing the shape. In our IGA context, this is crucial when we solve an equation on a domain defined by NURBS. Indeed, the geometry is fixed and it cannot change. A refinement of the mesh, in terms of knot vectors and control points, leads to a better approximation of the solution. While in the modeling and

animation field, it is important because, instead of drawing the curve (surface), the control polygon (net) is drawn. The subdivision scheme consists in a refinement of the control polygon that tends to a limit curve.

There are different types of refinements, below we see them described and applied to a B-spline curve.

Knot insertion (or h -refinement)

As suggested by the name of this refinement, an additional knot is inserted in the given knot vector.

Given a p -th degree B-spline curve $\gamma(\xi)$ defined on Ξ as in (2.3), let $\bar{\xi} \in [\xi_k, \xi_{k+1})$ and insert it into Ξ to form the new knot vector $\bar{\Xi}$. Then a new set of $m+1$ basis functions $\bar{M}_{i,p}(\xi)$ is provided and the curve γ has a representation on $\bar{\Xi}$ of the form

$$\gamma(\xi) = \sum_{i=1}^{m+1} \bar{M}_{i,p}(\xi) \bar{\mathbf{c}}_i,$$

where $\{\bar{\mathbf{c}}_i\}$ is the new set of control points. The new control points $\bar{\mathbf{c}}_i$ are computed as a linear combination of the original control points \mathbf{c}_i , by imposing the following system of linear equations

$$\sum_{i=1}^m M_{i,p}(\xi) \mathbf{c}_i = \sum_{i=1}^{m+1} \bar{M}_{i,p}(\xi) \bar{\mathbf{c}}_i.$$

We then obtain the following formula for the construction of the new control points:

$$\bar{\mathbf{c}}_i = \alpha_i \mathbf{c}_i + (1 - \alpha_i) \mathbf{c}_{i-1}, \quad (2.6a)$$

where

$$\alpha_i = \begin{cases} 1, & i = 1, \dots, k-p, \\ \frac{\bar{\xi} - \xi_k}{\xi_{k+p+1} - \bar{\xi}}, & i = k-p+1, \dots, k, \\ 0, & i = k+1, \dots, m+1. \end{cases} \quad (2.6b)$$

Note that only p new control points must be computed. Details on how to obtain (2.6) can be found in [11, 20, 47]. It is important to notice that the knot insertion is just a change of the B-spline space $\mathcal{S}(\Xi, p)$ into $\mathcal{S}(\bar{\Xi}, p)$, the curve is not changed.

The above discussion of knot insertion holds for B-spline curves. But since a NURBS curve can be seen as a projection of 3D B-spline curves to 2D, the knot insertion for NURBS curves is done as follows. Given a NURBS curve of degree p with knot vector Ξ , control points $\{\mathbf{c}_i = (x_i, y_i)\}_{i=1, \dots, m}$, and weights $\{\omega_i\}_{i=1, \dots, m}$, the knot insertion is done in three steps.

- (1) First we convert the given NURBS curve in 2D to a B-spline curve in 3D, i.e., we consider the B-spline curve of degree p with knot vector Ξ and control points $\{(w_i x_i, w_i y_i, w_i)\}_{i=1, \dots, m}$.
- (2) We insert a knot $\bar{\xi}$ into Ξ and, using the algorithm in (2.6), we compute the new control points $\{(X_i, Y_i, W_i)\}_{i=1, \dots, m+1}$.
- (3) We project the new set of control points back to 2D to form the new set of control points and weights for the given NURBS curve after the required knot has been inserted, i.e., the new control points are $\{\bar{\mathbf{c}}_i = (X_i/W_i, Y_i/W_i)\}_{i=1, \dots, m+1}$ and the new weights $\{\bar{\omega}_i = W_i\}_{i=1, \dots, m+1}$.

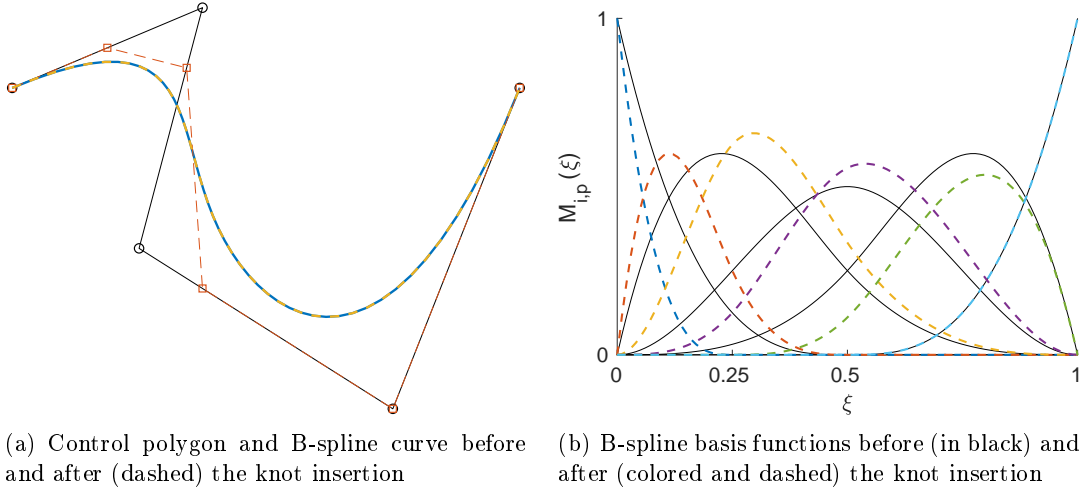


Figure 2.4. Example of knot insertion

The same procedure is applied when $\mathbf{c}_i \in \mathbb{R}^d, d \geq 3$.

Some of the important uses of the knot insertion algorithm are:

- subdividing curves and surfaces,
- adding control points in order to increase the flexibility in shape control,
- evaluating points and derivatives on curves and surfaces.

Indeed this evaluation could be very expensive when done with recursion formulae, such as de Boor's algorithm. With a subdivision scheme this evaluation is done on the limit curve (surface) of a sequence of successive refinements of the control polygon (net).

In Figure 2.4(a) a cubic B-spline curve, with knot vector $\Xi = \{0, 0, 0, 0, 1/2, 1, 1, 1, 1\}$ and control points $\{\mathbf{c}_i\}_{i=1,\dots,5} = \{(2, 2), (3.5, 2.5), (3, 1), (5, 0), (6, 2)\}$, is constructed. Then $\xi = 1/4$ is inserted once, so that $\bar{\Xi} = \{0, 0, 0, 0, 1/4, 1/2, 1, 1, 1, 1\}$. The refined control polygon contains

$$\{\bar{\mathbf{c}}_i\}_{i=1,\dots,6} = \{(2, 2), (2.75, 2.25), (3.375, 2.125), (3.5, 0.75), (5, 0), (6, 2)\},$$

where exactly $p = 3$ points are new. Since $1/4$ is in the knot-span $[0, 1/2)$, this refinement is affecting only the basis functions that are defined on that interval (see Figure 2.4(b)).

More knots can be inserted at the same time. Note that if the knot inserted is already present in Ξ , then its multiplicity is increased and the continuity of the basis functions will be reduced. However each unique internal knot value shall appear no more than p times otherwise the curve becomes discontinuous.

Degree elevation (or p -refinement)

This refinement elevates the degree of the B-spline basis functions such that the global smoothness is preserved.

Let $\gamma(\xi)$ a p -th degree B-spline curve defined on Ξ as in (2.3). Since $\gamma(\xi)$ is a piecewise polynomial curve, it is possible to elevate its degree to $p + 1$ such that

$$\gamma(\xi) = \sum_{i=1}^{\bar{m}} \bar{M}_{i,p+1}(\xi) \bar{\mathbf{c}}_i.$$

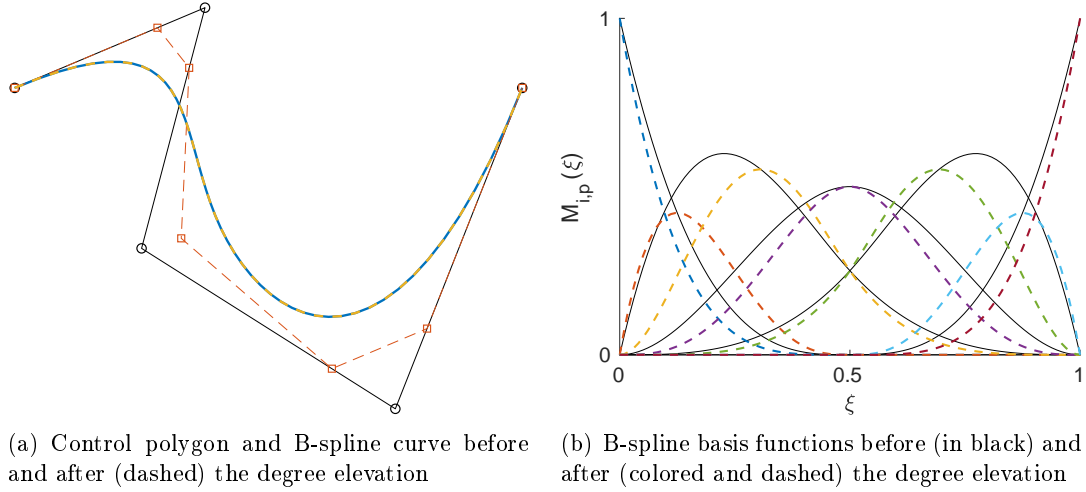


Figure 2.5. Example of degree elevation

In this refinement \bar{m} , $\bar{\Xi}$, and the new set of control points $\{\bar{\mathbf{c}}_i\}$ have to be computed. More precisely in order to maintain the same continuity at inner knots, the multiplicity of all distinct knots has to be increased by one for the new knot vector $\bar{\Xi}$. For more details on the computation of the new control points we refer to [47].

As an example, we consider the same cubic B-spline curve used in the knot insertion example. In Figure 2.5 a degree elevation is performed once. The new knot vector is $\bar{\Xi} = \{0, 0, 0, 0, 0, 1/2, 1/2, 1, 1, 1, 1, 1\}$ and the B-spline basis functions have now degree $p + 1 = 4$. The refined control polygon is

$$\{\bar{\mathbf{c}}_i\}_{i=1,\dots,7} = \{(2, 2), (3.125, 2.375), (3.375, 2.125), (3.312, 1.062), (4.5, 0.25), (5.25, 0.5), (6, 2)\}.$$

Unlike the knot insertion, the degree elevation is affecting all the basis functions and all the control points, except (by definition) the first one, $\mathbf{c}_1 = \bar{\mathbf{c}}_1$, and the last one, $\mathbf{c}_m = \bar{\mathbf{c}}_{\bar{m}}$.

Remark 2.12. *Knot insertion and degree elevation work also for multivariate B-splines and NURBS due to the tensor product structure.*

As already mentioned in Section 2.1.2, the control polygon represents an approximation to the corresponding curve. This approximation is improved when a refinement is performed. In Figure 2.6 we consider the same cubic B-spline curve with knot vector $\Xi = \{0, 0, 0, 0, 1/2, 1, 1, 1, 1\}$ as before and we apply different refinements.

- Figure 2.6(a): 5 knots are inserted into the knot vector Ξ . At the beginning $1/4$, then $1/4$ together with $4/5$ and at the end $1/2$ with $2/3$. The final knot vector is $\bar{\Xi} = \{0, 0, 0, 0, 1/4, 1/4, 1/2, 1/2, 2/3, 4/5, 1, 1, 1, 1\}$.
- Figure 2.6(b): the degree elevation is applied 5 times in a row to the same curve.

We can observe that, when applying multiple knot insertions, the control polygon is getting closer to the curve faster than when applying multiple degree elevations. This is true only if the inserted knots are distributed enough along the initial knot vector.

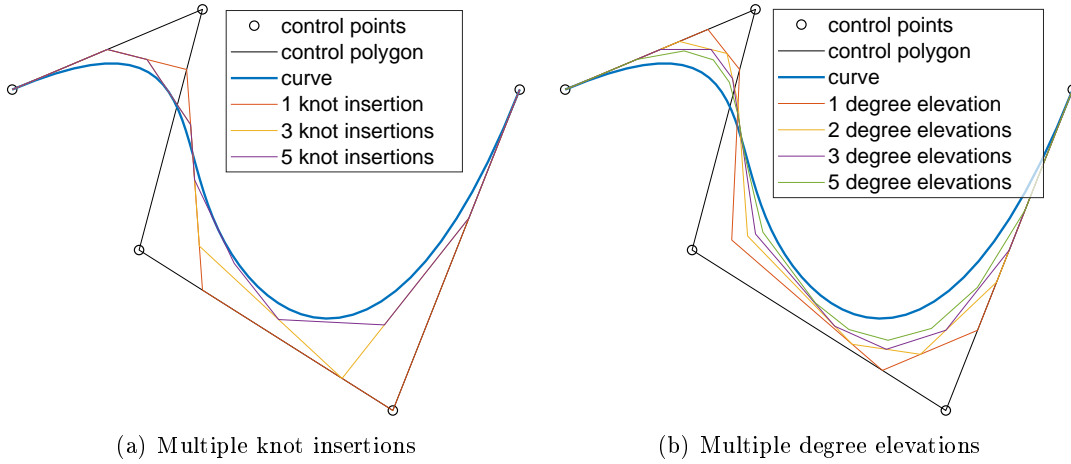


Figure 2.6. Successive refinements (knot insertions on the left and degree elevations on the right) are performed on the same curve. The control polygon better approximates the curve after more refinements.

***k*-refinement**

A series of knot insertions and degree elevations can also be carried out. It is important to notice that the refinement strategies do not commute, i.e., the order influences the result. For this reason when a series of refinements has to be done, it is better to first perform the degree elevation and secondly the knot insertion, since in this way a maximal continuity in the inner knots could be achieved. This difference is shown in the following example. *k*-refinement means that *p*-refinements are carried out before any *h*-refinement steps.

Example 2.13 (Comparison of the combination of different refinement strategies). *With the example in Figure 2.7, we want to show that it is convenient to apply first the degree elevation refinements and then the knot insertions. We start with the linear ($p = 1$) B-spline basis functions on the knot vector $\Xi = \{0, 0, 1, 1\}$.*

- (a) *First we insert the knots $1/3$ and $2/3$ in the knot vector, secondly we elevate the degree. This leads to $\bar{\Xi} = \{0, 0, 0, 1/3, 1/3, 2/3, 2/3, 1, 1, 1\}$. The final spline space $\mathcal{S}(\bar{\Xi}, 2)$ has degree 2, dimension $\bar{m} = 7$ and C^0 -continuity in the interior knots.*
- (b) *First we perform a degree elevation and then we insert the knots $1/3$ and $2/3$. The final knot vector is $\bar{\Xi} = \{0, 0, 0, 1/3, 2/3, 1, 1, 1\}$. In this case the final spline space $\mathcal{S}(\bar{\Xi}, 2)$ has still degree 2, but dimension $\bar{m} = 5$ and C^1 -continuity in the interior knots.*

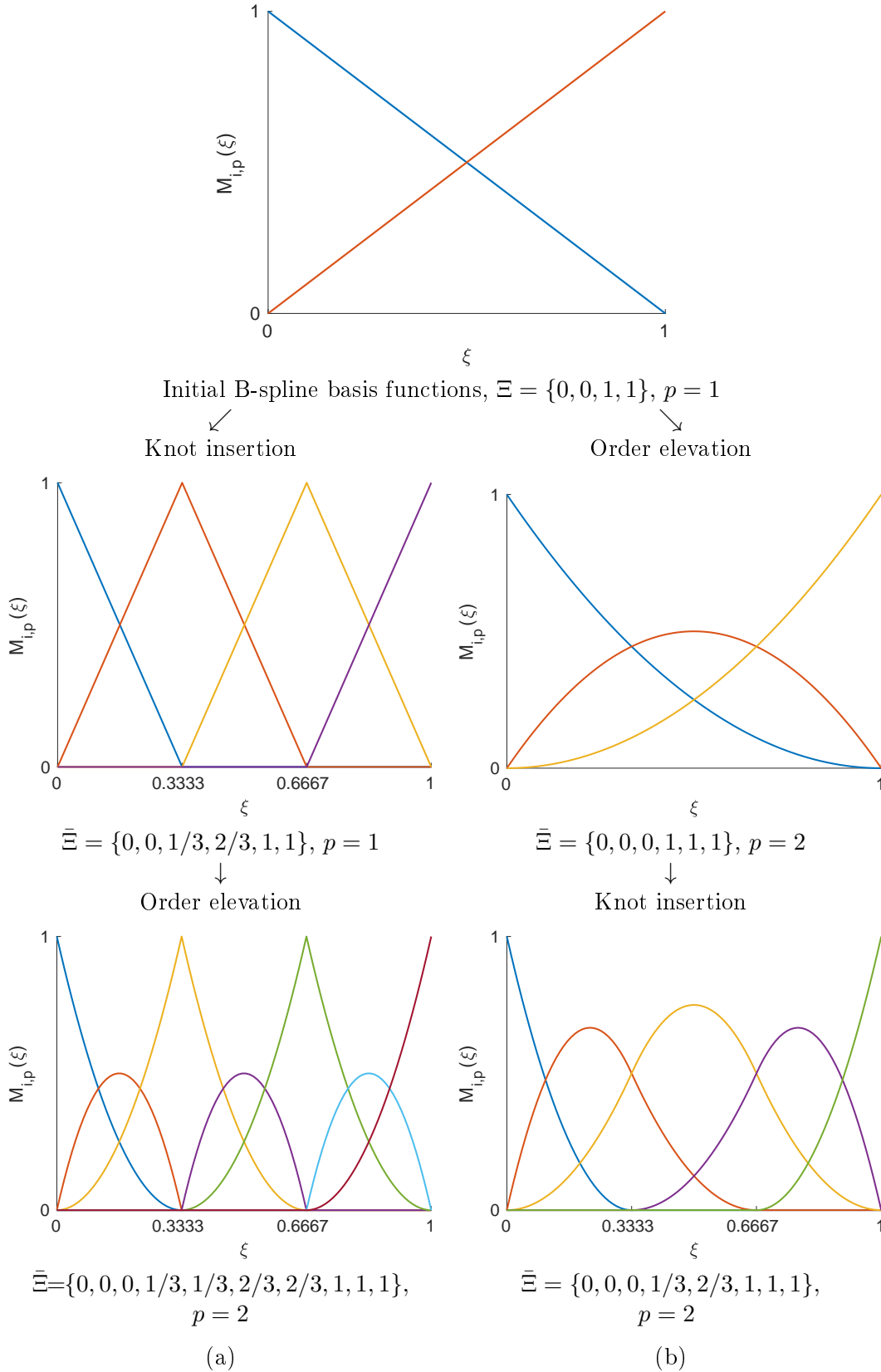


Figure 2.7. Comparison of a series of refinements in different order, when the starting knot vector is the same. (a) Knot insertion followed by degree elevation results in seven piecewise quadratic basis functions that are \mathcal{C}^0 at internal knots. (b) Degree elevation followed by knot insertion results in five piecewise quadratic basis functions that are \mathcal{C}^1 at internal knots.

Isogeometric Analysis

The main idea of isogeometric analysis is to bridge the gap between CAGD and finite element method (FEM). To do so the same functions for the description of the geometry in the design process and for the structural analysis are employed. Thus ensuring that the geometry in the analysis process is always exactly represented. The key ingredient of IGA are spline basis functions and geometries, already introduced in the previous chapter. Based on [17, 32], we introduce the main concept of IGA and summarize the major properties.

In Section 3.1 we define a boundary value problem in its strong form and we reformulate it in the weak form. Moreover, with Galerkin's method we approximate the space on which the analytical solution of the problem lives. In Section 3.2 we set the basis functions for this approximation space that are obtained via a parametrization of the domain on which we solve the problem. Finally, in Section 3.3 we use IGA to solve Poisson's equation with Dirichlet boundary conditions on different domains.

3.1 Strong and Weak Form of a Boundary Value Problem

We start here with the definition of a boundary value problem. We restrict our attention to linear elliptic partial differential equations (PDEs) of second order, in particular to Poisson's equation.

Definition 3.1 (Strong form of a boundary value problem). *Let L be an operator acting on an unknown function $u : \Omega \subset \mathbb{R}^d \rightarrow \mathbb{R}$ and let $f : \Omega \rightarrow \mathbb{R}$ be a given source term. A boundary value problem is given in the strong form by*

$$Lu = f \quad \text{in an open bounded domain } \Omega, \quad (3.1a)$$

together with boundary conditions on the boundary $\partial\Omega$

$$u = 0 \quad \text{on a Dirichlet boundary } \partial\Omega_D \subset \partial\Omega, \quad (3.1b)$$

$$\partial_n u = 0 \quad \text{on a Neumann boundary } \partial\Omega_N \subset \partial\Omega, \quad (3.1c)$$

where $\partial\Omega_D \cap \partial\Omega_N = \emptyset$ and $\partial\Omega_D \cup \partial\Omega_N = \partial\Omega$.

Remark 3.2. *For ease of presentation we have considered zero boundary conditions. In a more general setting the boundary conditions can be written as follows:*

$$\begin{aligned} u &= g_D \quad \text{on } \partial\Omega_D, \\ \partial_n u &= g_N \quad \text{on } \partial\Omega_N. \end{aligned}$$

In our model problem the operator L will be a linear uniformly elliptic differential operator of second order.

Definition 3.3 (Poisson's equation). *Let $Lu = \operatorname{div}(\nabla u) =: \Delta u$ be the Laplace operator acting on u , then Poisson's equation is given by*

$$\begin{cases} -\Delta u &= f & \text{in } \Omega, \\ u &= 0 & \text{on } \partial\Omega_D, \\ \partial_n u &= 0 & \text{on } \partial\Omega_N. \end{cases} \quad (3.2)$$

On the boundary $\partial\Omega$ may rule Dirichlet boundary conditions on $\partial\Omega_D$ or Neumann conditions on $\partial\Omega_N$. We call u a classical solution if it satisfies (3.2) pointwise and is an element of $\mathcal{C}^2(\Omega) \cap \mathcal{C}^1(\bar{\Omega})$ where $\bar{\Omega}$ is the closure of Ω . In case of $\partial\Omega_D = \partial\Omega$, a classical solution is a member of $\mathcal{C}^2(\Omega) \cap \mathcal{C}(\bar{\Omega})$.

From now on we consider $\partial\Omega_D = \partial\Omega$.

To find a solution to the above boundary value problem, we reformulate it through its weak, or variational, form. The solution needs not satisfy the PDE pointwise anymore but weakly in an integral over multiplications with test functions. The weak form will also serve as a starting point for the discretization process.

Definition 3.4 (Weak form of a boundary value problem). *We say that $u \in \mathcal{V}$ is a weak solution of the boundary value problem (3.1) if*

$$u \in \mathcal{V} : a(u, v) = l(v) \quad \forall v \in \mathcal{V}, \quad (3.3)$$

where v are called test functions, the space $\mathcal{V} = H_0^1(\Omega) := \{v \in H^1(\Omega), v = 0 \text{ on } \partial\Omega\}$ is a Hilbert space consisting of all functions $v \in L^2(\Omega)$ that possess weak and square-integrable first derivatives and that vanish on the boundary, $a(\cdot, \cdot) : \mathcal{V} \times \mathcal{V} \rightarrow \mathbb{R}$ is the bilinear form associated to the operator L , and $l(\cdot)$ is a linear form defined as the standard L^2 -scalar product, $l(v) := \langle v, f \rangle$.

To obtain the bilinear form a associated to L and thus the weak form of the problem, we multiply the strong form with test functions from \mathcal{V} and we use integration by parts.

Example 3.5 (Weak form for Poisson's equation). *Consider the strong form of Poisson's equation with zero Dirichlet boundary conditions*

$$\begin{cases} -\Delta u &= f & \text{in } \Omega, \\ u &= 0 & \text{on } \partial\Omega. \end{cases}$$

To obtain the corresponding weak form, we consider a test function $v \in \mathcal{V}$, we multiply it by the strong form and we integrate over the domain Ω , i.e.,

$$\int_{\Omega} -\Delta u v = \int_{\Omega} f v.$$

Then integrating by parts and using the boundary conditions we obtain

$$\int_{\Omega} \nabla u \nabla v = \int_{\Omega} f v.$$

Poisson's problem in the weak form now reads:

$$\text{find } u \in \mathcal{V} \text{ such that } a(u, v) := \int_{\Omega} \nabla u \nabla v = \int_{\Omega} f v =: l(v) \quad \forall v \in \mathcal{V}.$$

We now make some further assumptions and we introduce the properties of the bilinear form that we need, to show that the weak equation has a solution.

Definition 3.6. A bilinear form $a : \mathcal{V} \times \mathcal{V} \rightarrow \mathbb{R}$ on a Hilbert space \mathcal{V} with norm $\|\cdot\|$ is

- *bounded (or continuous)* if there exists a constant $M < \infty$ such that $a(u, v) \leq M\|u\|\|v\| \forall u, v \in \mathcal{V}$,
- *coercive* if there exists a constant $\alpha > 0$ such that $a(v, v) \geq \alpha\|v\|^2 \quad \forall v \in \mathcal{V}$,
- *symmetric* if $a(u, v) = a(v, u) \quad \forall u, v \in \mathcal{V}$.

The Lax-Milgram lemma is central to show whether elliptic partial differential equations can be uniquely solved.

Lemma 3.7 (Lax-Milgram lemma). *For a Hilbert space \mathcal{V} , a bounded, coercive bilinear form $a : \mathcal{V} \times \mathcal{V} \rightarrow \mathbb{R}$, and a linear functional $l \in \mathcal{V}^*$, there exists a unique solution $u \in \mathcal{V}$ of*

$$a(u, v) = l(v) \quad \forall v \in \mathcal{V}. \quad (3.4)$$

Proof. See [24, Theorem 1, pages 297–299]. \square

For Poisson’s boundary value problem in the Example 3.5, the norm of the space \mathcal{V} is the standard L^2 -norm on Ω , i.e. $\|\cdot\| := \|\cdot\|_{L^2(\Omega)}$. Moreover we see that $|a(u, u)| = \|\nabla u\|^2$ and by the Cauchy–Schwarz inequality $|a(u, v)| \leq \|\nabla u\|\|\nabla v\|$. With Lemma 3.7 we conclude that Poisson’s equation has a unique solution.

To solve the PDEs numerically, different techniques are available and can be implemented in an isogeometric framework, such as Galerkin’s method, collocation methods and so on. In this work we consider and present only the Galerkin approach. For collocation methods in IGA we refer to [49].

3.1.1 Galerkin’s Method

Galerkin’s method consists of constructing a finite-dimensional approximation of the space \mathcal{V} , denoted \mathcal{V}_h . Strictly speaking, this will be a subset such that

$$\mathcal{V}_h \subset \mathcal{V}. \quad (3.5)$$

We can now write a variational equation of the form of (3.3) also in the finite-dimensional space:

$$u_h \in \mathcal{V}_h : a(u_h, v_h) = l(v_h) \quad \forall v_h \in \mathcal{V}_h. \quad (3.6)$$

The finite-dimensional nature of the function space \mathcal{V}_h leads to a coupled system of linear algebraic equations. Indeed if $K = \dim(\mathcal{V}_h)$ and $\mathcal{V}_h := \text{span}\{\phi_i : i = 1, \dots, K\}$, then any function in \mathcal{V}_h has a basis representation and in particular $u_h = \sum_{i=1}^K u_i \phi_i$ with coefficients $u_i \in \mathbb{R}$. Upon inserting u_h into the weak form (3.6) and testing with $v_h = \phi_j$ for $j = 1, \dots, K$, one obtains the linear system

$$\mathbf{A}\mathbf{u} = \mathbf{r}, \quad (3.7)$$

where $\mathbf{u} = (u_1, \dots, u_K)^T$ is the vector of solution coefficients, \mathbf{A} is the stiffness matrix with entries $A_{i,j} = a(\phi_i, \phi_j)$ for all $i, j = 1, \dots, K$, and \mathbf{r} is the right-hand side vector with components $r_i = l(\phi_i)$, $i = 1, \dots, K$. Since the matrix \mathbf{A} inherits the

properties of the bilinear form a , it is straightforward to show that \mathbf{A} is symmetric positive definite, and thus the numerical solution \mathbf{u} or u_h , respectively, is well-defined. Furthermore the assumptions for the Lax-Milgram Lemma 3.7 are also fulfilled, which directly implicates the existence of a unique solution in \mathcal{V}_h .

The assembling of the system and thus the choice of the space \mathcal{V}_h will be shown in the next section where the isogeometric approach is presented. In general, a basis of locally supported functions is attractive. Indeed, we have that $a(\phi_i, \phi_j) = 0$ for most $i \neq j$ and so the linear system is sparse.

3.2 The Geometry Function

The root idea behind isogeometric analysis is that the basis used to exactly model the geometry will also serve as basis for the solution space of the numerical method. In CAGD and IGA the domain $\Omega \subset \mathbb{R}^d$ of the problem (3.3) is parametrized by a geometry function \mathbf{F} , which maps a reference or parameter domain $\Omega_0 \subset \mathbb{R}^d$ onto the physical domain Ω of the problem:

$$\mathbf{F} : \Omega_0 \rightarrow \Omega, \quad \mathbf{F}(\boldsymbol{\xi}) = \mathbf{x} = \begin{pmatrix} x_1 \\ \vdots \\ x_d \end{pmatrix}, \quad (3.8)$$

see Figure 3.1. Below we will apply B-splines (or NURBS) to define \mathbf{F} , but for the moment the geometry function is simply an invertible \mathcal{C}^1 -mapping from the parameter domain to the physical one. In our framework, $d = 2$ or $d = 3$ and $\Omega_0 = [0, 1]^d$ is the unit square or unit cube, respectively. However, we have in general $\Omega_0 \subset \mathbb{R}^z, z \leq d$. We stick in this work to $z = d$.

Since the problem is posed over the physical domain, it is necessary to use a change of variables to state it over the parameter domain. Integrals over Ω can be transformed into integrals over Ω_0 by means of the following integration rule

$$\int_{\Omega} \iota(\mathbf{x}) \, d\mathbf{x} = \int_{\Omega_0} \iota(\mathbf{F}(\boldsymbol{\xi})) |\det \mathbf{DF}(\boldsymbol{\xi})| \, d\boldsymbol{\xi}, \quad (3.9)$$

where \mathbf{DF} is the $d \times d$ Jacobian matrix, $\mathbf{DF}(\boldsymbol{\xi}) = (\partial F_i / \partial \xi_j)_{i,j=1,\dots,d}$.

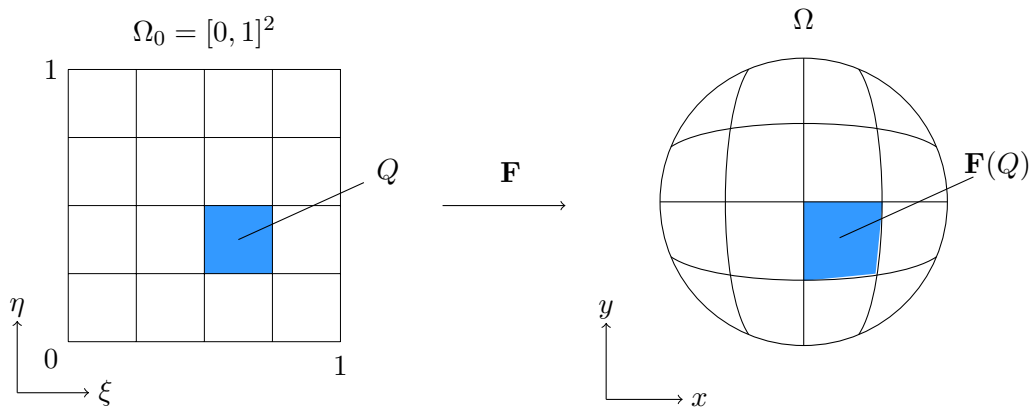


Figure 3.1. Parametrization of a physical domain $\Omega \subset \mathbb{R}^2$. The parameter domain is denoted by Ω_0 and corresponds to the unit square $[0, 1]^2$.

Once the problem is solved over Ω_0 , it is then transported over Ω again through \mathbf{F} . It is common to call these operations push forward and pull back, i.e., we say that an isogeometric map \mathbf{F} between manifolds can pull back something to the parameter domain Ω_0 or push it forward onto the physical domain Ω . The mapping \mathbf{F} is modifying also the bilinear form a and the linear form l of the problem. It can be shown that for $\hat{u} := u \circ \mathbf{F} \in \hat{\mathcal{V}} := \{\hat{v} \in H^1(\Omega_0), \hat{v} = 0 \text{ on } F^{-1}(\partial\Omega)\}$ a change of basis yields equivalent weak formulations:

$$u \in \mathcal{V} : a(u, v) = l(v) \quad \forall v \in \mathcal{V} \quad (3.10)$$

$$\iff \hat{u} \in \hat{\mathcal{V}} : \hat{a}(\mathbf{F})(\hat{u}, \hat{v}) = \hat{l}(\mathbf{F})(\hat{v}) \quad \forall \hat{v} \in \hat{\mathcal{V}}, \quad (3.11)$$

where the transformed bilinear and linear forms are obtained via the rule in (3.9). Since the Jacobian is bounded, the transformed operators are still bounded and coercive. Thus, by Lax-Milgram, the transformed problem (3.11) has a unique solution \hat{u} that has the form $\hat{u} = u \circ \mathbf{F}$.

From now on, we use the convention that a hat $\hat{\cdot}$ indicates something defined on the parameter domain Ω_0 .

Example 3.8 (Transformed weak form for Poisson's equation). *As already seen in the Example 3.5, the following Poisson's boundary value problem*

$$\begin{cases} -\Delta u = f & \text{in } \Omega, \\ u = 0 & \text{on } \partial\Omega, \end{cases} \quad (3.12)$$

is equivalent to find $u \in \mathcal{V}$ such that

$$\int_{\Omega} \nabla u \cdot \nabla v \, d\mathbf{x} = \int_{\Omega} f v \, d\mathbf{x} \quad \forall v \in \mathcal{V}, \quad (3.13)$$

where $\mathcal{V} = \{v \in H^1(\Omega), v = 0 \text{ on } \partial\Omega\}$.

Next assume that a parametrization of Ω is available as in (3.8). For the differentiation, the chain rule applied to $u(\mathbf{x}) = u(\mathbf{F}(\boldsymbol{\xi})) =: \hat{u}(\boldsymbol{\xi})$ yields, using a row vector notation for the gradient ∇u ,

$$\nabla_{\mathbf{x}} u(\mathbf{x}) = \nabla_{\boldsymbol{\xi}} \hat{u}(\boldsymbol{\xi}) \cdot \mathbf{D}\mathbf{F}(\boldsymbol{\xi})^{-1}. \quad (3.14)$$

Using the integration rule in (3.9), the integrals in the weak form (3.13) satisfy

$$a(u, v) = \int_{\Omega} \nabla u \cdot \nabla v \, d\mathbf{x} = \int_{\Omega_0} (\nabla \hat{u} \mathbf{D}\mathbf{F}^{-1}) \cdot (\nabla \hat{v} \mathbf{D}\mathbf{F}^{-1}) |\det \mathbf{D}\mathbf{F}| \, d\boldsymbol{\xi} = \hat{a}(\mathbf{F})(\hat{u}, \hat{v}) \quad (3.15)$$

and

$$l(v) = \int_{\Omega} f v \, d\mathbf{x} = \int_{\Omega_0} \hat{f} \hat{v} |\det \mathbf{D}\mathbf{F}| \, d\boldsymbol{\xi} = \hat{l}(\mathbf{F})(\hat{v}). \quad (3.16)$$

The weak form in the parametric coordinates is then

$$\int_{\Omega_0} (\nabla \hat{u} \mathbf{D}\mathbf{F}^{-1}) \cdot (\nabla \hat{v} \mathbf{D}\mathbf{F}^{-1}) |\det \mathbf{D}\mathbf{F}| \, d\boldsymbol{\xi} = \int_{\Omega_0} \hat{f} \hat{v} |\det \mathbf{D}\mathbf{F}| \, d\boldsymbol{\xi}. \quad (3.17)$$

In IGA the geometry function \mathbf{F} is expressed in terms of a spline geometry, here we consider a bivariate tensor product B-splines for $d = 2$ and a trivariate one for $d = 3$. Using the notation from the previous chapter we can write for the case $d = 2$ (corresponding to the one in Figure 3.1)

$$\mathbf{F}(\xi, \eta) = \sum_{i=1}^m \sum_{j=1}^n M_{i,p}(\xi) N_{j,q}(\eta) \mathbf{d}_{i,j}, \quad (3.18)$$

where $\mathbf{d}_{i,j} \in \mathbb{R}^2$ are the control points forming the control net associated to the parametrization. We remind that, in order to work with the unit square as parameter domain, the knot vectors Ξ and H are open, $\xi_1 = \dots = \xi_{p+1} = 0$ and $\xi_{m+1} = \dots = \xi_{m+p+1} = 1$, analogously $\eta_1 = \dots = \eta_{q+1} = 0$ and $\eta_{n+1} = \dots = \eta_{n+q+1} = 1$.

In $d = 3$ dimensions a trivariate tensor product B-splines is generated analogously, which results in

$$\mathbf{F}(\xi, \eta, \theta) = \sum_{i=1}^m \sum_{j=1}^n \sum_{k=1}^l M_{i,p}(\xi) N_{j,q}(\eta) L_{k,r}(\theta) \mathbf{d}_{i,j,k} \quad (3.19)$$

with an additional set of univariate B-splines $L_{k,r}$ and control points $\mathbf{d}_{i,j,k} \in \mathbb{R}^3$. The same treatment seen for Ξ and H will be considered for the knot vector Θ , i.e. Θ is open, $\theta_1 = \dots = \theta_{r+1} = 0$ and $\theta_{l+1} = \dots = \theta_{l+r+1} = 1$.

When applying Galerkin's method, the isogeometric analysis uses as basis functions for the finite-dimensional space the spline functions that describes \mathbf{F} . The space \mathcal{V}_h is then spanned by the push-forward of the spline basis functions of the geometry function \mathbf{F} onto the physical domain Ω . On the parameter domain the finite-dimensional space is spanned by $\hat{\mathcal{V}}_h = \text{span}\{\psi_i\}_{i=1,\dots,K}$, where $\psi_i = M_{j,p}N_{k,q}$ in the planar case and $\psi_i = M_{j,p}N_{k,q}L_{\omega,r}$ in the spatial case. The total number of degrees of freedom (DoF) is accordingly $K = mn$ or $K = mnl$, respectively. Then for the physical domain we obtain

$$\mathcal{V}_h = \text{span}\{\phi_i\}_{i=1,\dots,K} \quad \text{with} \quad \phi_i = \psi_i \circ \mathbf{F}^{-1}.$$

The projection step of Galerkin's method then boils down to inserting $\hat{u}_h = \sum \hat{u}_i \psi_i$ and $\hat{v}_h = \psi_j$, $j = 1, \dots, K$, into the weak form

$$\hat{u}_h \in \hat{\mathcal{V}}_h : \hat{a}(\mathbf{F})(\hat{u}_h, \hat{v}_h) = \hat{l}(\mathbf{F}(\hat{v}_h)) \quad \forall \hat{v}_h \in \hat{\mathcal{V}}_h. \quad (3.20)$$

3.2.1 Assembling the System

It is now clear that the spline functions span the finite-dimensional space in IGA. As already seen in Section 3.1.1, the variational equation in the finite-dimensional space leads to the linear system (3.7). It is important to notice that the stiffness matrix \mathbf{A} is sparse. Thus, for many combinations of i and j in the $K \times K$ stiffness matrix, $A_{i,j} = a(\phi_i, \phi_j) = 0$. This is an outcome of the properties of the spline functions seen in the previous chapter, that is the maximum number of functions with support on any given element (knot-span, rectangle and so on) is always fixed by the order of the polynomial. So for each element in the patch, the maximum number of functions that are not identically equal to zero throughout the patch is the same regardless of which element is under consideration. Let us denote this number of local shape functions by n_e . We build a $n_e \times n_e$ element stiffness matrix, \mathbf{A}_e , by posing a problem over a single element. This matrix is dense and it is common to call it local stiffness matrix.

The process of building the global stiffness matrix and the right-hand side vector is called assembly. Instead of looping through all of the global functions, taking global integrals to build \mathbf{A} one entry at a time, we will loop through the elements, building local stiffness matrices as we go. Every entry of each of these local stiffness matrices will then be added to the appropriate spot in the global one. In this way we need not expend effort integrating functions over regions in which we know a priori that they are zero.

The actual computation of each entry of the local stiffness matrix and of the right-hand side vector is performed by quadrature rules. A Gaussian quadrature rule is

used to compute numerical integration. We refer to [31, 33] for additional details on numerical integration.

Once Galerkin's method has been applied and an approximation u_h has been obtained, it is fair to query how good the approximation is.

3.2.2 A Priori Error Estimates

We use some abbreviations for the standard norms

$$\begin{aligned} \|\cdot\|_\infty &:= \operatorname{ess\,sup}_{\mathbf{x} \in \Omega} |\cdot(\mathbf{x})|, \\ \|\cdot\| &:= \|\cdot\|_{L^2(\Omega)} = \left(\int_\Omega |\cdot(\mathbf{x})|^2 \, d\mathbf{x} \right)^{1/2}, \\ \|\cdot\|_E &:= \sqrt{a(\cdot, \cdot)}, \text{ the energy norm,} \\ \|\cdot\|_p &:= \|\cdot\|_{H^p(\Omega)}, \end{aligned}$$

where $H^p(\Omega)$ is a Sobolev space defined as the subset of functions $f \in L^2(\mathbb{R})$ such that f and its weak derivatives up to order p have a finite L^2 -norm. For more details on Sobolev spaces see [12].

For boundary value problems with sufficiently regular exact solution and data, standard error estimates from FEM ([38, 57]) are also valid for IGA:

$$\|u - u_h\|_E \leq Ch^{p+1-m} \|u\|_{p+1}, \quad (3.21)$$

$$\|u - u_h\| \leq Ch^\sigma \|u\|_{p+1}, \quad (3.22)$$

where $\sigma = \min\{p+1, 2(p+1-m)\}$, $2m$ is the order of the differential operator L from which $a(\cdot, \cdot)$ is derived, and p is the degree of the B-spline/NURBS basis functions considered.

Since we consider L as a linear uniformly elliptic differential operator of second order we have $m = 1$ and $\sigma = \min\{p+1, 2p\} = p+1$, thus

$$\|u - u_h\|_E \leq Ch^p \|u\|_{p+1}, \quad (3.23)$$

$$\|u - u_h\| \leq Ch^{p+1} \|u\|_{p+1}. \quad (3.24)$$

The technical details of the process to obtain these error estimates in isogeometric analysis can be found in [6, 19], where they prove a sequence of lemmas leading up to an approximation result that includes also the gradient \mathbf{DF} of the mapping. The term depending on the geometry function presents no problem because it does not change as the mesh is refined and thus does not affect the rate of the convergence. Without going through all the lemmas proved in [6], we recall here the final result for the global error estimate. Let k and l be integer indices such that $0 \leq k \leq l \leq p+1$, and let $u \in H^l(\Omega)$, then

$$\sum_{e=1}^{n_{el}} |u - \Pi_k u|_{H^k(\Omega_e)}^2 \leq C \sum_{e=1}^{n_{el}} h_e^{2(l-k)} \sum_{i=0}^l \|\mathbf{DF}\|_\infty^{2(i-l)} |u|_{H^i(\Omega_e)}^2, \quad (3.25)$$

where $\Pi_k u$ is the optimal interpolate and h_e is the element size in the physical domain. The constant C depends on p and the shape (but not size) of the domain Ω , as well as on the shape regularity of the mesh.

So the isogeometric analysis solution obtained using NURBS of degree p has the same order of convergence as we would expect in a FEM setting using classical basis

functions with a polynomial of degree p . This is a strong result and it is independent of the order of continuity that the mesh possesses. Indeed in the following section an L-shape geometry with different parametrizations will be considered. It will be evident that, even though the continuity of the meshes is different, the order of convergence results the same.

3.3 Examples

In this section we consider two different geometries, an L-shape and a disk. On both of them Poisson's equation with zero Dirichlet boundary conditions is going to be solved with the standard Galerkin isogeometric analysis. We solve the partial differential equation by an extension of the ISOGAT package [63].

We recall here the problem:

$$\begin{cases} -\Delta u &= f & \text{in } \Omega, \\ u &= 0 & \text{on } \partial\Omega. \end{cases} \quad (3.26)$$

3.3.1 L-Shape

We consider a B-spline surface, as in (2.4), with $p, q = 2$, knot vectors

$$\begin{aligned} \Xi &= \{0, 0, 0, 1, 1, 1\} \\ H &= \{0, 0, 0, 0.5, 0.5, 1, 1, 1\}, \end{aligned}$$

and control points

$$\begin{aligned} &\{(-1.00, 1.00) \quad (-1.00, 0.00) \quad (-1.00, -1.00) \quad (0.00, -1.00) \quad (1.00, -1.00); \\ &\quad (-0.60, 1.00) \quad (-0.55, 0.00) \quad (-0.50, -0.50) \quad (0.00, -0.55) \quad (1.00, -0.60); \\ &\quad (0.00, 1.00) \quad (0.00, 0.50) \quad (0.00, 0.00) \quad (0.50, 0.00) \quad (1.00, 0.00)\}. \end{aligned}$$

The surface generated, our physical domain Ω , is represented in Figure 3.2 (right).

We consider as right-hand side the function

$$f = 2\pi^2 \sin(\pi x) \sin(\pi y).$$

The analytical solution of (3.26) is then

$$u(x, y) = \sin(\pi x) \sin(\pi y).$$

The refinements in the ISOGAT code are performed by using the knot insertion technique and they are restricted to global h -refinement. So in the middle of each nonempty knot-span a knot is inserted and the new control points are calculated. See Figure 3.3 for the control points on the L-shape domain after one refinement. In Figure 3.4 the approximate solution and the distribution of the absolute error after two refinements are shown. Such an error plot, however, contains little information on the convergence of the method. In order to study the convergence and the quality of different parametrizations, we introduce another geometry map that generates the same L-shape as B-spline surface. This time we construct a parametrization that is globally \mathcal{C}^1 -continuous, note indeed that the first parametrization had a \mathcal{C}^0 -edge in the interior of the domain, the one connecting the corners $(-1, -1)$ and $(0, 0)$. To do so we change the knot vector H into $\{0, 0, 0, 0.5, 1, 1, 1\}$ and the control points into

$$\begin{aligned} &\{(-1.00, 1.00) \quad (-1.00, -1.00) \quad (-1.00, -1.00) \quad (1.00, -1.00); \\ &\quad (-0.65, 1.00) \quad (-0.70, 0.00) \quad (0.00, -0.70) \quad (1.00, -0.65); \\ &\quad (0.00, 1.00) \quad (0.00, 0.00) \quad (0.00, 0.00) \quad (1.00, 0.00)\}, \end{aligned}$$

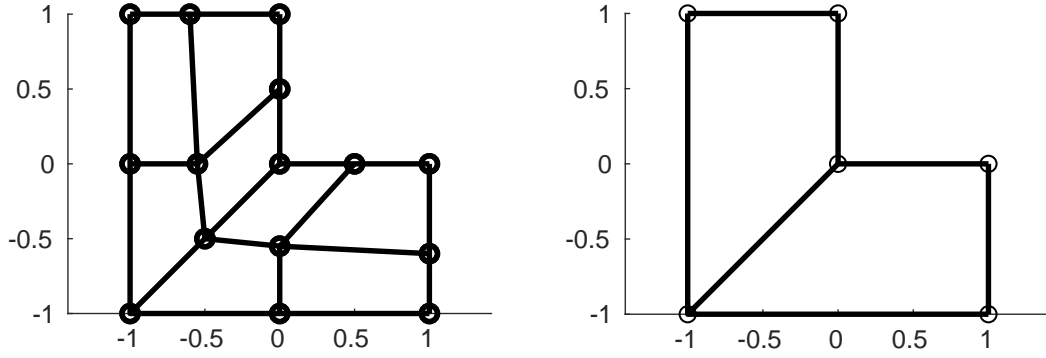


Figure 3.2. Geometry description of the L-shape: control point grid (left), physical domain with image of the knot lines (right)

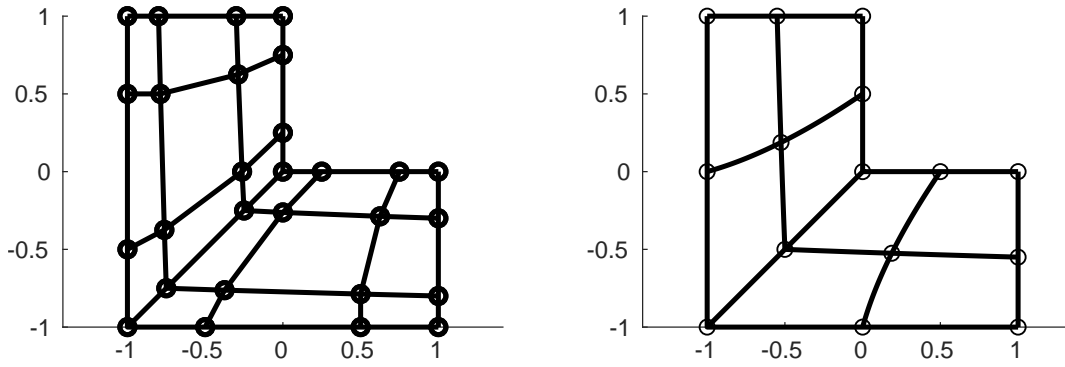


Figure 3.3. Geometry description of the L-shape after one global h -refinement: control point grid (left), physical domain with image of the knot lines (right)

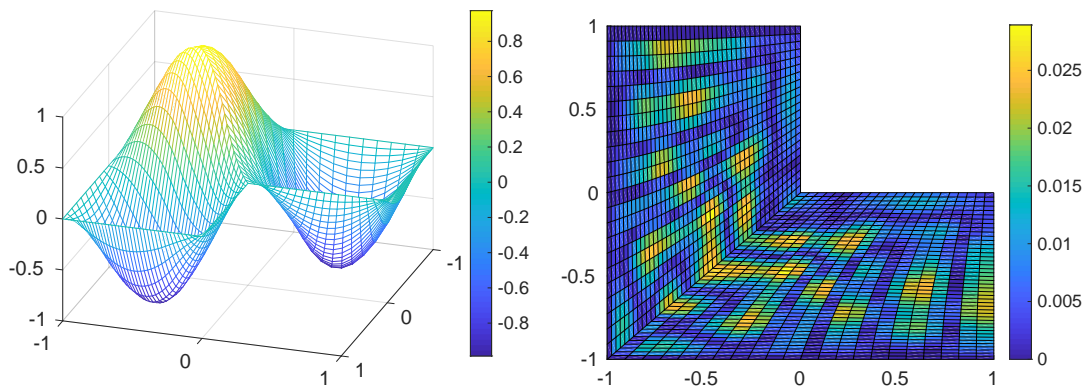


Figure 3.4. Numerical solution (left) and absolute error (right) after two refinements

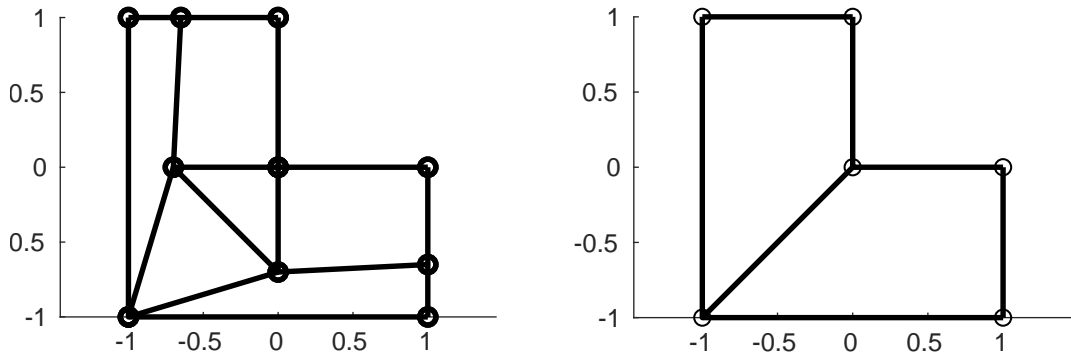


Figure 3.5. Geometry description of the L-shape in order to get a globally \mathcal{C}^1 -continuous parametrization: control point grid (left), physical domain with image of the knot lines (right).

see Figure 3.5 for the new control point grid.

To compare the two parametrizations we first calculate the energy norm

$$||u_h||_E = \sqrt{\mathbf{u}^T \mathbf{A} \mathbf{u}}$$

of the numerical approximation. In Figure 3.6(a) we have plotted the energy norm for several refinement steps versus the mesh size h . In the numerical simulation we consider h as one over the square root of the number of degrees of freedom, i.e.,

$$h = (\#\text{DoF})^{-1/2}. \quad (3.27)$$

Both numerical solutions tend to the same maximum value when refining the grids. This confirms the theoretical result that $||u_h||_E \rightarrow ||u||_E$ from below for any convergent Galerkin projection method [31]. As seen in the previous section, the convergence estimates feature a factor depending on the geometry function \mathbf{F} , i.e. the parametrization has an influence on the accuracy. We can observe that the first parametrization behaves better especially in the case of coarse meshes with bigger mesh size. This is also confirmed by Figure 3.6(b), where we have plotted the L^2 -error norm $||u - u_h||$ of both parametrizations for several refinement steps. As expected both the geometries show optimal convergence rates of order three for the global L^2 -error. However, the error is slightly smaller in the \mathcal{C}^0 -parametrization.

As another measure of the parametrization quality we can consider the condition number of the stiffness matrix. Figure 3.7 shows the behavior of the condition number of the stiffness matrix arising from the two parametrizations. When decreasing the mesh size, the first parametrization demonstrates the lowest condition number with a growth rate of $1/h^2$. While the second parametrization has bigger condition numbers with a growth rate of $1/h^3$. This is an effect of the two singularities in the corner $(-1, -1)$ and $(0, 0)$ of the second parametrization, as depicted in Figure 3.8. There the determinant of the Jacobian of the geometry function has been plotted. This comes from the fact that these two control points are present in the control net with multiplicity two.

3.3.2 Unit Disk

The disk geometry belongs to the class of conic intersections that can only be described by rational splines and not by polynomial splines. We consider a disk that has radius

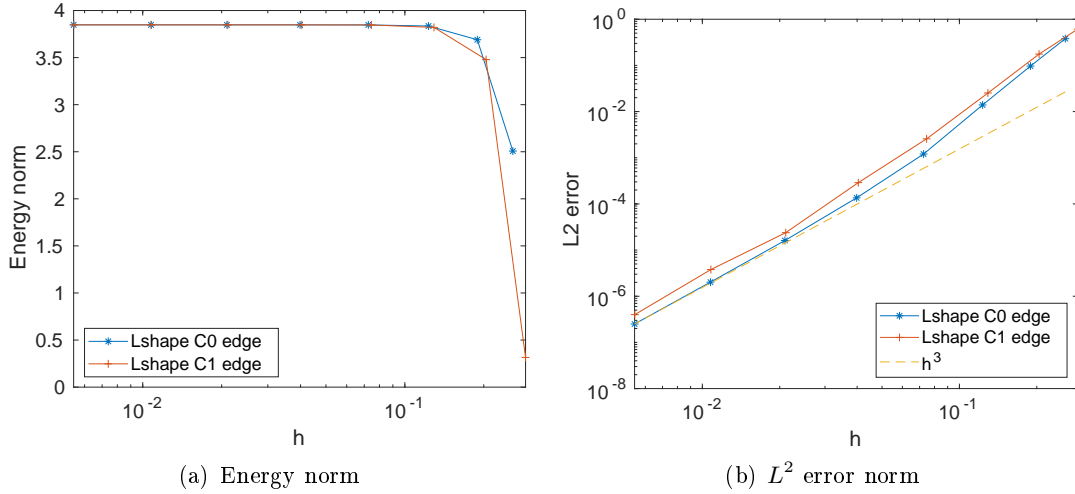


Figure 3.6. Comparison of the two different parametrizations for the L-shape domain: on the left the energy norm $\|u_h\|_E$ and on the right the L^2 error norm $\|u - u_h\|$

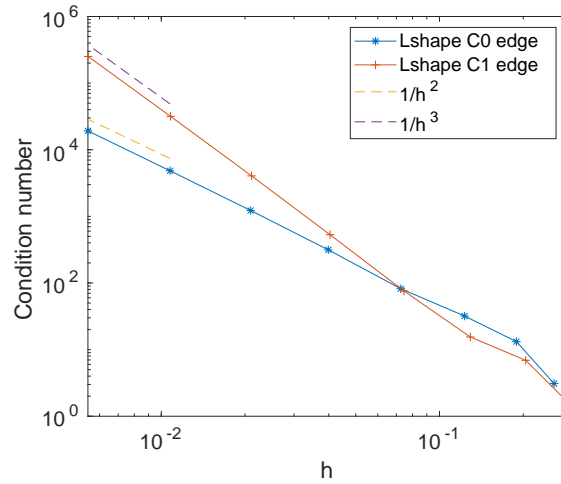


Figure 3.7. Comparison of the condition numbers of the stiffness matrix arising from the two different discretizations

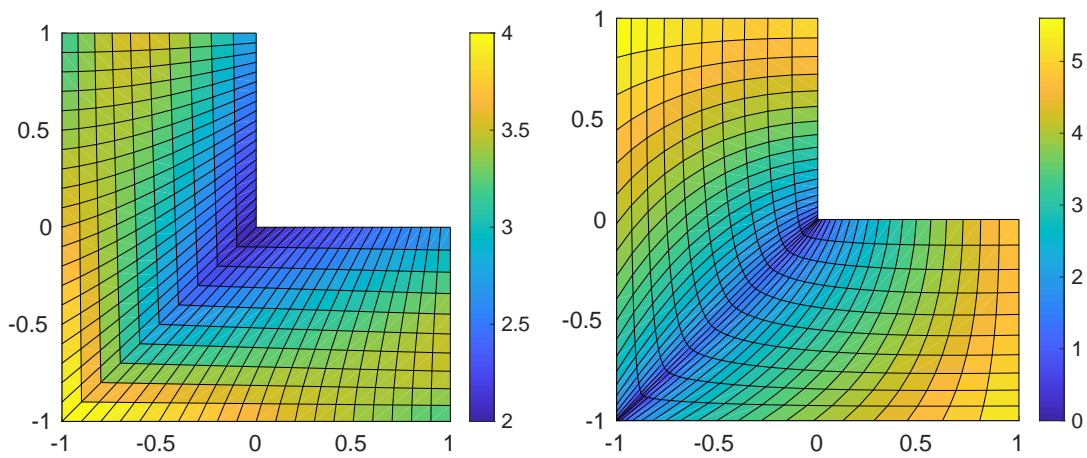
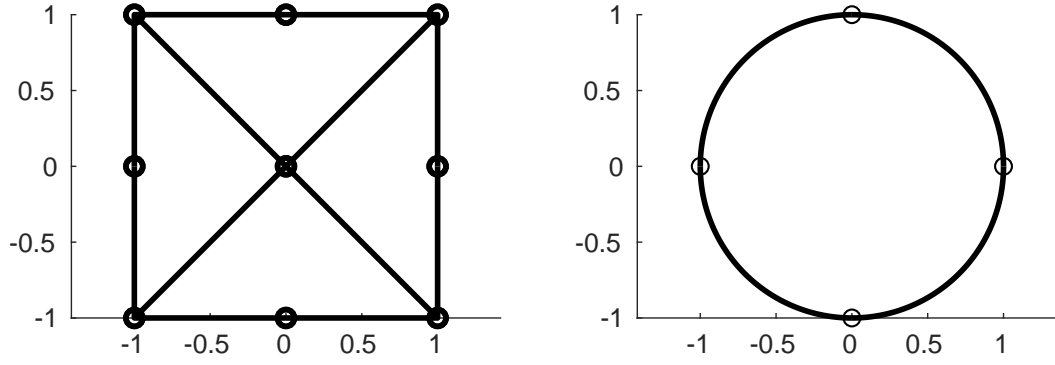


Figure 3.8. Determinant of the Jacobian of the geometry function for the two different parametrizations for the L-shape geometry: on the left the first parametrization, on the right the \mathcal{C}^1 -continuous parametrization



(a) Control point grid as defined at the first iteration

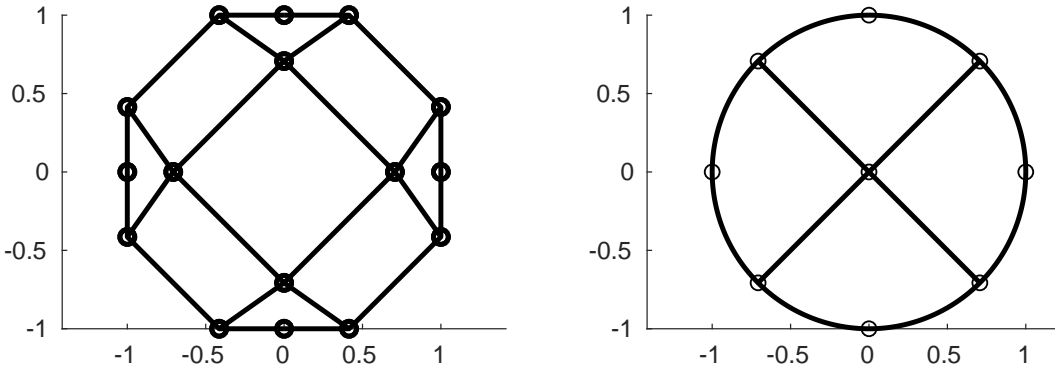

 (b) Control point grid at the second iteration. An h -refinement has been performed.

Figure 3.9. Geometry description of the disk: control point grid (left), physical domain (right)

1 and is centered in $(0,0)$. This unit disk can be described using a NURBS surface with $p, q = 2$, knot vectors

$$\Xi = \{0, 0, 0, 1, 1, 1\},$$

$$H = \{0, 0, 0, 1, 1, 1\},$$

weights $\omega = \{1, \sqrt{2}/2, 1, \sqrt{2}/2, 1, \sqrt{2}/2, 1, \sqrt{2}/2, 1\}$ and control points

$$\begin{Bmatrix} (-1, 0) & (-1, -1) & (0, -1); \\ (-1, 1) & (0, 0) & (1, -1); \\ (0, 1) & (1, 1) & (1, 0) \end{Bmatrix},$$

as in Figure 3.9(a) (left). The physical domain Ω is represented in Figure 3.9(a) (right). The control point grid after one global h -refinement is depicted in Figure 3.9(b) (left). We consider as right-hand side function $f = 1$, then the analytical solution of (3.26) is

$$u(x, y) = \frac{1 - x^2 - y^2}{4}.$$

The numerical solution and the absolute error after two refinements are shown in Figure 3.10, while in Figure 3.11 the energy norm, the L^2 -error norm and the condition number of the stiffness matrix are plotted for several refinement steps. Also in this case the L^2 -error norm has the expected order 3. Another noticeable aspect are the

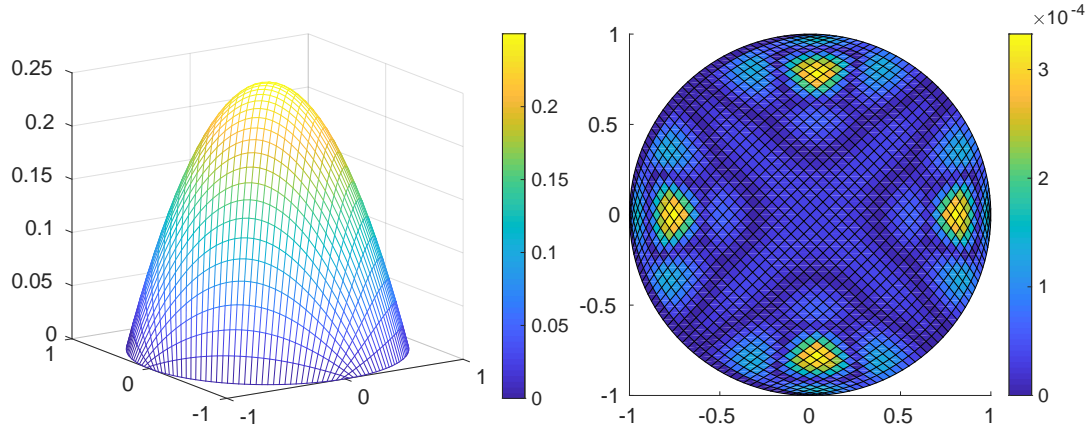


Figure 3.10. Numerical solution (left) and absolute error (right) on the disk after two refinements when right-hand side function $f = 1$

four singularities of the Jacobian \mathbf{DF} that arise for this particular geometry function (see the determinant of the Jacobian in Figure 3.12). The singularities lie on the circle line and are marked by black dots in Figure 3.9(a) on the right. However, in our numerical simulations, the quadrature for evaluating the integrals of the weak form associated to (3.26) remained stable and did not suffer from the singularities, even in close proximity. Indeed the Gauss-Legendre quadrature uses as quadrature points only points inside the parameter domain [1]. Hence, since the singularities lie on its boundary, they do not affect the quadrature. Due to these four singularities the condition number grows with rate $1/h^3$ (Figure 3.11(b)).

We now change the right-hand side function

$$f = 3\pi \left(2 \sin \left(\frac{3}{2}\pi R \right) + 3\pi R \cos \left(\frac{3}{2}\pi R \right) \right), \quad \text{with } R = x^2 + y^2. \quad (3.28)$$

The analytical solution is then

$$u(x, y) = \cos \left(\frac{3}{2}\pi R \right).$$

The numerical solution and the absolute error after three refinements are shown in Figure 3.13, while in Figure 3.14 the energy norm, the L^2 -error norm and the condition number of the stiffness matrix are plotted with respect to the size h of the mesh. As expected the order of convergence of the L^2 -error norm is 3 (Figure 3.14(b)). Since we only changed the right-hand side function, the condition number of the stiffness matrix is the same and it increases as in Figure 3.11(b).

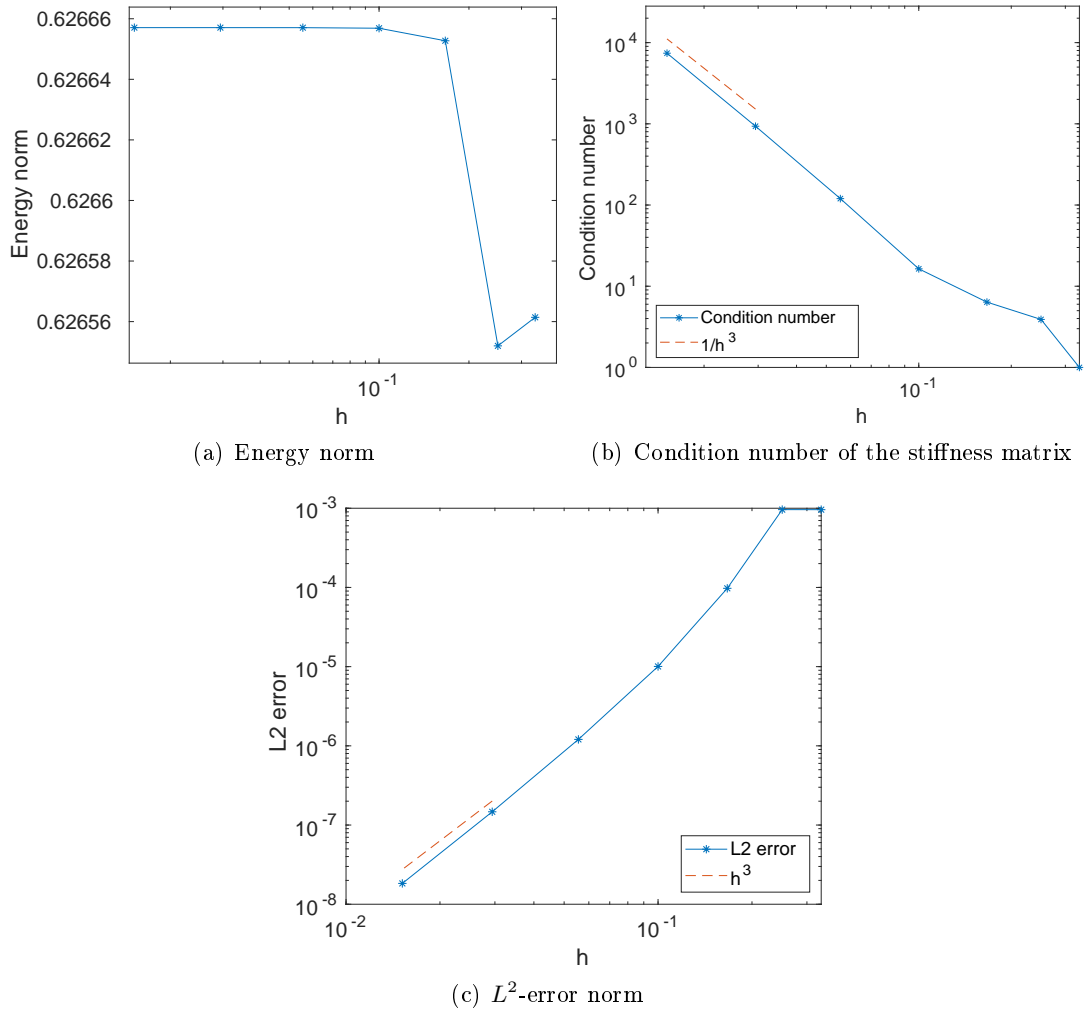


Figure 3.11. Energy norm $\|u_h\|_E$, L^2 -error norm $\|u - u_h\|$ and condition number of the stiffness matrix for the disk geometry when right-hand side function $f = 1$

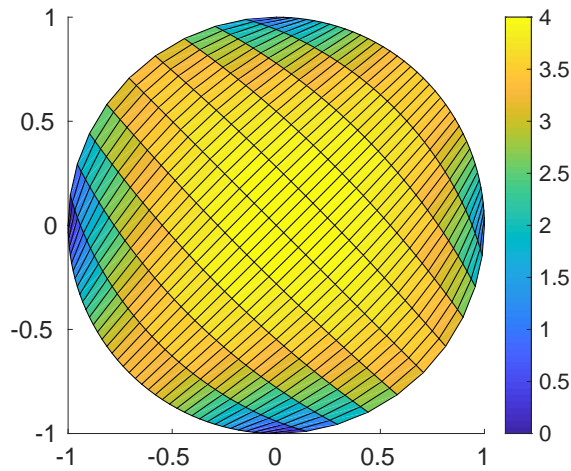


Figure 3.12. Determinant of the Jacobian of the geometry function for the disk geometry

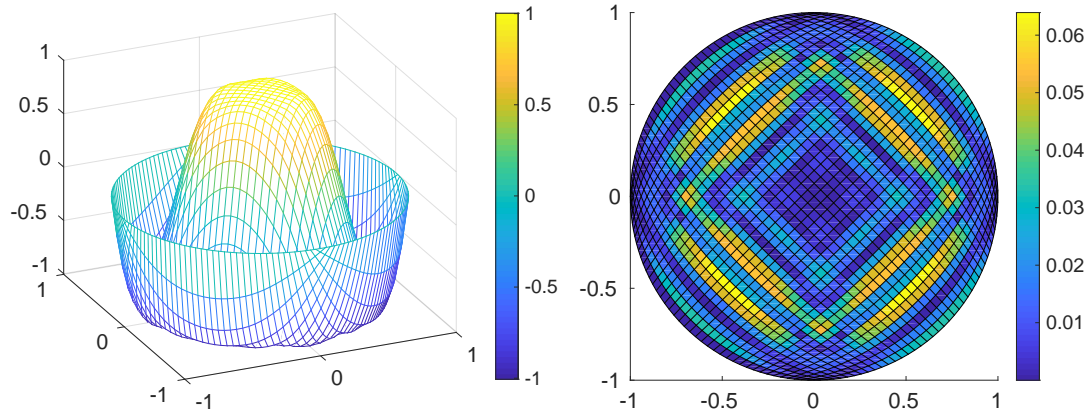


Figure 3.13. Numerical solution (left) and absolute error (right) on the disk after three refinements when right-hand side function f as in (3.28)

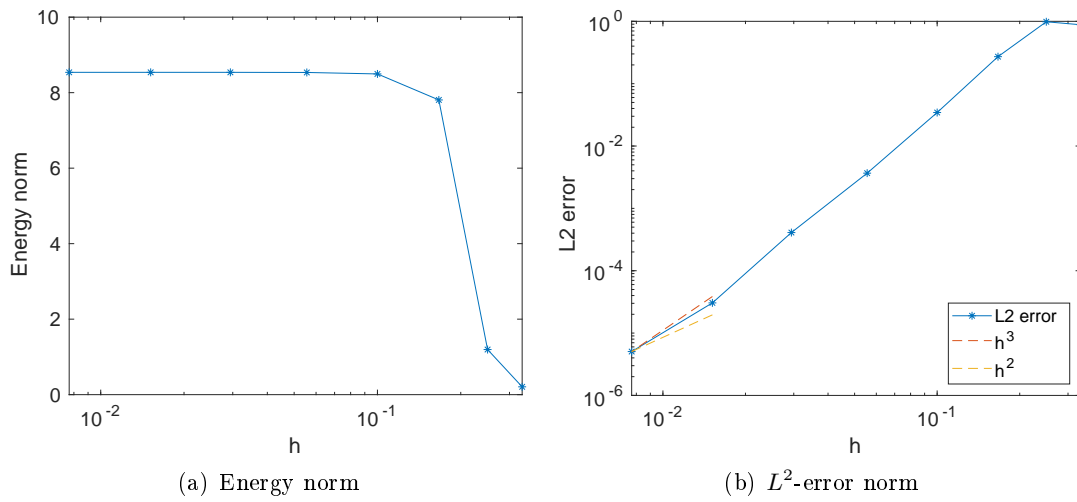


Figure 3.14. Energy norm $\|u_h\|_E$ and L^2 -error norm $\|u - u_h\|$ for the disk geometry when right-hand side function f as in (3.28)

Scaled Boundary Isogeometric Analysis

In isogeometric analysis the parametrization of the computational domain plays a crucial role. In Chapter 3 we have seen how this parametrization can be written using tensor product B-splines. In this chapter we introduce a class of parametrizations that can be viewed as a generalization of classical polar coordinates, the scaled boundary parametrizations (SB-parametrizations). These are easy to construct and especially attractive if only a boundary description of the domain is available. Indeed, classically, objects in CAGD are defined by a boundary representation (B-Rep), where only the surfaces of the objects with their corresponding edges and nodes are stored. In order to construct the interior mesh, it appears then easier and faster to build a beam of rays from the surface to a center previously chosen. Based on this parametrization we introduce the scaled boundary isogeometric analysis (SB-IGA). Our approach is inspired by the scaled boundary finite element method (SB-FEM) [55, 56] and its extension to IGA [13, 39, 43], which both rely on the B-Rep format in CAGD [58]. Moreover we explain the relation between the standard Galerkin-based IGA, presented in the previous chapter, and the SB-IGA. The majority of what will be discussed in the next sections can be found also in [2].

In Section 4.1 we present the SB-parametrizations and we observe an important property, the multiplicative structure of their Jacobian. Then, in Section 4.2 we present the scaled boundary isogeometric analysis. Considering an SB-parametrization as geometry function also in the standard IGA, we compare the two methods at a weak analytical level and at a discrete level for a linear problem. Furthermore, we state an equivalence theorem between the two approaches. Afterwards, in Section 4.3 we analyze the singularity in the scaling center. We conclude the chapter with some numerical examples in Section 4.4. We solve Poisson's equation with zero Dirichlet boundary conditions with SB-IGA on different star-shaped domains. We consider and compare the numerical results for different SB-parametrizations.

4.1 Scaled Boundary Parametrizations

In this section we introduce the idea behind a scaled boundary parametrization and we show some of its properties.

As seen in Section 3.2, the goal of a parametrization is to find a geometry function \mathbf{F} that goes from a parameter domain Ω_0 , typically the unit square or the unit cube, into the physical domain $\Omega \subset \mathbb{R}^d$, $d = 2, 3$.

We consider now the case $d = 2$, so $\Omega \subset \mathbb{R}^2$ and $\Omega_0 = [0, 1]^2$. An SB-parametrization

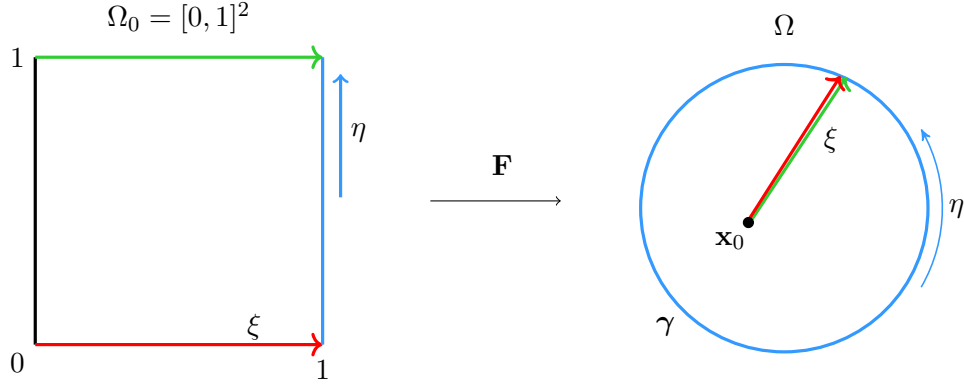


Figure 4.1. Scaled boundary parametrization of a physical domain $\Omega \subset \mathbb{R}^2$, where only the boundary curve γ is available. The parameter domain is denoted by Ω_0 and corresponds to the unit square $[0, 1]^2$.

can be constructed as follows. We first assume that Ω is a star-shaped domain and that only its boundary is available. This is described by a B-spline curve γ

$$\gamma(\eta) := \sum_{j=1}^n N_{j,q}(\eta) \mathbf{c}_j, \quad (4.1)$$

where $N_{j,q}$ are the univariate B-splines of degree q with open knot vector

$$H = \{\underbrace{0, \dots, 0}_{q+1}, \eta_{q+2}, \dots, \eta_n, \underbrace{1, \dots, 1}_{q+1}\}.$$

We require also $\eta \in [0, 1]$ for the independent variable and we consider a closed curve with $\gamma(0) = \gamma(1)$. This can be achieved by an open knot vector and control points $\mathbf{c}_1 = \mathbf{c}_n$.

Next, we pick a point $\mathbf{x}_0 \in \Omega$, the scaling center, from which all points inside the domain are visible and we connect it with the boundary through rays that emanate from it, see Figure 4.1. A ray from the scaling center to a control point \mathbf{c}_j can be parametrized as

$$(1 - \xi)\mathbf{x}_0 + \xi\mathbf{c}_j, \quad \xi \in [0, 1]. \quad (4.2)$$

Replacing the control point \mathbf{c}_j by any point on the boundary curve (4.1), we obtain, by the partition of unity,

$$\begin{aligned} (1 - \xi)\mathbf{x}_0 + \xi\gamma(\eta) &= (1 - \xi) \sum_{j=1}^n N_{j,q}(\eta) \mathbf{x}_0 + \xi \sum_{j=1}^n N_{j,q}(\eta) \mathbf{c}_j \\ &= \sum_{i=1}^2 \sum_{j=1}^n M_{i,1}(\xi) N_{j,q}(\eta) \mathbf{d}_{i,j} = \mathbf{F}(\xi, \eta), \end{aligned} \quad (4.3)$$

where $M_{1,1}(\xi) = 1 - \xi$, $M_{2,1}(\xi) = \xi$ are the linear B-splines depending only on the parameter ξ and $\mathbf{d}_{i,j}$ are control points defined as $\mathbf{d}_{1,j} := \mathbf{x}_0$, $\mathbf{d}_{2,j} := \mathbf{c}_j$, $j = 1, \dots, n$.

The bivariate parametrization $\mathbf{F}(\xi, \eta)$ maps the unit square to the physical domain with multiple control point $\mathbf{d}_{1,j} := \mathbf{x}_0$, $j = 1, \dots, n$, in the scaling center and the other control points $\mathbf{d}_{2,j} := \mathbf{c}_j$, $j = 1, \dots, n$, inherited from the boundary curve. That is to say, the left vertical edge of the unit square collapses into the scaling center, while the

right vertical edge is mapped into the boundary, see Figure 4.1. The lower and upper edges are mapped inside the domain as the same ray from the scaling center to the curve. In order to solve an equation on this parametrized domain, it will be necessary to impose some periodic conditions along this ray.

Note that the geometry function in (4.3) features the same structure of the geometry function expressed in terms of a bivariate tensor product B-splines in (3.18), where only $m = 2$ linear B-splines are considered in the ξ -direction and n B-splines in the η -direction. The ξ -direction is also called scaling or radial direction.

In some cases it will be advantageous to write the geometry function in a more compact form:

$$\mathbf{F}(\xi, \eta) = \mathbf{x}_0 + \xi(\mathbf{C} \cdot \mathbf{N}(\eta) - \mathbf{x}_0), \quad (4.4)$$

where the matrix $\mathbf{C} := (\mathbf{c}_1, \dots, \mathbf{c}_n) \in \mathbb{R}^{2 \times n}$ contains the control points of the boundary curve and for all η the vector $\mathbf{N}(\eta) := (N_{1,q}(\eta), \dots, N_{n,q}(\eta))^T \in \mathbb{R}^n$ the B-splines. This compact form is the usual notation for the geometry function in the SB-IGA [14, 15, 43].

Finally, we extend the bivariate spline parametrization in (4.3) and we apply both knot insertion and degree elevation in the radial direction, which maintain the rays that emanate from the scaling center but leads to a more general formulation

$$\mathbf{F}(\xi, \eta) = \sum_{i=1}^m \sum_{j=1}^n M_{i,p}(\xi) N_{j,q}(\eta) \bar{\mathbf{d}}_{i,j}. \quad (4.5)$$

The multiple control point in the scaling center is still present here, i.e., $\bar{\mathbf{d}}_{1,j} = \mathbf{x}_0$ for $j = 1, \dots, n$, and for the control points of the boundary curve $\bar{\mathbf{d}}_{m,j} = \mathbf{c}_j$, $j = 1, \dots, n$. The other extra control points $\bar{\mathbf{d}}_{i,j}$, $i = 2, \dots, m-1$, $j = 1, \dots, n$, are computed from the steps of knot insertion and degree elevation seen in Section 2.3. In this way, we obtain a finer parametrization that still preserves the scaled boundary idea and it possesses a discretization in both ξ and η that can be used as isogeometric mesh for a numerical simulation.

For the case $d = 3$ the construction of the geometry function with a scaled boundary parametrization is quite similar. We now have Ω a star-shaped solid and the unit cube as a parameter domain, $\Omega_0 = [0, 1]^3$, and only the surface of the solid is given. This is parametrized by a B-spline surface

$$\mathbf{\Gamma}(\eta, \theta) := \sum_{j=1}^n \sum_{k=1}^l N_{j,q}(\eta) L_{k,r}(\theta) \mathbf{d}_{j,k}, \quad (4.6)$$

where now $\mathbf{d}_{j,k}$ are control points in \mathbb{R}^3 . Following the same steps of the case $d = 2$ we obtain

$$\mathbf{F}(\xi, \eta, \theta) = (1 - \xi)\mathbf{x}_0 + \xi \mathbf{\Gamma}(\eta, \theta) = \sum_{i=1}^2 \sum_{j=1}^n \sum_{k=1}^l M_{i,1}(\xi) N_{j,q}(\eta) L_{k,r}(\theta) \mathbf{d}_{i,j,k}, \quad (4.7)$$

where $\mathbf{x}_0 \in \mathbb{R}^3$ and $\mathbf{d}_{i,j,k} \in \mathbb{R}^3$ are the new control points defined as $\mathbf{d}_{1,j,k} = \mathbf{x}_0 \forall j, k$, and $\mathbf{d}_{2,j,k} = \mathbf{d}_{j,k}$, $j = 1, \dots, n$, $k = 1, \dots, l$. So the scaling center is always a multiple control point.

Also in this case it is possible to write a general formulation after refining the mesh in the scaling direction. We obtain then

$$\mathbf{F}(\xi, \eta, \theta) = \sum_{i=1}^m \sum_{j=1}^n \sum_{k=1}^l M_{i,p}(\xi) N_{j,q}(\eta) L_{k,r}(\theta) \bar{\mathbf{d}}_{i,j,k}, \quad (4.8)$$

with $\bar{\mathbf{d}}_{1,j,k} = \mathbf{d}_{1,j,k} = \mathbf{x}_0 \ \forall j, k$, and $\bar{\mathbf{d}}_{m,j,k} = \mathbf{d}_{2,j,k}$, $j = 1, \dots, n$, $k = 1, \dots, l$. The other control points $\bar{\mathbf{d}}_{i,j,k}$, $i = 2, \dots, m-1$, $j = 1, \dots, n$, $k = 1, \dots, l$, are derived from the algorithms of knot insertion and degree elevation.

For more details and examples of SB-IGA for the three-dimensional case we refer to [15].

We now want to study the regularity and smoothness of the SB-parametrization. For this purpose, it is convenient to consider the compact form in (4.4). The Jacobian of the geometry function reads

$$\mathbf{DF}(\xi, \eta) = (\mathbf{C} \mathbf{N}(\eta) - \mathbf{x}_0 \mid \xi \mathbf{C} \mathbf{N}'(\eta)) = \begin{pmatrix} \mathbf{C}_1 \mathbf{N}(\eta) - x_{0,1} & \mathbf{C}_1 \mathbf{N}'(\eta) \\ \mathbf{C}_2 \mathbf{N}(\eta) - x_{0,2} & \mathbf{C}_2 \mathbf{N}'(\eta) \end{pmatrix} \begin{pmatrix} 1 & 0 \\ 0 & \xi \end{pmatrix}. \quad (4.9)$$

Here we used the notation $\mathbf{C}_1 := \mathbf{C}(1, :) \in \mathbb{R}^{1 \times n}$ and $\mathbf{C}_2 := \mathbf{C}(2, :) \in \mathbb{R}^{1 \times n}$ for the first and for the second row of \mathbf{C} , respectively. Furthermore $\mathbf{x}_0^T = (x_{0,1}, x_{0,2})$ and the derivative with respect to η is written as $\mathbf{N}' = \partial \mathbf{N} / \partial \eta$.

The determinant of the Jacobian is given by

$$\det \mathbf{DF}(\xi, \eta) = \xi J(\eta), \quad (4.10)$$

where

$$J(\eta) := \mathbf{C}_1 \mathbf{N}(\eta) \mathbf{C}_2 \mathbf{N}'(\eta) - x_{0,1} \mathbf{C}_2 \mathbf{N}'(\eta) - \mathbf{C}_1 \mathbf{N}'(\eta) \mathbf{C}_2 \mathbf{N}(\eta) + x_{0,2} \mathbf{C}_1 \mathbf{N}'(\eta). \quad (4.11)$$

We observe a multiplicative structure in the Jacobian. This allows a direct analysis of the parametrization in terms of regularity and smoothness. Clearly, in the scaling center where $\xi = 0$, the parametrization \mathbf{F} becomes singular. For the derivative in η -direction, we have $\partial \mathbf{F}(\xi = 0, \eta) / \partial \eta = \mathbf{0}$. It is possible to determine the smoothness and the regularity of the parametrization directly from the ones of the boundary curve. If γ is of class \mathcal{C}^k , then \mathbf{F} is of class \mathcal{C}^k as well. If γ possesses points of reduced smoothness, e.g. its knot vector has a multiple knot such that a certain control point \mathbf{c}_j lies on the curve, then the ray $(1 - \xi)\mathbf{x}_0 + \xi \mathbf{c}_j$, $\xi \in [0, 1]$, which runs from the scaling center to \mathbf{c}_j , will maintain the smoothness and it will form a \mathcal{C}^0 -edge in the interior. Furthermore, if γ is injective, the parametrization will also be injective except for the scaling center.

We remark that the boundary curve, as well as the boundary surface in the case $d = 3$, could be expressed in terms of NURBS basis functions, instead of B-splines. The construction of a scaled boundary parametrization when NURBS are considered stays the same. Moreover, all the properties discussed so far, including the multiplicative structure of the Jacobian, are preserved. The so-called multi-degree polar splines have been introduced to circumvent the singularity in the scaling center [61]. That framework, however, leads to a different type of splines, while we stick here to standard tensor product B-splines.

4.2 Scaled Boundary IGA and Galerkin-Based IGA

In the previous chapter we have seen how the standard IGA proceeds to solve a partial differential equation. In the first step the weak form of the problem is obtained from the strong form using a test function and the integration by parts. When considering a domain whose parametrization is a scaled boundary parametrization, it is possible to derive the weak form in another way. In the context of IGA, this leads to the scaled boundary isogeometric analysis.

As seen in Section 4.1, an SB-parametrization presents two independent variables (or three in the case $d = 3$). Using the terminology of the polar coordinates, the variable η defines the so-called angular or circumferential direction, while the variable ξ defines the scaling or radial direction. For $\xi = 1$ the variable η describes exactly the boundary curve. The idea of the scaled boundary isogeometric analysis is to derive the final weak form in two steps. In the first step a Galerkin projection is considered with respect to the circumferential coordinate η , that is the weak form is derived from the strong form only in the η -direction and so the test function will depend only on η and the integration is only performed with respect to η as well. Then, the weak form is also considered in the ξ -direction.

In this section we consider a scaled boundary parametrization \mathbf{F} , as in 4.4, and we use it in the standard IGA and in the SB-IGA as geometry function. Besides how the weak form is derived, another difference between these two methods is the moment when the transformation \mathbf{F} is used. For standard IGA the transformation \mathbf{F} is applied to the weak form, while in the SB-IGA to the strong form at the beginning. More details will be shown later.

For the ease of presentation, we consider, as model problem, Poisson's equation with zero Dirichlet boundary conditions (see Example 3.8 for the definition of the problem in the strong and weak forms and its transformation under \mathbf{F}). However, our results can be generalized to linear elliptic PDEs with the usual properties of coercivity and continuity. For our purposes, it is now advantageous to adopt a general viewpoint from differential geometry, where the Laplace operator is extended to operate on functions defined on surfaces in Euclidean space and on Riemannian manifolds, see Berger [10]. We define the metric tensor or first fundamental form

$$\mathbf{g}(\xi) := \mathbf{D}\mathbf{F}(\xi)^T \mathbf{D}\mathbf{F}(\xi), \quad (4.12)$$

which has determinant $\det \mathbf{g} = (\det \mathbf{D}\mathbf{F})^2$. The transformed weak form from (3.17) then reads

$$\int_{\Omega_0} \nabla \hat{u} \mathbf{g}^{-1} (\nabla \hat{v})^T |\det \mathbf{g}|^{1/2} d\xi = \int_{\Omega_0} \hat{f} \hat{v} |\det \mathbf{g}|^{1/2} d\xi \quad (4.13)$$

for test functions $\hat{v} = v \circ \mathbf{F}$. In terms of regularity and smoothness, the parametrization \mathbf{F} is here required to be of class \mathcal{C}^1 and to be injective almost everywhere, which means that singularities in sets of measure zero, such as points, are admitted.

Corresponding to the weak form (4.13), there is a strong form that makes use of the Laplace–Beltrami operator. Like the standard Laplacian, this operator is defined as the divergence of the gradient in parametric coordinates, and it reads

$$\Delta_{\xi} \hat{u} = |\det \mathbf{g}|^{-1/2} \sum_{k=1}^d \frac{\partial}{\partial \xi_k} \left(|\det \mathbf{g}|^{1/2} \nabla \hat{u} \mathbf{g}^{-1} \right). \quad (4.14)$$

Note that Δ_{ξ} is typically used to express PDEs on surfaces as in [21], but its definition holds for any kind of parametric coordinates.

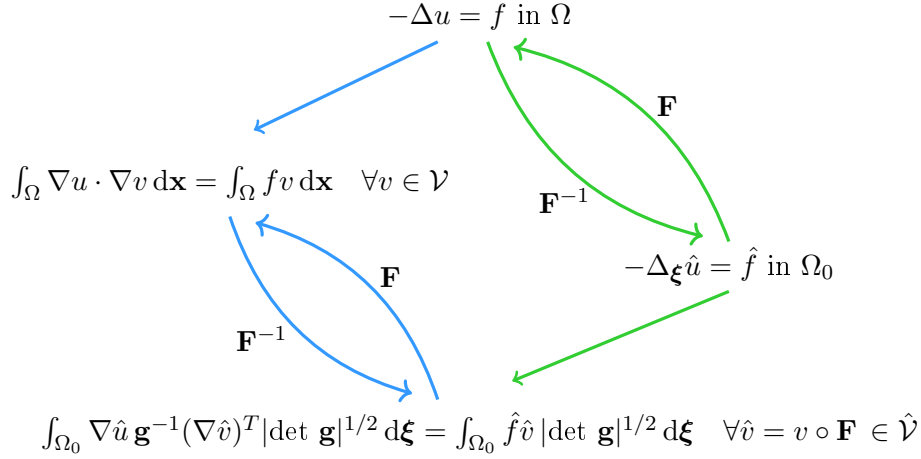


Figure 4.2. From the problem in the strong form in Cartesian coordinates (top corner), we derive the weak form in parametric coordinates (bottom corner) with two different approaches: in blue the route taken by standard IGA (approach (a)), in green the one by SB-IGA (approach (b)).

For the strong form of Poisson's equation with respect to the metric \mathbf{g} and expressed in the coordinates $\boldsymbol{\xi}$, this implies the representation

$$-\Delta_{\boldsymbol{\xi}} \hat{u} = \hat{f} \text{ in } \Omega_0, \quad (4.15a)$$

i.e.,

$$-\sum_{k=1}^d \frac{\partial}{\partial \xi_k} \left(|\det \mathbf{g}|^{1/2} \nabla \hat{u} \mathbf{g}^{-1} \right) = |\det \mathbf{g}|^{1/2} \hat{f} \text{ in } \Omega_0. \quad (4.15b)$$

Obviously, the Laplace–Beltrami operator takes into account twice-differentiable functions, so the parametrization \mathbf{F} now has to be of class \mathcal{C}^2 and injective almost everywhere, in order to hold in all Ω_0 .

Based on this general framework provided by differential geometry, there are two ways to derive the weak form (4.13) in parametric coordinates $\boldsymbol{\xi}$. We start with the strong form (3.12) in Cartesian coordinates \mathbf{x} , then we have the following choices.

- (a) First, we derive the weak form in \mathbf{x} (3.13) and then we apply the transformation to it, obtaining the weak form in $\boldsymbol{\xi}$ (4.13).
- (b) First, we apply the transformation to the strong form to get the strong form in parametric coordinates $\boldsymbol{\xi}$ (4.15). Then we proceed with the weak form (4.13).

The two approaches are summarized in Figure 4.2. Option (a) is the approach taken in the standard Galerkin-based IGA, while option (b) is the one taken by the scaled boundary IGA. In the latter, as already said, the weak form will not be considered directly in all independent variables, but it is split into two steps, with the first one along the angular direction and the second one in the scaling direction. From a theoretical point of view, both (a) and (b) lead to the same weak form in parametric coordinates. Moreover, we remark that IGA for Poisson's boundary value problem (3.12) can be interpreted as solving the transformed PDE (4.15) with the Laplace–Beltrami operator on the unit square or unit cube.

Also the discretization on the finite-dimensional space \mathcal{V}_h is done in different ways. In the standard IGA a Galerkin projection is applied to the weak form 4.13. While in

the SB-IGA we first consider a discretization of the weak form in η , that generates an ODE in ξ , and then we apply a second discretization to the weak form in ξ . Anyway both discretization approaches leads to a linear system, as seen in Section 3.1.1.

In the following, we analyze the two approaches in details. We will assemble the stiffness matrices of the linear systems and we will observe that the SB-parametrization leads to a stiffness matrix which is the tensor product of low-rank structures. Our purpose is to state a theorem about the equivalence of the two discretization approaches.

4.2.1 Galerkin-Based IGA

We consider Ω in the case $d = 2$ parametrized by the geometry function \mathbf{F} , as given in (4.4), and Jacobian \mathbf{DF} , as in (4.9). When writing the weak form from the Cartesian coordinates (x, y) to the parametric coordinates (ξ, η) , we need the inverse of the metric tensor \mathbf{g} defined in (4.12). We obtain

$$\begin{aligned} \mathbf{g}^{-1}(\xi, \eta) &= \mathbf{DF}^{-1}(\xi, \eta) \mathbf{DF}^{-T}(\xi, \eta) \\ &= \frac{1}{(\det \mathbf{DF})^2} \begin{pmatrix} \xi & 0 \\ 0 & 1 \end{pmatrix} \begin{pmatrix} \mathbf{b}_1^T(\eta) \\ \mathbf{b}_2^T(\eta) \end{pmatrix} \begin{pmatrix} \mathbf{b}_1(\eta) & | & \mathbf{b}_2(\eta) \end{pmatrix} \begin{pmatrix} \xi & 0 \\ 0 & 1 \end{pmatrix} \\ &= \frac{1}{J(\eta)^2} \begin{pmatrix} \mathbf{b}_1^T(\eta) \mathbf{b}_1(\eta) & \mathbf{b}_1^T(\eta) \mathbf{b}_2(\eta) / \xi \\ \mathbf{b}_2^T(\eta) \mathbf{b}_1(\eta) / \xi & \mathbf{b}_2^T(\eta) \mathbf{b}_2(\eta) / \xi^2 \end{pmatrix}, \end{aligned} \quad (4.16)$$

where

$$\mathbf{b}_1^T(\eta) := (\mathbf{C}_2 \mathbf{N}'(\eta), -\mathbf{C}_1 \mathbf{N}'(\eta)), \quad \mathbf{b}_2^T(\eta) := (-\mathbf{C}_2 \mathbf{N}(\eta) + x_{0,2}, \mathbf{C}_1 \mathbf{N}(\eta) - x_{0,1}). \quad (4.17)$$

Then inserting (4.16) into (4.13), the left-hand side becomes, omitting the arguments ξ, η for a compact notation,

$$\begin{aligned} \int_{\Omega_0} \nabla \hat{u} \mathbf{DF}^{-1} \mathbf{DF}^{-T} (\nabla \hat{v})^T | \det \mathbf{DF} | d\xi d\eta &= \\ &= \int_0^1 \int_0^1 \frac{1}{J} \left(\xi \hat{u}_\xi \hat{v}_\xi \mathbf{b}_1^T \mathbf{b}_1 + \hat{u}_\eta \hat{v}_\xi \mathbf{b}_2^T \mathbf{b}_1 + \hat{u}_\xi \hat{v}_\eta \mathbf{b}_1^T \mathbf{b}_2 + \frac{1}{\xi} \hat{u}_\eta \hat{v}_\eta \mathbf{b}_2^T \mathbf{b}_2 \right) d\xi d\eta, \end{aligned} \quad (4.18)$$

where $\cdot_\xi = \partial(\cdot)/\partial\xi$ and $\cdot_\eta = \partial(\cdot)/\partial\eta$.

Remark 4.1 (Singularity of the integral). *We notice that the integral*

$$\int_0^1 \int_0^1 \frac{1}{\xi} \hat{u}_\eta \hat{v}_\eta \mathbf{b}_2^T \mathbf{b}_2 d\xi d\eta \quad (4.19)$$

has a singularity for $\xi = 0$. However, the weak form (4.18) is equivalent to the left-hand side of the weak form in physical coordinates (3.13). Since $u, v \in H^1(\Omega)$, the integrals in the weak form (3.13) are well-defined and finite, hence also the integrals (4.18) and so (4.19) are finite.

For the numerical solution, a Galerkin projection on a finite-dimensional space is considered, i.e. (4.18) and the corresponding transformed right-hand side are evaluated by inserting approximations \hat{u}_h and \hat{v}_h , which are tensor product B-splines. To compute an entry in the stiffness matrix we consider

$$\hat{u}_h(\xi, \eta) = \sum_i \sum_j M_i(\xi) N_j(\eta) U_{i,j}, \quad \hat{v}_h(\xi, \eta) = M_k(\xi) N_\ell(\eta), \quad (4.20)$$

where we have omitted the degrees of the B-splines, and we insert (4.20) into (4.18). For the first integral, it follows

$$\begin{aligned} \int_0^1 \int_0^1 \frac{1}{J(\eta)} \xi \hat{u}_{h,\xi}(\xi, \eta) \hat{v}_{h,\xi}(\xi, \eta) \mathbf{b}_1^T(\eta) \mathbf{b}_1(\eta) d\xi d\eta = \\ = \sum_i \sum_j \left(\int_0^1 \xi M'_i(\xi) M'_k(\xi) d\xi \cdot \int_0^1 \frac{1}{J(\eta)} N_j(\eta) N_\ell(\eta) \mathbf{b}_1^T(\eta) \mathbf{b}_1(\eta) d\eta \right) U_{i,j}. \end{aligned} \quad (4.21)$$

Similarly, the three other integrals become:

$$\sum_i \sum_j \left(\int_0^1 M_i(\xi) M'_k(\xi) d\xi \cdot \int_0^1 \frac{1}{J(\eta)} N'_j(\eta) N_\ell(\eta) \mathbf{b}_2^T(\eta) \mathbf{b}_1(\eta) d\eta \right) U_{i,j}, \quad (4.22a)$$

$$\sum_i \sum_j \left(\int_0^1 M'_i(\xi) M_k(\xi) d\xi \cdot \int_0^1 \frac{1}{J(\eta)} N_j(\eta) N'_\ell(\eta) \mathbf{b}_1^T(\eta) \mathbf{b}_2(\eta) d\eta \right) U_{i,j}, \quad (4.22b)$$

$$\sum_i \sum_j \left(\int_0^1 \frac{1}{\xi} M_i(\xi) M_k(\xi) d\xi \cdot \int_0^1 \frac{1}{J(\eta)} N'_j(\eta) N'_\ell(\eta) \mathbf{b}_2^T(\eta) \mathbf{b}_2(\eta) d\eta \right) U_{i,j}. \quad (4.22c)$$

The two-dimensional integration can thus be carried out as the product of two one-dimensional integrations, which is a great computational advantage and an important consequence of the multiplicative structure of the Jacobian \mathbf{DF} .

For the right-hand side we obtain

$$\int_{\Omega_0} \hat{f} \hat{v}_h |\det \mathbf{DF}| d\xi d\eta = \int_0^1 \int_0^1 \xi M_k(\xi) N_\ell(\eta) J(\eta) \hat{f}(\xi, \eta) d\xi d\eta. \quad (4.23)$$

The separation of variables that we observe in (4.21)–(4.22) is a special case of the so-called low-rank tensor approximation that has been introduced by Mantzaflaris et al. [42, 41]. In this approach, low-rank approximations of the integral kernels are computed to provide a compact, separated representation of the integrals in IGA. In our case, there is no need to compute an approximation. Instead, the parametrization provides directly a low-rank tensor representation.

4.2.2 Scaled Boundary IGA

In the SB-IGA, we start considering the strong form of the problem in parametric coordinates (4.15) for the case $d = 2$. We insert (4.16) into (4.15) and we obtain

$$-\frac{\partial}{\partial \xi} \left(\frac{1}{J} (\xi \mathbf{b}_1^T \mathbf{b}_1 \hat{u}_\xi + \mathbf{b}_2^T \mathbf{b}_1 \hat{u}_\eta) \right) - \frac{\partial}{\partial \eta} \left(\frac{1}{J} \left(\mathbf{b}_1^T \mathbf{b}_2 \hat{u}_\xi + \frac{1}{\xi} \mathbf{b}_2^T \mathbf{b}_2 \hat{u}_\eta \right) \right) = \xi J \hat{f}. \quad (4.24)$$

Then, the weak form is considered only in the circumferential direction η , that is a Galerkin projection with respect to the circumferential coordinate η is derived, using the given representation of the boundary curve in terms of the B-splines $\mathbf{N}(\eta)$. We set

$$\hat{u}(\xi, \eta) = \mathbf{N}^T(\eta) \mathbf{U}(\xi), \quad \hat{v}(\xi, \eta) = \mathbf{N}^T(\eta) \mathbf{V}, \quad (4.25)$$

where $\mathbf{U}(\xi) \in \mathbb{R}^n$ is the solution depending on the radial parameter ξ and the variations $\mathbf{V} \in \mathbb{R}^n$ are arbitrarily chosen with the periodic constraint $V_1 = V_n$. We remind that the quantities J , \mathbf{b}_1 and \mathbf{b}_2 depend only on η and not on ξ . We insert \hat{u} in (4.24),

we multiply by \hat{v} and integrate with respect to η . This yields, omitting the arguments ξ, η for a compact notation,

$$\begin{aligned} & - \int_0^1 \mathbf{V}^T \mathbf{N} \frac{1}{J} \mathbf{b}_1^T \mathbf{b}_1 \mathbf{N}^T \mathbf{U}_\xi \, d\eta - \int_0^1 \mathbf{V}^T \mathbf{N} \frac{1}{J} \xi \mathbf{b}_1^T \mathbf{b}_1 \mathbf{N}^T \mathbf{U}_{\xi\xi} \, d\eta \\ & - \int_0^1 \mathbf{V}^T \mathbf{N} \frac{1}{J} \mathbf{b}_2^T \mathbf{b}_1 \mathbf{N}^T \mathbf{U}_\xi \, d\eta - \int_0^1 \mathbf{V}^T \mathbf{N} \frac{\partial}{\partial \eta} \left(\frac{1}{J} \left(\mathbf{b}_1^T \mathbf{b}_2 \hat{u}_\xi + \frac{1}{\xi} \mathbf{b}_2^T \mathbf{b}_2 \hat{u}_\eta \right) \right) d\eta \quad (4.26) \\ & = \int_0^1 \mathbf{V}^T \mathbf{N} \xi J \hat{f} \, d\eta. \end{aligned}$$

The fourth integral of equation (4.26) is integrated by parts, using the property $V_1 = V_n$ for the variations of a periodic curve. This results in

$$\begin{aligned} & - \int_0^1 \mathbf{V}^T \mathbf{N} \frac{\partial}{\partial \eta} \left(\frac{1}{J} \left(\mathbf{b}_1^T \mathbf{b}_2 \hat{u}_\xi + \frac{1}{\xi} \mathbf{b}_2^T \mathbf{b}_2 \hat{u}_\eta \right) \right) d\eta \\ & = \int_0^1 \mathbf{V}^T \mathbf{N}' \frac{1}{J} \mathbf{b}_1^T \mathbf{b}_2 \mathbf{N}^T \mathbf{U}_\xi \, d\eta + \int_0^1 \mathbf{V}^T \mathbf{N}' \frac{1}{J} \frac{1}{\xi} \mathbf{b}_2^T \mathbf{b}_2 \mathbf{N}^T \mathbf{U} \, d\eta. \end{aligned} \quad (4.27)$$

Since (4.26) must hold for all variations \mathbf{V} , we generate a strong form for the vector $\mathbf{U}(\xi)$. Moreover we perform the integration with respect to η obtaining a system of ordinary differential equations (ODEs) for $\mathbf{U}(\xi)$. For this purpose, we introduce a notation that is common in the SB-FEM and SB-IGA. We define

$$\begin{aligned} \mathbf{E} &:= \int_0^1 \frac{1}{J(\eta)} \mathbf{N}(\eta) \mathbf{b}_1^T \mathbf{b}_1 \mathbf{N}^T(\eta) \, d\eta, \quad \mathbf{G} := \int_0^1 \frac{1}{J(\eta)} \mathbf{N}'(\eta) \mathbf{b}_1^T(\eta) \mathbf{b}_2(\eta) \mathbf{N}^T(\eta) \, d\eta, \\ \mathbf{K} &:= \int_0^1 \frac{1}{J(\eta)} \mathbf{N}'(\eta) \mathbf{b}_2^T \mathbf{b}_2 \mathbf{N}^T(\eta) \, d\eta, \quad \mathbf{S}(\xi) := - \int_0^1 \mathbf{N}(\eta) J(\eta) \hat{f}(\xi, \eta) \, d\eta. \end{aligned} \quad (4.28)$$

Then (4.26) becomes

$$\xi \mathbf{E} \mathbf{U}_{\xi\xi} + (\mathbf{E} - \mathbf{G} + \mathbf{G}^T) \mathbf{U}_\xi - \frac{1}{\xi} \mathbf{K} \mathbf{U} = \xi \mathbf{S}(\xi). \quad (4.29)$$

This way we obtain a system of ODEs in the scaling direction ξ , with boundary conditions $\mathbf{U}(\xi = 1) = \mathbf{0}$ and periodicity condition $U_1(\xi) = U_n(\xi)$. Moreover, in the scaling center we have the conditions

$$U_1(\xi = 0) = U_2(\xi = 0) = \dots = U_n(\xi = 0), \quad (4.30)$$

i.e., the solution is the same in all components.

There are several options for the numerical treatment of the system of ODEs (4.29) in the scaling direction, as proposed in [14, 15, 43]. Besides an analytical approach that is based on the solution of an eigenvalue problem with a Hamiltonian matrix, see Section 4.3 below, there is also the possibility of using collocation or standard Galerkin projection with respect to the ξ -variable. The latter is based on a weak form in ξ , which possesses the same structure and the same separation property as shown in (4.21)–(4.22). To this end, we multiply (4.29) by a vector of test functions

$$\mathbf{W}(\xi) \in \mathbb{R}^n, \quad (4.31)$$

where $\mathbf{W}(\xi = 1) = \mathbf{0}$ and we integrate it with respect to ξ . This gives

$$\begin{aligned} & \int_0^1 \xi \mathbf{W}^T \mathbf{E} \mathbf{U}_{\xi\xi} \, d\xi + \int_0^1 \mathbf{W}^T (\mathbf{E} - \mathbf{G} + \mathbf{G}^T) \mathbf{U}_\xi \, d\xi \\ & - \int_0^1 \frac{1}{\xi} \mathbf{W}^T \mathbf{K} \mathbf{U} \, d\xi = \int_0^1 \xi \mathbf{W}^T \mathbf{S}(\xi) \, d\xi. \end{aligned} \quad (4.32)$$

From integration by parts we obtain

$$\int_0^1 \xi \mathbf{W}^T \mathbf{E} \mathbf{U}_{\xi\xi} d\xi = - \int_0^1 (\xi \mathbf{W}_\xi^T + \mathbf{W}^T) \mathbf{E} \mathbf{U}_\xi d\xi + \xi \mathbf{W}^T \mathbf{E} \mathbf{U}_\xi|_0^1,$$

where the last term vanishes due to the boundary conditions. Furthermore,

$$\int_0^1 \mathbf{W}^T \mathbf{G}^T \mathbf{U}_\xi d\xi = - \int_0^1 \mathbf{W}_\xi^T \mathbf{G}^T \mathbf{U} d\xi + \mathbf{W}^T \mathbf{G}^T \mathbf{U}|_0^1$$

holds. Here, the last term vanishes due to the boundary conditions for $\xi = 1$ and due to the property (4.30) for $\xi = 0$, considering that, for $\mathbf{U}(0) = (1, 1, \dots, 1)^T \alpha$ with some $\alpha \in \mathbb{R}$, the differentiation of the partition of unity $\mathbf{N}(\eta)^T (1, 1, \dots, 1)^T = 1$ yields

$$\mathbf{G}^T \mathbf{U}(0) = \int_0^1 \frac{1}{J(\eta)} \mathbf{N}(\eta) \mathbf{b}_2^T(\eta) \mathbf{b}_1(\eta) \underbrace{\mathbf{N}'(\eta)^T \begin{pmatrix} 1 \\ \vdots \\ 1 \end{pmatrix}}_{=0} \alpha d\eta = \mathbf{0}.$$

Overall, the weak form of (4.29) thus can be written as

$$\begin{aligned} \int_0^1 \xi \mathbf{W}_\xi^T \mathbf{E} \mathbf{U}_\xi d\xi + \int_0^1 \mathbf{W}_\xi^T \mathbf{G}^T \mathbf{U} d\xi + \int_0^1 \mathbf{W}^T \mathbf{G} \mathbf{U}_\xi d\xi \\ + \int_0^1 \frac{1}{\xi} \mathbf{W}^T \mathbf{K} \mathbf{U} d\xi = - \int_0^1 \xi \mathbf{W}^T \mathbf{S}(\xi) d\xi. \end{aligned} \quad (4.33)$$

For the Galerkin projection, we insert approximations

$$\mathbf{U}_h(\xi) = \sum_{i=1}^m M_i(\xi) \begin{pmatrix} U_{i,1} \\ \vdots \\ U_{i,n} \end{pmatrix} \quad \text{and} \quad \mathbf{W}_h(\xi) = \mathbf{e}_\ell M_k(\xi), \quad k = 1, \dots, m, \quad (4.34)$$

where \mathbf{e}_ℓ , $\ell = 1, \dots, n$, stands for the standard basis in \mathbb{R}^n .

We can now compute an entry of the stiffness matrix of the linear system. This computation will be done in the following section, where we state an equivalence theorem between the two approaches.

4.2.3 Equivalence Theorem

Thanks to the derivation shown in Section 4.2.1 and 4.2.2, we now state a theorem about the equivalence of the scaled boundary isogeometric analysis and the standard Galerkin-based IGA, when a scaled boundary parametrization of the domain is available. This equivalence is valid for a linear problem and it is proved on Poisson's boundary value problem. In a more general nonlinear problem setting, however, the two approaches might differ since the diagram in Figure 4.2 might not commute. An important implication of this theorem is immediately clear: the standard convergence results of [6] hold also for the SB-IGA if combined with a Galerkin projection in radial direction. Moreover, in a specific implementation, the degrees of freedom used in both approaches are identical up to a permutation.

Theorem 4.2 (Equivalence theorem). *Let $\Omega \in \mathbb{R}^2$ be a star-shaped domain where only its boundary curve is available, $\gamma(\eta) = \sum_{j=1}^n N_j(\eta) \mathbf{c}_j$. Consider a scaled boundary parametrization for this domain such that the geometry function $\mathbf{F} : \Omega_0 = [0, 1]^2 \rightarrow \Omega$ is defined as in (4.5), and a linear problem, w.l.o.g. Poisson's boundary value problem*

in (3.12). Consider the weak form, induced by the scaled boundary representation, generated in the standard isogeometric analysis (left-hand side in Equation (4.18) and right-hand side in Equation (4.23)), and apply a Galerkin projection with the numerical approximation

$$\hat{u}_h(\xi, \eta) = \sum_{i=1}^m \sum_{j=1}^n M_i(\xi) N_j(\eta) U_{i,j}. \quad (4.35)$$

Then, the resulting discretized system is equivalent to the discretization of the weak form generated in the scaled boundary isogeometric analysis (Equation (4.33)) by means of the Galerkin projection in (4.34).

Proof. We insert the discretization $\mathbf{U}_h(\xi)$ and $\mathbf{W}_h(\xi)$ (4.34) into the weak form (4.33). For the first integral we obtain:

$$\begin{aligned} \int_0^1 \xi \mathbf{W}_\xi^T \mathbf{E} \mathbf{U}_\xi \, d\xi &\approx \int_0^1 \xi \mathbf{e}_\ell^T M'_k(\xi) \mathbf{E} \sum_{i=1}^m M'_i(\xi) (U_{i,1}, \dots, U_{i,n})^T \, d\xi = \\ &= \sum_{i=1}^m \sum_{j=1}^n \left(\int_0^1 \xi M'_k(\xi) M'_i(\xi) \, d\xi \int_0^1 \frac{1}{J(\eta)} N_\ell(\eta) N_j(\eta) \mathbf{b}_1^T(\eta) \mathbf{b}_1(\eta) \, d\eta \right) U_{i,j}. \end{aligned} \quad (4.36a)$$

Similarly, the other three integrals become:

$$\begin{aligned} \int_0^1 \mathbf{W}_\xi^T \mathbf{G}^T \mathbf{U} \, d\xi &\approx \int_0^1 \mathbf{e}_\ell^T M'_k(\xi) \mathbf{G}^T \sum_{i=1}^m M_i(\xi) (U_{i,1}, \dots, U_{i,n})^T \, d\xi = \\ &= \sum_{i=1}^m \sum_{j=1}^n \left(\int_0^1 M'_k(\xi) M_i(\xi) \, d\xi \int_0^1 \frac{1}{J(\eta)} N_\ell(\eta) N'_j(\eta) \mathbf{b}_2^T(\eta) \mathbf{b}_1(\eta) \, d\eta \right) U_{i,j}, \end{aligned} \quad (4.36b)$$

$$\begin{aligned} \int_0^1 \mathbf{W}^T \mathbf{G} \mathbf{U}_\xi \, d\xi &\approx \int_0^1 \mathbf{e}_\ell^T M_k(\xi) \mathbf{G} \sum_{i=1}^m M'_i(\xi) (U_{i,1}, \dots, U_{i,n})^T \, d\xi = \\ &= \sum_{i=1}^m \sum_{j=1}^n \left(\int_0^1 M_k(\xi) M'_i(\xi) \, d\xi \int_0^1 \frac{1}{J(\eta)} N'_\ell(\eta) N_j(\eta) \mathbf{b}_1^T(\eta) \mathbf{b}_2(\eta) \, d\eta \right) U_{i,j}, \end{aligned} \quad (4.36c)$$

$$\begin{aligned} \int_0^1 \frac{1}{\xi} \mathbf{W}^T \mathbf{K} \mathbf{U} \, d\xi &\approx \int_0^1 \frac{1}{\xi} \mathbf{e}_\ell^T M_k(\xi) \mathbf{K} \sum_{i=1}^m M_i(\xi) (U_{i,1}, \dots, U_{i,n})^T \, d\xi = \\ &= \sum_{i=1}^m \sum_{j=1}^n \left(\int_0^1 \frac{1}{\xi} M_k(\xi) M_i(\xi) \, d\xi \int_0^1 \frac{1}{J(\eta)} N'_\ell(\eta) N'_j(\eta) \mathbf{b}_2^T(\eta) \mathbf{b}_2(\eta) \, d\eta \right) U_{i,j}. \end{aligned} \quad (4.36d)$$

We observe that the contribution to the stiffness matrix that corresponds to the unknown $U_{i,j}$ is exactly the same as in (4.21)–(4.22).

The source term in (4.33) is evaluated via

$$\begin{aligned} - \int_0^1 \xi \mathbf{W}^T \mathbf{S}(\xi) \, d\xi &\approx - \int_0^1 \xi \mathbf{e}_\ell^T M_k(\xi) \left(- \int_0^1 \mathbf{N}(\eta) J(\eta) \hat{f}(\xi, \eta) \, d\eta \right) \, d\xi = \\ &= \int_0^1 \int_0^1 \xi M_k(\xi) N_\ell(\eta) J(\eta) \hat{f}(\xi, \eta) \, d\eta \, d\xi, \end{aligned} \quad (4.36e)$$

which is again identical to the classical IGA discretization of the right-hand side (Equation (4.23)). \square

4.3 The Singularity in the Scaling Center

In this section we investigate the singularity of the parametrization in the scaling center in the case $d = 2$. It must be underlined that we do not notice a singularity in the solution of Poisson's equation. Indeed, such an elliptic boundary value problem exhibits a regular behavior, with the maximum principle bounding the solution of the strong form. Coercivity and continuity of the bilinear form in the weak formulation, on the other hand, yield bounds and stability estimates in the energy and H^1 -norms. To better understand the singularity at $\xi = 0$, we consider the boundary value problem generated by the SB-IGA. In its original form, the scaled boundary finite element method, which provides the basic idea for the SB-IGA, is a semi-analytical method where the boundary value problem with respect to ξ is solved exactly [54]. We adopt here this approach since it offers insights into the nature of the singularity. For a more general treatment of singularities in IGA see [59, 60].

We start considering the system of ODEs in the scaling direction (4.29) as homogeneous system (writing $\mathbf{U}_\xi = \mathbf{U}'$)

$$\xi^2 \mathbf{E} \mathbf{U}'' + \xi (\mathbf{E} - \mathbf{G} + \mathbf{G}^T) \mathbf{U}' - \mathbf{K} \mathbf{U} = \mathbf{0}, \quad (4.37)$$

with a symmetric positive definite matrix $\mathbf{E} \in \mathbb{R}^{n \times n}$, a symmetric positive semi-definite matrix $\mathbf{K} \in \mathbb{R}^{n \times n}$, and a matrix $\mathbf{G} \in \mathbb{R}^{n \times n}$. Next, we introduce the new variables

$$\mathbf{y}(\xi) := \begin{pmatrix} \mathbf{U}(\xi) \\ \mathbf{Z}(\xi) \end{pmatrix} \quad \text{where } \mathbf{Z} := \xi \mathbf{E} \mathbf{U}' + \mathbf{G}^T \mathbf{U}. \quad (4.38)$$

The second order system of ODEs is thus transformed to a first order system

$$\xi \mathbf{y}' = -\mathbf{H} \mathbf{y}, \quad (4.39)$$

with the matrix

$$\mathbf{H} := \begin{pmatrix} \mathbf{E}^{-1} \mathbf{G}^T & -\mathbf{E}^{-1} \\ -\mathbf{K} + \mathbf{G} \mathbf{E}^{-1} \mathbf{G}^T & -\mathbf{G} \mathbf{E}^{-1} \end{pmatrix}. \quad (4.40)$$

$\mathbf{H} \in \mathbb{R}^{2n \times 2n}$ is a Hamiltonian matrix, i.e., it becomes a symmetric matrix when multiplied by the skew-symmetric matrix \mathbf{J} ,

$$\mathbf{J} = \begin{pmatrix} \mathbf{0} & \mathbf{I}_n \\ -\mathbf{I}_n & \mathbf{0} \end{pmatrix} \Rightarrow (\mathbf{J} \mathbf{H})^T = \mathbf{J} \mathbf{H}, \quad (4.41)$$

where \mathbf{I}_n is the n -by- n identity matrix.

The characteristic polynomial $d(\lambda) = \det(\lambda \mathbf{I}_{2n} - \mathbf{H})$ is an even function, which means that the eigenvalues of \mathbf{H} are such that $\lambda_{n+i} = -\lambda_i$, $i = 1, \dots, n$, with $\text{Re} \lambda_i \geq 0$, and the corresponding eigenvectors are Φ_i . Hence the solution of (4.39) in the homogeneous case is a linear combination of terms $c_i \xi^{\lambda_i} \Phi_i + c_{n+i} \xi^{-\lambda_i} \Phi_{n+i}$. Since the solution is finite in $\xi = 0$, one concludes that $c_{n+i} = 0$, $i = 1, \dots, n$, which cancels the unstable part.

In practice, the numerical solution of the eigenvalue problem for \mathbf{H} is only feasible for relatively small dimensions. But our interest here lies on the insight that we obtain from it. The singularity in the scaling center thus loses its threat. However, the question remains what happens if we apply a discretization with respect to ξ and do not utilize the eigenvalue solution.

We concentrate next on the Galerkin-based IGA and we discuss the practical treatment of the singularity in the scaling center. We have already seen that analytically, see Remark 4.1, and with the just shown semi-discretization approach, there is no

singularity in the treatment of the integrals. Also in the numerical experiments that we performed so far, we did not observe instabilities nor singular stiffness matrices. A possible explanation can be given in the following way.

Consider the bilinear form (4.18) in parametric coordinates. The fourth term in the integral is the critical one and it contains the factor $1/\xi$. With the separation of integrals seen in (4.21)–(4.22), this term is written as the product of a well-defined integral with respect to η times the integral

$$\int_0^1 \frac{1}{\xi} M_i(\xi) M_k(\xi) d\xi. \quad (4.42)$$

We use linear B-splines and analyze the contribution of the first element integrated from 0 to h , where h is the mesh size. The integral (4.42) then yields for $M_i = M_k = M_{1,1}(\xi) = 1 - \xi$

$$\int_0^h \frac{1}{\xi} (1 - \xi/h)(1 - \xi/h) d\xi = \int_0^h \left(\frac{1}{\xi} - \frac{2}{h} + \frac{\xi}{h^2} \right) d\xi.$$

Obviously, the problematic integral is the one containing $1/\xi$, while the other terms are not critical. In a numerical implementation a quadrature rule is applied in order to approximate numerically the integral, so it is used instead of exact integration. If for example we apply the midpoint rule, we get

$$\int_0^h \left(\frac{1}{\xi} - \frac{2}{h} + \frac{\xi}{h^2} \right) d\xi \doteq h \left(\frac{1}{\xi} - \frac{2}{h} + \frac{\xi}{h^2} \right) \Big|_{\xi=h/2} = \frac{1}{2}. \quad (4.43)$$

The evaluation is thus independent of h , and the contribution of this integral to the stiffness matrix is always well-defined.

The above reasoning applies also to B-splines of higher degrees and to higher order quadrature rules, as long as the nodes of the quadrature rule are in the interior of the interval. Indeed, if we take quadrature points $\{q_r\}_{r=1,\dots,R}$ and quadrature weights $\{w_r\}_{r=1,\dots,R}$ on the interval $[0, 1]$, the quadrature rule reads

$$\int_0^h \frac{1}{\xi} M_i(\xi) M_k(\xi) d\xi \doteq h \sum_{r=1}^R \frac{w_r}{h q_r} M_i(h q_r) M_k(h q_r). \quad (4.44)$$

Using the fact that the B-splines are bounded by 1, we can state that

$$\left| \int_0^h \frac{1}{\xi} M_i(\xi) M_k(\xi) d\xi \right| \leq \sum_{r=1}^R \frac{|w_r|}{q_r} < \infty, \quad (4.45)$$

if the points are chosen in the interior of the interval, i.e., $q_r > 0 \forall r$. In this way, we can conclude that the computation itself of the stiffness matrix in Galerkin-based IGA is not affected by the singularity.

When using Galerkin-based IGA in combination with an SB-parametrization, the property (4.30) in the scaling center is not enforced and holds only approximately as the discretization converges. In this context it turns out that enforcing (4.30) via $n - 1$ additional constraints $U_{1,j} = U_{1,1}$ for $j = 2, \dots, n$, for the unknowns (4.35) is beneficial and can be implemented in the same fashion as a Dirichlet boundary condition or a periodicity condition. The constraints imply that

$$\hat{u}_h(0, \eta) = \sum_{i=1}^m \sum_{j=1}^n M_i(0) N_j(\eta) U_{i,j} = \sum_{i=1}^m \sum_{j=1}^n M_i(0) N_j(\eta) U_{1,1} = U_{1,1}. \quad (4.46)$$

Moreover, $M_1(\xi) \sum_{j=1}^n N_j(\eta) = M_1(\xi)$ is the basis function around the scaling center that is then actually used in the Galerkin projection. The same approach, but with a different justification, can be found in [26, 59], where it is shown that, in this way, the finite-dimensional subspace used in the Galerkin projection is still in $H^1(\Omega)$, in opposition to the approach without enforcing (4.30).

In the next section we validate the previous theoretical results with some examples. In particular, we will notice that even if the Jacobian of the stiffness matrix has a singularity, we do not observe any problem in the computation of the integrals, thanks to the quadrature rule. Furthermore, having demonstrated that the SB-IGA is equivalent to the standard Galerkin-based IGA with an SB-parametrization, the SB-IGA inherits the properties of stability and convergence of the standard IGA. For instance, we observe the same convergence rate.

It will be also shown that for some geometries, an SB-parametrization is much easier to construct, since the construction of rays going from the scaling center to the boundary curve is more natural than the mesh grids used for the standard parametrization. However, the condition number might grow faster.

4.4 Examples

We now solve Poisson's equation with zero Dirichlet boundary conditions on different geometries using the scaled boundary isogeometric analysis. We will consider also the same geometries as in Section 3.3, but only the boundary curve will be the same, the mesh inside the domain will be generated starting from a scaling center and connecting it to the control points on the boundary. For our simulations we used an extension of the ISOGAT package [63], with the precaution to add a set of periodic conditions together with the Dirichlet boundary conditions. Indeed, the geometry function \mathbf{F} (see Figure 4.1) maps the left edge of Ω_0 into the scaling center, the lower and upper edges into the same ray in the physical domain Ω and the right edge into $\partial\Omega$. That is, the control point of the scaling center is repeated multiple times and so the numerical solution computed there should coincide. At the same time the control points that run along the center and the ones associated to the lower and upper edges should coincide, as well as the numerical solution computed there. This implies the imposition of periodic boundary conditions on the left, on the top, and on the bottom edges of the parameter domain. At last the Dirichlet boundary conditions are considered along $\partial\Omega$ and so in the numerical solutions computed in the control points associated to the right edge.

In this section we will also investigate the influence of the choice of the scaling center on the numerical results. To do so we compute and compare the energy norm $\|u_h\|_E$, the L^2 -error norm $\|u - u_h\|$ and the condition number of the stiffness matrix with respect to the mesh size $h = (\#\text{DoF})^{-1/2}$. All the geometries that we consider in our examples are star-shaped, since this property is required in order to construct an SB-parametrization as presented in Section 4.1.

4.4.1 Unit Disk

A disk suggests itself as a very suitable geometry for testing the scaled boundary approach. Indeed, it is a star-shaped domain whose kernel coincides with the domain itself, where we call kernel the set of all points from which the entire boundary is visible.

Our physical domain Ω will be the disk with radius 1 and center $(0,0)$. As seen in

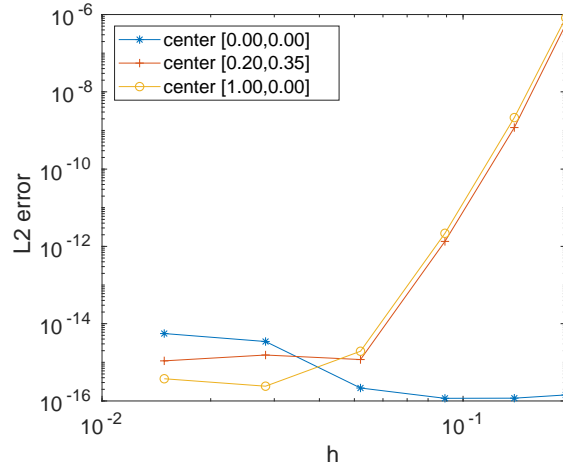


Figure 4.3. L^2 -error norm for three different SB-parametrizations of the unit disk when the right-hand side function $f = 1$

Section 4.1, only the boundary curve of the domain is available and it is fixed by certain degree, knot vector, weights and control points. In our case the boundary of the unit disk is a NURBS curve with degree $q = 2$, knot vector

$$H = \{0, 0, 0, 0.25, 0.25, 0.5, 0.5, 0.75, 0.75, 1, 1, 1\},$$

weights $\omega = \{1, \sqrt{2}/2, 1, \sqrt{2}/2, 1, \sqrt{2}/2, 1, \sqrt{2}/2, 1\}$ and control points

$$\{\mathbf{c}_j\}_{j=1,\dots,9} = \{(1, 0), (1, 1), (0, 1), (-1, 1), (-1, 0), (-1, -1), (0, -1), (1, -1), (1, 0)\}.$$

To construct the SB-parametrization we start picking a scaling center x_0 and then we connect it with the boundary $\partial\Omega$, that is the circumference of the disk. We start with the problem

$$\begin{cases} -\Delta u &= 1 & \text{in } \Omega, \\ u &= 0 & \text{on } \partial\Omega, \end{cases}$$

whose solution on the unit disk and center in $(0, 0)$ is

$$u(x, y) = \frac{1 - x^2 - y^2}{4}.$$

The first and obvious choice for the scaling center would be the center of the disk, and so $x_0 = (0, 0)$. In this case the numerical solution is already exact at the first iteration, since the analytical solution is contained in the space generated by the basis functions of this mesh. When moving the scaling center, the numerical solution needs couple of refinements to get an error of the size of the machine precision. In Figure 4.3 we have plotted the L^2 -error norm for several refinement steps versus the mesh size h . Three different scaling centers have been considered: the centroid of the disk, a random point inside the disk and a point on the boundary. In Figure 4.4 the condition number of the stiffness matrix arising from the three different SB-parametrizations has been plotted for several refinement steps. We can see that, when the scaling center lies on the boundary, the condition number is the highest and its growth rate is of order $1/h^4$. Inside the domain, the condition number is slightly smaller when the scaling center is the centroid, but, in both cases, it grows with rate $1/h^3$. Even though this example gives already an insight on which choice for the scaling center could be beneficial, we change the right-hand side of the problem, in order to get more information also on the behavior of the L^2 -error and energy norms.

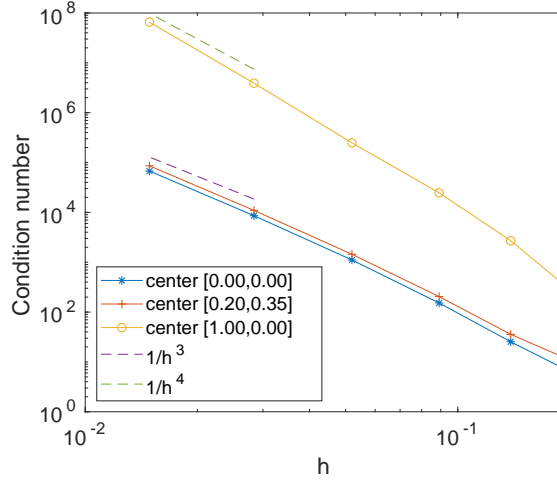


Figure 4.4. Condition number of the stiffness matrix for three different SB-parametrizations of the unit disk when the right-hand side function $f = 1$. When the scaling center is on the boundary of the disk the condition number is higher and grows as $1/h^4$, instead of $1/h^3$ as in the other cases.

We now consider as right-hand side of the problem

$$f = 3\pi \left(2 \sin \left(\frac{3}{2}\pi R \right) + 3\pi R \cos \left(\frac{3}{2}\pi R \right) \right), \quad \text{with } R = x^2 + y^2,$$

then the analytical solution is

$$u(x, y) = \cos \left(\frac{3}{2}\pi R \right).$$

Then we pick a point x_0 inside the kernel of Ω . We construct for this example five different SB-parametrizations based on five different scaling centers depicted in Figure 4.5:

- (D.1) the centroid of the disk $(0, 0)$,
- (D.2) a point inside the domain preserving an axial symmetry $(0.6, 0)$,
- (D.3) a random point inside the domain $(-0.6, -0.4)$,
- (D.4) a random point on the boundary $(-0.35, 0.94)$,
- (D.5) a control point lying on the boundary $(0, -1)$.

In the scaling direction we consider B-splines of degree $p = 2$, so that we have the same degrees in both directions, as done in the numerical examples for the standard Galerkin IGA (Section 3.3). The knot vector in the scaling direction is then $\Xi = \{0, 0, 0, 1, 1, 1\}$ and the control points on one ray contains a control point of the boundary, the scaling center and one inner control point computed with a degree elevation refinement. The SB-parametrization is then the tensor product of the NURBS boundary curve with the B-splines in the scaling direction, as seen in Equation (4.5). Here the control points are ordered such that the scaling center is repeated 9 times. We report now the control points only for two of our five cases, the other ones can be easily generated in the same way. In Figure 4.6 the control point grid and the physical domain with the image of the knot lines for these two cases have been plotted.

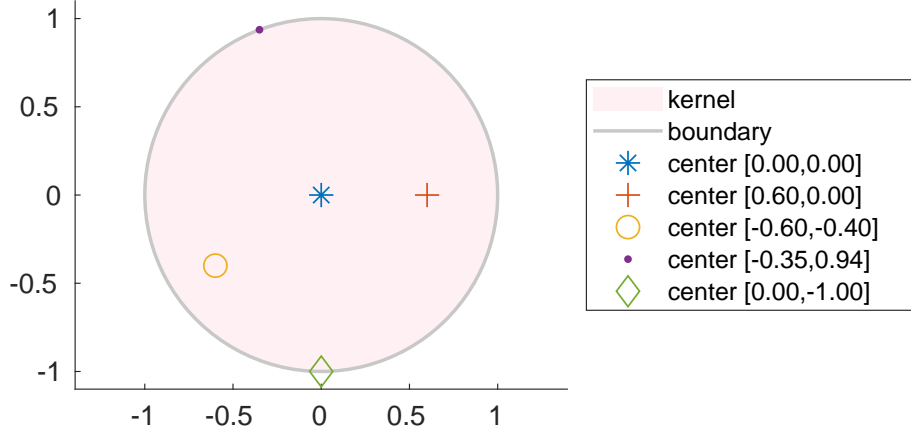


Figure 4.5. Five different points chosen as scaling center for the unit disk. The pink area represents the kernel of the domain, that for this geometry coincides with the domain itself.

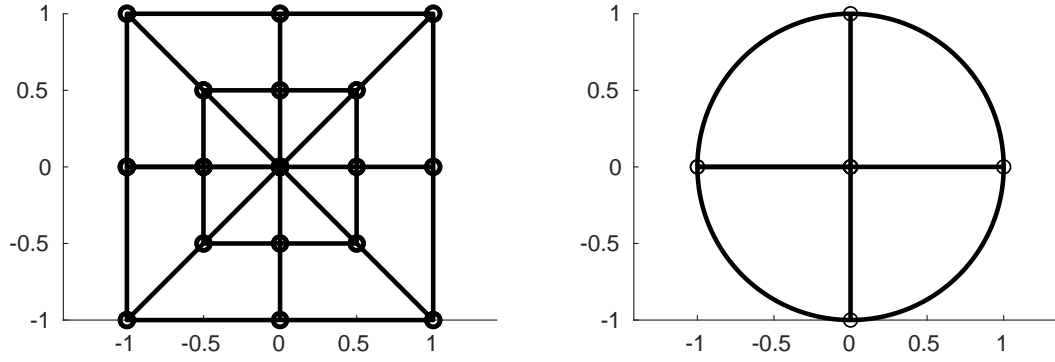
$$(D.1) \quad \{\bar{\mathbf{a}}_{i,j}\}_{i=1,\dots,3,j=1,\dots,9} =$$

$$\begin{aligned} & \{(0.0, 0.0) \quad (0.0, 0.0) \quad (0.0, 0.0) \quad (0.0, 0.0) \quad (0.0, 0.0) \\ & \quad (0.0, 0.0) \quad (0.0, 0.0) \quad (0.0, 0.0) \quad (0.0, 0.0); \\ & \quad (-0.5, 0.0) \quad (-0.5, -0.5) \quad (0.0, -0.5) \quad (0.5, -0.5) \quad (0.5, 0.0) \\ & \quad (0.5, 0.5) \quad (0.0, 0.5) \quad (-0.5, 0.5) \quad (-0.5, 0.0); \\ & \quad (-1.0, 0.0) \quad (-1.0, -1.0) \quad (0.0, -1.0) \quad (1.0, -1.0) \quad (1.0, 0.0) \\ & \quad (1.0, 1.0) \quad (0.0, 1.0) \quad (-1.0, 1.0) \quad (-1.0, 0.0)\}. \end{aligned}$$

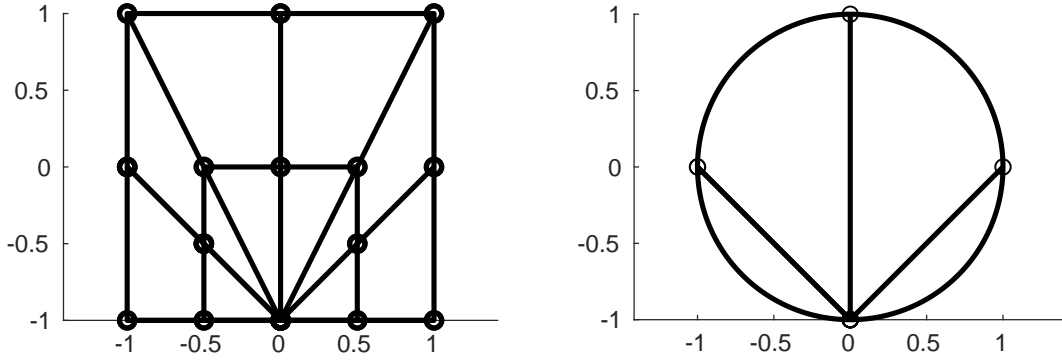
$$(D.5) \quad \{\bar{\mathbf{a}}_{i,j}\}_{i=1,\dots,3,j=1,\dots,9} =$$

$$\begin{aligned} & \{(0.0, -1.0) \quad (0.0, -1.0) \quad (0.0, -1.0) \quad (0.0, -1.0) \quad (0.0, -1.0) \\ & \quad (0.0, -1.0) \quad (0.0, -1.0) \quad (0.0, -1.0) \quad (0.0, -1.0); \\ & \quad (-0.5, -0.5) \quad (-0.5, -1.0) \quad (0.0, -1.0) \quad (0.5, -1.0) \quad (0.5, -0.5) \\ & \quad (0.5, 0.0) \quad (0.0, 0.0) \quad (-0.5, 0.0) \quad (-0.5, -0.5); \\ & \quad (-1.0, 0.0) \quad (-1.0, -1.0) \quad (0.0, -1.0) \quad (1.0, -1.0) \quad (1.0, 0.0) \\ & \quad (1.0, 1.0) \quad (0.0, 1.0) \quad (-1.0, 1.0) \quad (-1.0, 0.0)\}. \end{aligned}$$

To compare the different parametrizations we analyze, for several refinement steps, the energy norm, the L^2 -error norm and the condition number of the stiffness matrix, as done in Section 3.3 for the standard IGA examples. In Figure 4.7 we have plotted all these quantities for several refinement steps. Regarding the energy norm, all numerical solutions tend from below to the same maximum value, as expected. Moreover this value coincides with the one obtained when we solved this equation on the disk with the standard Galerkin IGA (Figure 3.14(a)). The parametrization of the case (D.1) presents a faster convergence with respect to the others, but after three refinements they have all reached the same reference value. The same happens when we look at the L^2 -error norm. The parametrization (D.1), i.e., when the scaling center is the centroid, presents always the smallest error. Then the parametrizations (D.2) and (D.3), i.e., when the scaling center is a random point inside the disk, follow. While the cases



(a) Case (D.1): the scaling center is the centroid of the disk.



(b) Case (D.5): the scaling center is a control point on the boundary.

Figure 4.6. Geometry description of the unit disk using an SB-parametrization: control point grid (left), physical domain with image of knot lines (right)

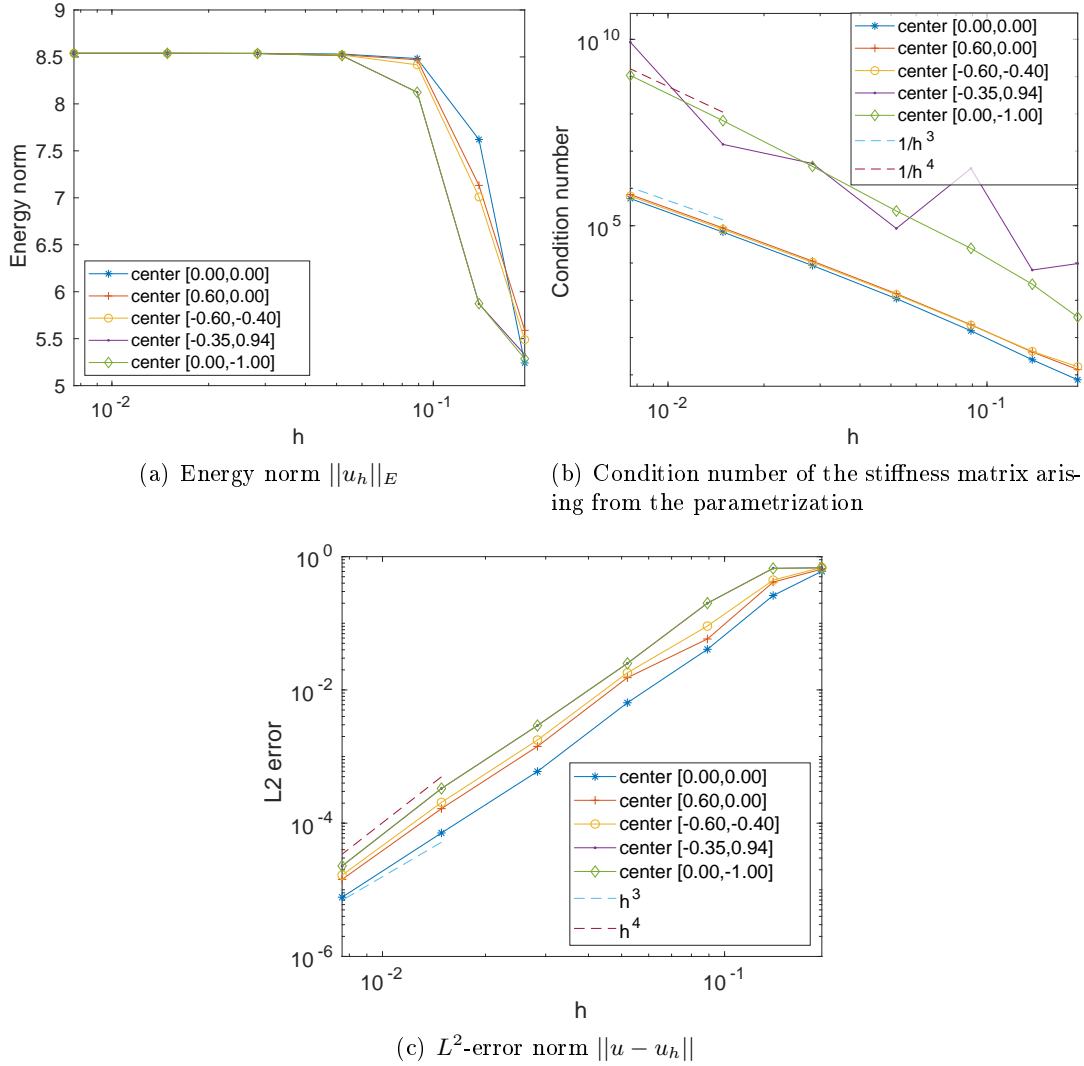


Figure 4.7. Comparison of the energy norm, L^2 -error norm and condition number for the five different SB-parametrizations of the unit disk. From these plots we get an idea on where it is better to put the scaling center. For this geometry the best choice results in its centroid.

(D.4) and (D.5), i.e., when the scaling center lies on the boundary curve, have always the biggest errors and there are no evident differences between these last two cases. The convergence rate for the global L^2 -error is of order between three and four for all the geometries, while in the standard IGA it was almost three (Figure 3.14(b)). So far the best choice for the scaling center is given by the centroid, this is also confirmed when looking at the condition number of the stiffness matrix. Indeed, as shown in Figure 4.19(b), the condition number grows with an order of $1/h^3$ when x_0 is inside the domain and with an order of $1/h^4$ when it is on the boundary. However, for the case (D.4) (a random point on the boundary curve), there is not a clear growth rate for the condition number within 7 iterations. The influence of the parametrization on the accuracy can also be seen in the determinant of the Jacobian of the geometry function (Figure 4.8), where the singularity in the scaling center is depicted by a zero value and, the farther we move the scaling center from the centroid, the bigger the maximum value of the determinant is.

Unlike the standard Galerkin IGA, where we needed spline basis functions of degree

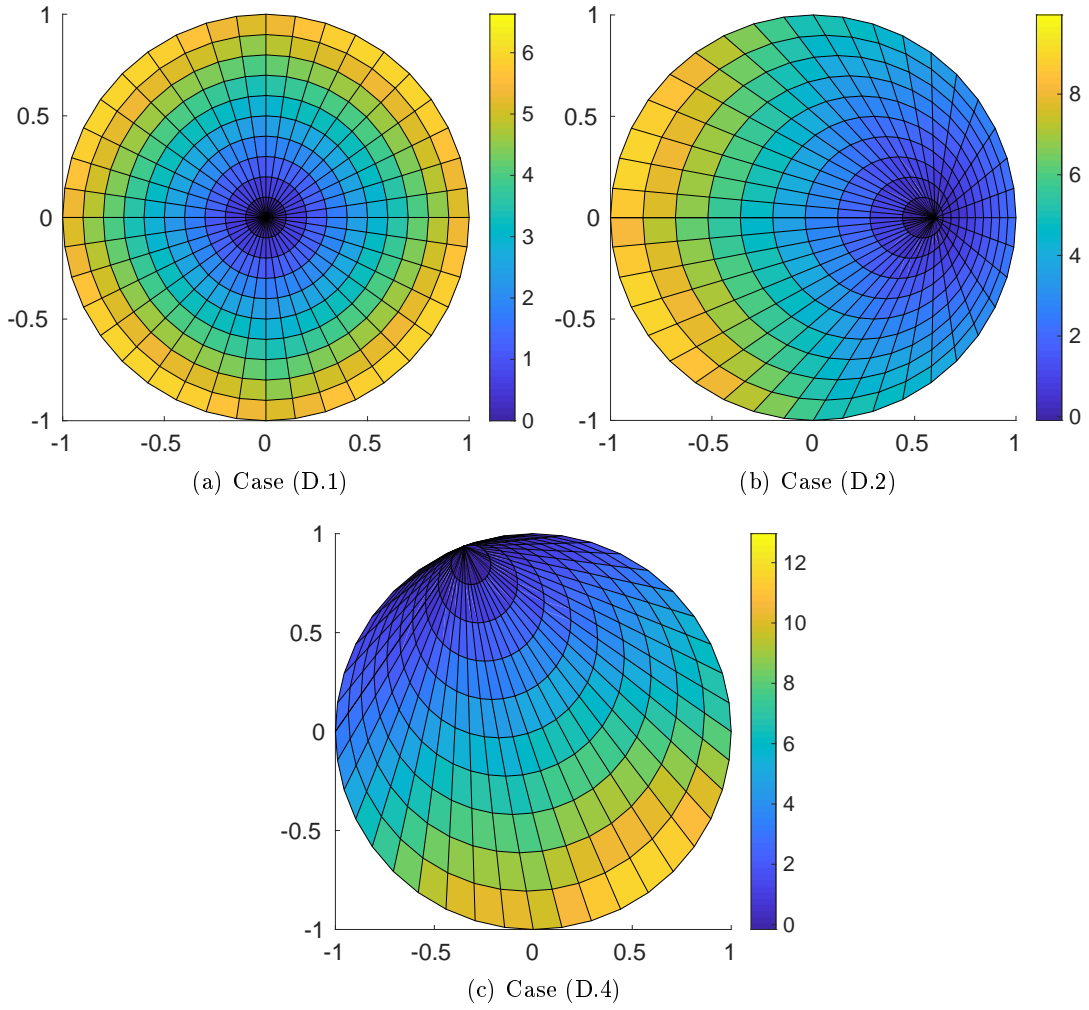


Figure 4.8. Determinant of the Jacobian of the geometry function for the SB-parametrization of the unit disk

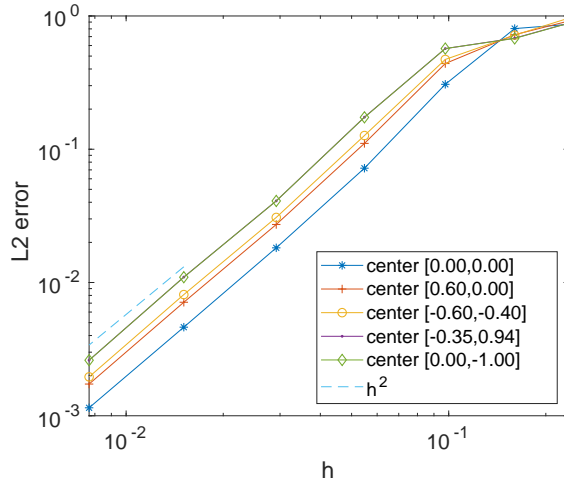


Figure 4.9. Degree 1 in the scaling direction and degree 2 on the boundary curve: L^2 -error norm for the five different SB-parametrizations of the unit disk. The convergence is of order 2.

two in both directions, the SB-IGA can construct the disk using degree $q = 2$ only on the boundary curve and degree $p = 1$ in the scaling direction. However, the order of convergence for the L^2 -error norm will be smaller. Indeed, in this case, the convergence is of order 2, see Figure 4.9. But we did not observe any difference from the case $p = q = 2$ regarding the energy norm and the condition number of the stiffness matrix. Nevertheless, using degree 1 in the scaling direction is slower in approximating numerically a solution with a cosine function inside. Indeed, the error stays high also at the seventh iteration and, to reach the error values obtained with B-splines of degree 2 in the scaling direction, we would have needed more expensive computational costs.

We claim here that for the disk the best choice for the scaling center is the centroid of the kernel, that in the disk coincides with the centroid of the domain. Moreover, for this geometry a SB-parametrization is preferable to the standard parametrization in IGA.

We now consider another star-shaped domain, the L-shape, and we will see if the previous sentences are also true for this kind of geometry.

4.4.2 L-Shape

We consider the L-shape domain seen in Section 3.3.1. In particular, only the boundary curve is available. In this case the boundary is a B-spline curve with degree $q = 2$, knot vector

$$H = \{0, 0, 0, 0.125, 0.125, 0.25, 0.25, 0.5, 0.5, 0.625, 0.625, 0.75, 0.75, 1, 1, 1\}$$

and control points

$$\{\mathbf{c}_j\}_{j=1,\dots,13} = \{(-1, 1), (-1, 0), (-1, -1), (0, -1), (1, -1), \\ (1, -0.5), (1, 0), (0.5, 0), (0, 0), (0, 0.5), (0, 1), (-0.5, 1), (-1, 1)\}.$$

Then we pick a point x_0 inside the kernel of Ω . We choose now seven different scaling centers depicted in Figure 4.10:

$$(L.1) \text{ the centroid of the kernel } (-0.5, -0.5),$$

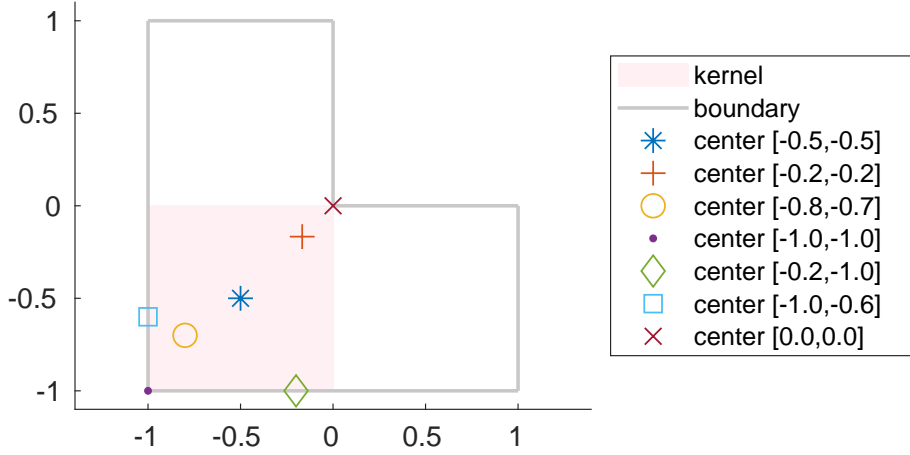


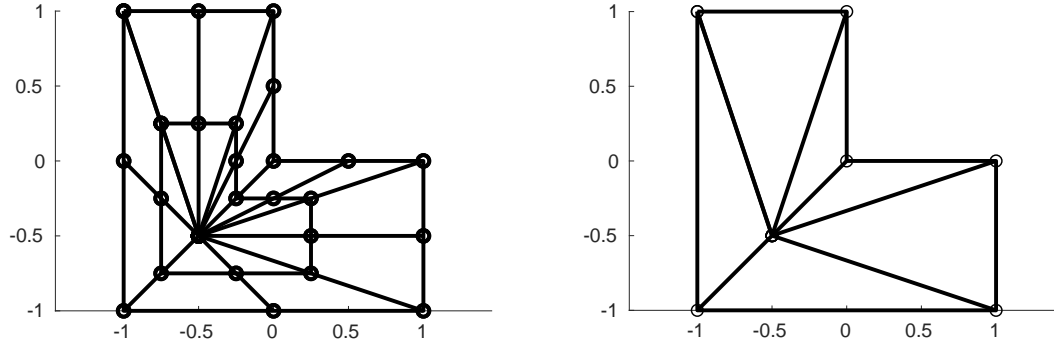
Figure 4.10. Seven different points chosen as scaling center for the L-shape domain. The pink area represents the kernel of this geometry.

- (L.2) the centroid of the domain $(-1/6, -1/6)$,
- (L.3) a random point inside the domain $(-0.8, -0.7)$,
- (L.4) the southwest corner of the kernel $(-1, -1)$,
- (L.5) a point on the south boundary edge of the kernel $(-0.2, -1)$,
- (L.6) a point on the left boundary edge of the kernel $(-1, -0.6)$,
- (L.7) the northeast corner of the kernel $(0, 0)$.

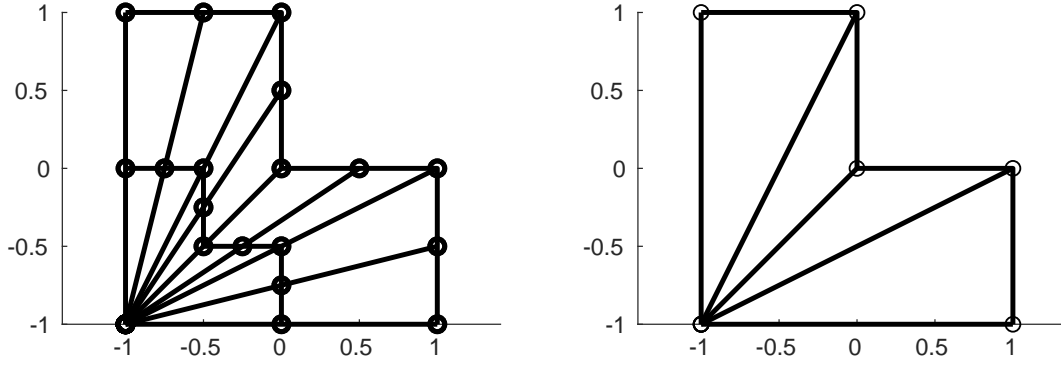
For the first three cases, (L.1),(L.2),(L.3), we construct an SB-parametrization as already done before. We choose for the scaling direction degree $p = 2$, in order to have the same degrees as in the standard IGA example for the L-shape. So the knot vector in the scaling direction is again $\Xi = \{0, 0, 0, 1, 1, 1\}$. The SB-parametrization is then the tensor product of the B-spline boundary curve with the quadratic B-splines in the scaling direction. Dirichlet boundary conditions and periodic conditions are imposed as before. We report now the control points only for one of the first three cases, whose control point grid and the physical domain with the image of knot lines are in Figure 4.17(a).

$$\begin{aligned}
 \text{(L.1)} \quad \{\bar{\mathbf{d}}_{i,j}\}_{i=1,\dots,3,j=1,\dots,13} = & \\
 & \{(-0.50, -0.50) \quad (-0.50, -0.50) \quad (-0.50, -0.50) \quad (-0.50, -0.50) \\
 & (-0.50, -0.50) \quad (-0.50, -0.50) \quad (-0.50, -0.50) \quad (-0.50, -0.50) \\
 & (-0.50, -0.50) \quad (-0.50, -0.50) \quad (-0.50, -0.50) \quad (-0.50, -0.50) \quad (-0.50, -0.50); \\
 & (-0.75, 0.25) \quad (-0.75, -0.25) \quad (-0.75, -0.75) \quad (-0.25, -0.75) \\
 & (0.25, -0.75) \quad (0.25, -0.50) \quad (0.25, -0.25) \quad (0.00, -0.25) \\
 & (-0.25, -0.25) \quad (-0.25, 0.00) \quad (-0.25, 0.25) \quad (-0.50, 0.25) \quad (-0.75, 0.25); \\
 & (-1.00, 1.00) \quad (-1.00, 0.00) \quad (-1.00, -1.00) \quad (0.00, -1.00) \\
 & (1.00, -1.00) \quad (1.00, -0.50) \quad (1.00, 0.00) \quad (0.50, 0.00) \\
 & (0.00, 0.00) \quad (0.00, 0.50) \quad (0.00, 1.00) \quad (-0.50, 1.00) \quad (-1.00, 1.00)\}.
 \end{aligned}$$

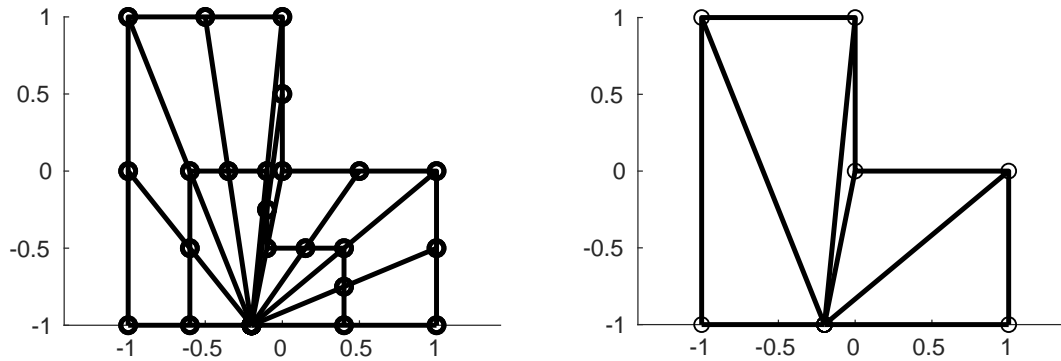
We construct the other cases differently, since the periodic conditions should not be imposed. The only conditions that we will then impose are the Dirichlet boundary



(a) Case (L.1): the scaling center is the centroid of the kernel of the L-shape.



(b) Case (L.4): the scaling center is the southwest corner of the L-shape.



(c) Case (L.5): the scaling center is on the south boundary edge of the kernel.

Figure 4.11. Geometry description of the L-shape using a SB-parametrization: control point grid (left), physical domain with image of knot lines (right)

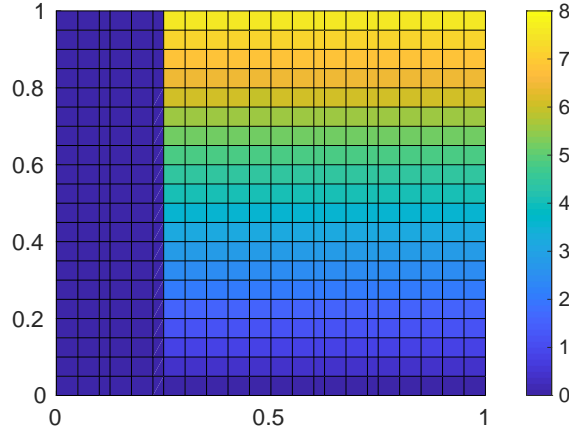


Figure 4.12. Case (L.4) when periodic conditions are also imposed. Determinant of the Jacobian of the stiffness matrix plotted on the parameter domain. In the dark blue area the determinant has value zero.

conditions on the boundary of the domain. Indeed, if we impose periodic conditions when the scaling center is on the edges of the kernel and also on the boundary of the domain, the stiffness matrix is singular. Moreover, the determinant of the Jacobian is zero in a set with positive measure, and so the geometry function is not invertible, see Figure 4.12. This distinction of cases was not necessary in the disk geometry, because the disk does not present any corner. It is however necessary, if we choose as scaling center a point on the boundary of a domain that presents a corner or a crack for example, or in general if the boundary is straight for a finite distance either side of the center. The two straight segments on the boundary passing through the scaling center are known as side faces, and no discretization is there required. Geometries of this type can be found for example in [9, 22, 40].

The size of the knot vectors and the number of control points for the cases (L.5) and (L.6) are the same and we report here the data for (L.5). Same for (L.4) and (L.7), we write the ones for (L.4). Their control point grids are in Figure 4.17(b), 4.17(c).

$$(L.4) \quad p = q = 2, \quad H = \{0, 0, 0, 0.25, 0.25, 0.5, 0.5, 0.75, 0.75, 1, 1, 1\}, \\ \Xi = \{0, 0, 0, 1, 1, 1\}, \quad \{\mathbf{d}_{i,j}\}_{i=1,\dots,3, j=1,\dots,9} =$$

$$\begin{aligned} & \{(-1.00, -1.00) \quad (-1.00, -1.00) \quad (-1.00, -1.00) \quad (-1.00, -1.00) \quad (-1.00, -1.00) \\ & (-1.00, -1.00) \quad (-1.00, -1.00) \quad (-1.00, -1.00) \quad (-1.00, -1.00); \\ & (0.00, -1.00) \quad (0.00, -0.75) \quad (0.00, -0.50) \quad (-0.25, -0.50) \quad (-0.50, -0.50) \\ & (-0.50, -0.25) \quad (-0.50, 0.00) \quad (-0.75, 0.00) \quad (-1.00, 0.00); \\ & (1.00, -1.00) \quad (1.00, -0.50) \quad (1.00, 0.00) \quad (0.50, 0.00) \quad (0.00, 0.00) \\ & (0.00, 0.50) \quad (0.00, 1.00) \quad (-0.50, 1.00) \quad (-1.00, 1.00)\}. \end{aligned}$$

$$(L.5) \quad p = q = 2, \quad H = \{0, 0, 0, 0.25, 0.25, 0.5, 0.5, 0.625, 0.625, 0.75, 0.75, 1, 1, 1\},$$

$$\Xi = \{0, 0, 0, 1, 1, 1\}, \{\bar{\mathbf{d}}_{i,j}\}_{i=1,\dots,3, j=1,\dots,11} =$$

$$\begin{aligned} & \{(-0.20, -1.00) \quad (-0.20, -1.00) \quad (-0.20, -1.00) \quad (-0.20, -1.00) \\ & (-0.20, -1.00) \quad (-0.20, -1.00) \quad (-0.20, -1.00) \quad (-0.20, -1.00) \\ & (-0.20, -1.00) \quad (-0.20, -1.00) \quad (-0.20, -1.00); \\ & (0.40, -1.00) \quad (0.40, -0.75) \quad (0.40, -0.50) \quad (0.15, -0.50) \\ & (-0.10, -0.50) \quad (-0.10, -0.25) \quad (-0.10, 0.00) \quad (-0.35, 0.00) \\ & (-0.60, 0.00) \quad (-0.60, -0.50) \quad (-0.60, -1.00); \\ & (1.00, -1.00) \quad (1.00, -0.50) \quad (1.00, 0.00) \quad (0.50, 0.00) \\ & (0.00, 0.00) \quad (0.00, 0.50) \quad (0.00, 1.00) \quad (-0.50, 1.00) \\ & (-1.00, 1.00) \quad (-1.00, 0.00) \quad (-1.00, -1.00)\}. \end{aligned}$$

We solve on these different parametrizations of the L-shape domain the same problem as in Section 3.3.1, that is

$$\begin{cases} -\Delta u &= 2\pi^2 \sin(\pi x) \sin(\pi y) & \text{in } \Omega, \\ u &= 0 & \text{on } \partial\Omega, \end{cases}$$

whose exact solution is

$$u(x, y) = \sin(\pi x) \sin(\pi y).$$

We compare the energy norm, the L^2 -error norm and the condition number of the stiffness matrix in Figure 4.13. As already observed before, the energy norm of all the parametrizations tends to the same maximum value, that coincides with the one obtained using the standard IGA (Figure 3.6(a)). The fastest parametrization in reaching this value is the case (L.7) (the northeast corner of the kernel), followed by the case (L.2) (the scaling center in the centroid of the domain). The same happens for the L^2 -error norm, where the case (L.7) presents always the smallest error. The convergence has the expected order three in all the parametrizations. Due to presence of the singularity, the condition number has a growth rate of $1/h^3$. In general, we can say that for this geometry the best choice is when the scaling center is in the northeast corner of the kernel, i.e., the inner concave corner of the geometry. Regarding the other cases, it seems that the farther the scaling center is from this northeast corner of the kernel, the slower the error decreases. From the determinant of the Jacobian of the stiffness matrix we do not gain any new information, since the maximum value changes without following a particular behavior, see Figure 4.14.

Unlike the disk, for the L-shape domain we did not observe any big difference in using an SB-parametrization instead of the standard one. But, since the L-shape has straight lines, we can construct this geometry using only linear B-spline basis functions in both the directions. We now compare the two techniques for $p = q = 1$ in Figure 4.15. We have considered three different scaling centers, the ones that performed better in the previous example, and the standard IGA parametrization with an internal C^0 -edge. This last gives better results than the SB-parametrizations. However, since the analytical solution is a product of sine functions, B-spline basis functions of degree only 1 are not really suited to solve the problem. Indeed also after 8 iterations the L^2 -error norm has a value around 10^{-4} .

In general we can claim that, for the L-shape domain, the best choice for the scaling

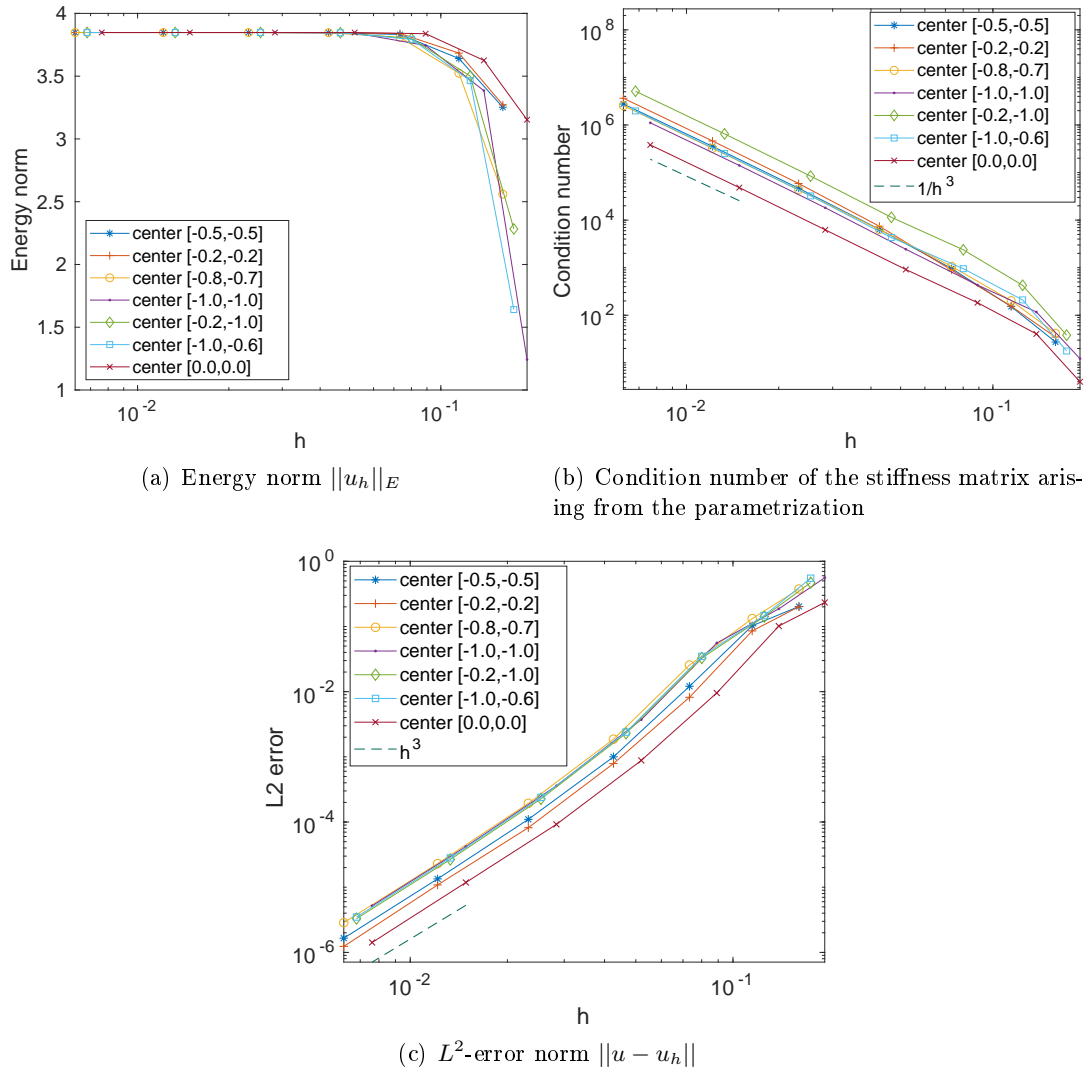


Figure 4.13. Comparison of the energy norm, L^2 -error norm and condition number for the seven different SB-parametrizations of the L-shape. For this geometry the best choice results in the northeast corner of the kernel.

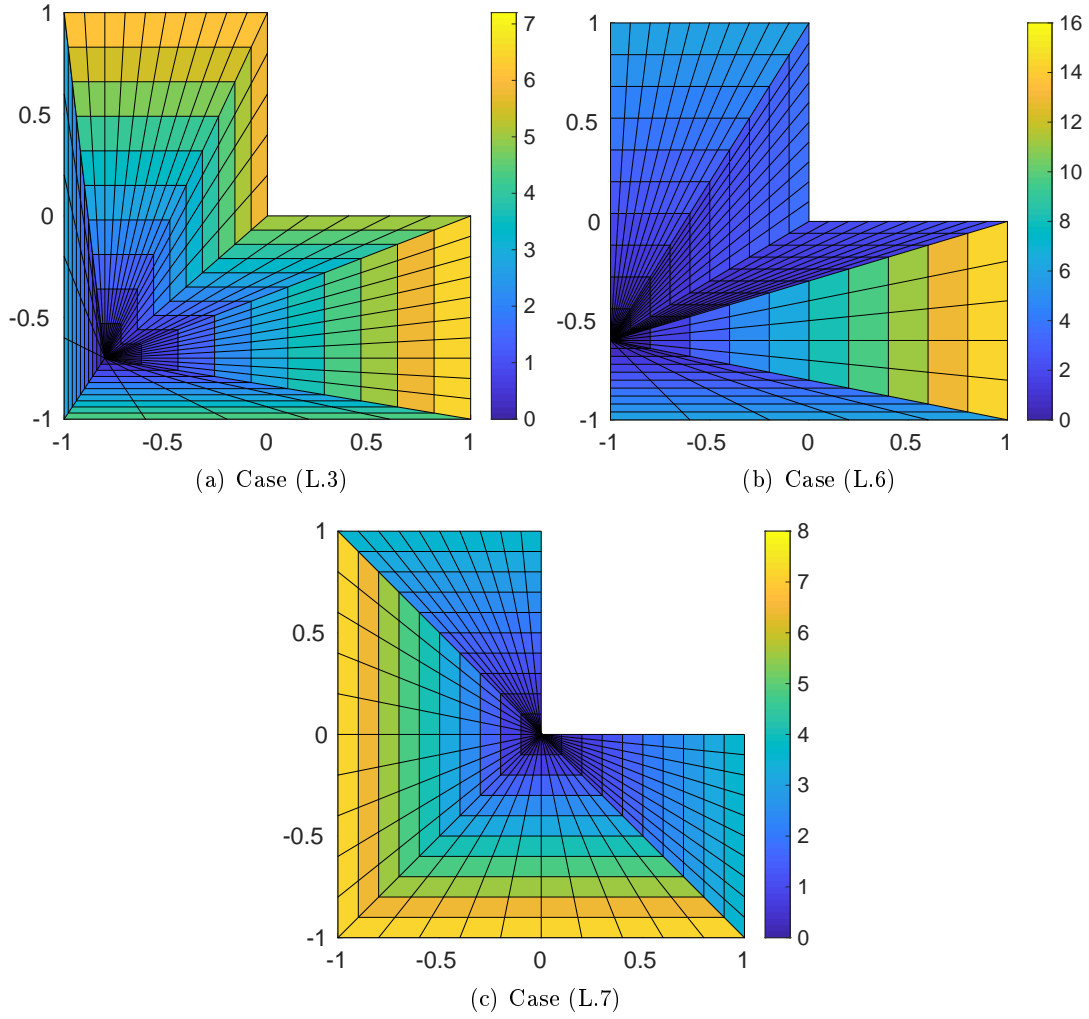


Figure 4.14. Determinant of the Jacobian of the geometry function for the SB-parametrizations of the L-shape

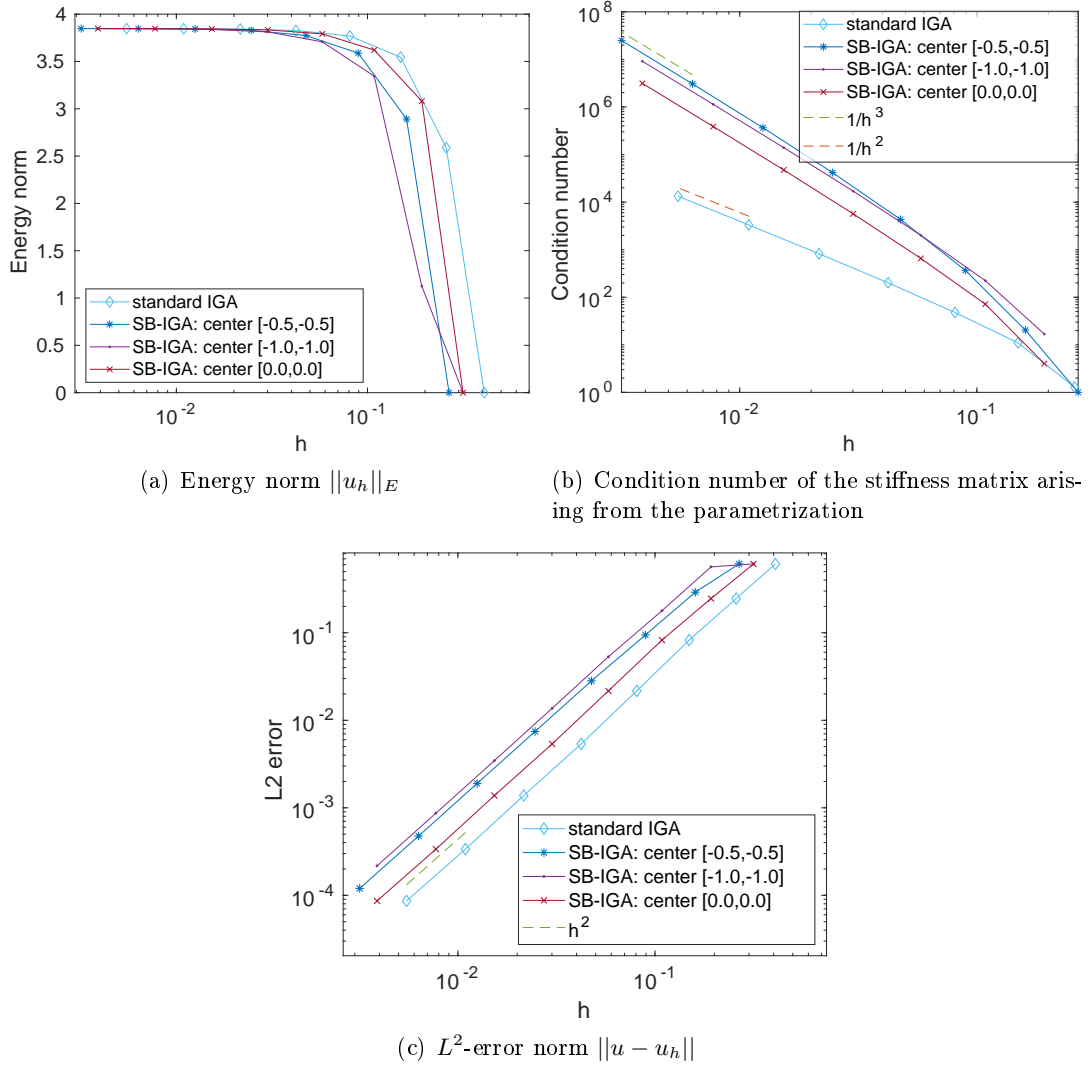


Figure 4.15. $p = q = 1$: comparison of the energy norm, L^2 -error norm and condition number of the stiffness matrix on the L-shape domain between the standard Galerkin IGA and the SB-IGA

center of an SB-parametrization is not a special point such as a centroid, but the north-east corner of the kernel. Moreover, for this geometry the standard parametrization is slightly better than a scaled boundary one.

4.4.3 Wedge-Shape

As final example, we consider a wedge-shape domain as in Figure 4.16. This domain combines straight segments with curved ones, that is, two straight lines are connected at one extremity, while the other ones are connected with a curve. It is clear that, for this geometry, it is much easier to construct an SB-parametrization than a standard one. As boundary curve of the domain we consider a B-spline curve of degree $q = 2$, with knot vector

$$H = \{0, 0, 0, 1/11, 1/11, 3/11, 3/11, 5/11, 6/11, 7/11, 8/11, 9/11, 10/11, 1, 1, 1\}$$

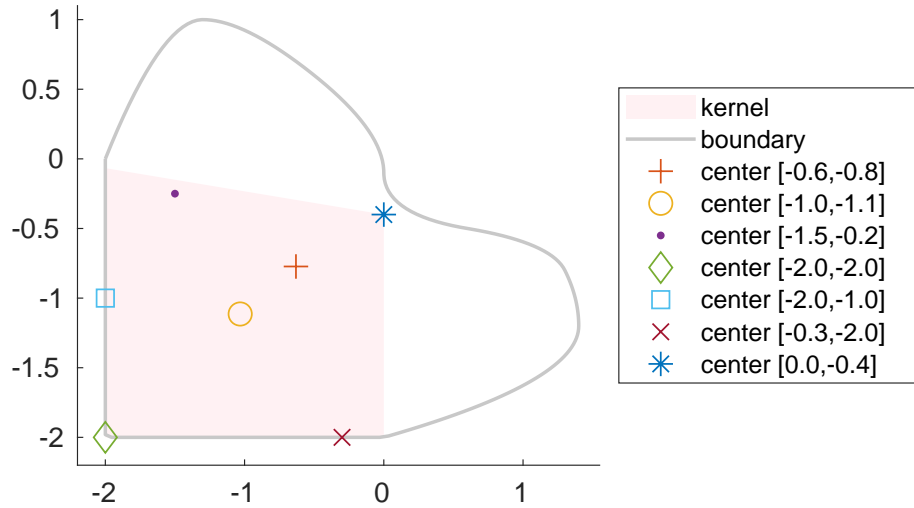


Figure 4.16. Seven different points chosen as scaling center for the wedge-shape domain. The pink area represents the kernel of this geometry.

and control points

$$\{\mathbf{c}_j\}_{j=1,\dots,13} = \{(-2, 0), (-2, -1), (-2, -2), (-1, -2), (0, -2), (1.4, -1.6), (1.4, -1), (1.2, -0.6), (0, -0.4), (0, 0.2), (-1, 1), (-1.6, 1), (-2, 0)\}.$$

Now, we choose seven different points inside the kernel of the domain. These are depicted in Figure 4.16:

- (W.1) the centroid of the domain $\approx (-0.63, -0.77)$,
- (W.2) the centroid of the kernel $\approx (-1.03, -1.11)$,
- (W.3) a random point inside the domain $(-1.5, -0.25)$,
- (W.4) the southwest corner of the kernel $(-2, -2)$,
- (W.5) a point on the left boundary edge of the kernel $(-2, -1)$,
- (W.6) a point on the south boundary edge of the kernel $(-0.3, -2)$,
- (W.7) the northeast corner of the kernel $(0, -0.4)$.

The construction of the SB-parametrization depends on where the scaling center is located. If it is inside the domain (cases (W.1), (W.2), (W.3), (W.7)), Dirichlet boundary conditions and periodic conditions are imposed. If it is on the boundary of the domain (cases (W.4), (W.5), (W.6)), we have two side faces that do not need a discretization and only Dirichlet boundary conditions are imposed, as we have already seen for the L-shape domain. In these last three cases the dimension of the knot vector H is 12, 14, 14, respectively.

In all the cases we choose degree $p = 2$ in the scaling direction. So the knot vector in this direction is $\Xi = \{0, 0, 0, 1, 1, 1\}$. We report now the control points for three of these seven cases, whose control point grids and physical domains with the image of knot lines are in Figure 4.17.

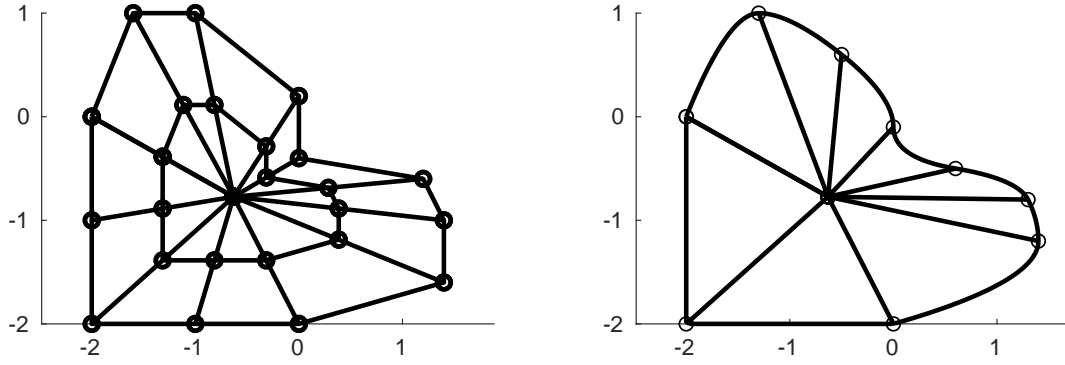
$$\begin{aligned}
 \text{(W.1)} \quad H &= \{0, 0, 0, 1/11, 1/11, 3/11, 3/11, 5/11, 6/11, 7/11, 8/11, 9/11, 10/11, 1, 1, 1\}, \\
 \{\bar{\mathbf{d}}_{i,j}\}_{i=1,\dots,3, j=1,\dots,13} &= \\
 &\{(-0.63, -0.77) \quad (-0.63, -0.77) \quad (-0.63, -0.77) \quad (-0.63, -0.77) \\
 &\quad (-0.63, -0.77) \quad (-0.63, -0.77) \quad (-0.63, -0.77) \quad (-0.63, -0.77) \\
 &\quad (-0.63, -0.77) \quad (-0.63, -0.77) \quad (-0.63, -0.77) \quad (-0.63, -0.77) \quad (-0.63, -0.77); \\
 &\quad (-1.32, -0.39) \quad (-1.32, -0.89) \quad (-1.32, -1.39) \quad (-0.82, -1.39) \\
 &\quad (-0.32, -1.39) \quad (0.38, -1.19) \quad (0.38, -0.89) \quad (0.28, -0.69) \\
 &\quad (-0.32, -0.59) \quad (-0.32, -0.29) \quad (-0.82, 0.11) \quad (-1.12, 0.11) \quad (-1.32, -0.39); \\
 &\quad (-2.00, 0.00) \quad (-2.00, -1.00) \quad (-2.00, -2.00) \quad (-1.00, -2.00) \\
 &\quad (0.00, -2.00) \quad (1.40, -1.60) \quad (1.40, -1.00) \quad (1.20, -0.60) \\
 &\quad (0.00, -0.40) \quad (0.00, 0.20) \quad (-1.00, 1.00) \quad (-1.60, 1.00) \quad (-2.00, 0.00)\}.
 \end{aligned}$$

$$\begin{aligned}
 \text{(W.4)} \quad H &= \{0, 0, 0, 1/7, 2/7, 3/7, 4/7, 5/7, 6/7, 1, 1, 1\}, \\
 \{\bar{\mathbf{d}}_{i,j}\}_{i=1,\dots,3, j=1,\dots,9} &= \\
 &\{(-2.00, -2.00) \quad (-2.00, -2.00) \quad (-2.00, -2.00) \quad (-2.00, -2.00) \\
 &\quad (-2.00, -2.00) \quad (-2.00, -2.00) \quad (-2.00, -2.00) \quad (-2.00, -2.00) \quad (-2.00, -2.00); \\
 &\quad (-1.00, -2.00) \quad (-0.30, -1.80) \quad (-0.30, -1.50) \quad (-0.40, -1.30) \\
 &\quad (-1.00, -1.20) \quad (-1.00, -0.90) \quad (-1.50, -0.50) \quad (-1.80, -0.50) \quad (-2.00, -1.00); \\
 &\quad (0.00, -2.00) \quad (1.40, -1.60) \quad (1.40, -1.00) \quad (1.20, -0.60) \\
 &\quad (0.00, -0.40) \quad (0.00, 0.20) \quad (-1.00, 1.00) \quad (-1.60, 1.00) \quad (-2.00, 0.00)\}.
 \end{aligned}$$

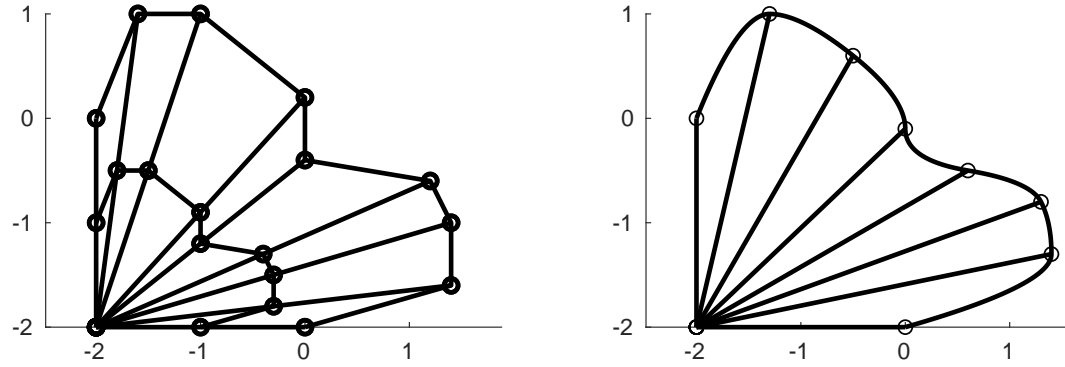
$$\begin{aligned}
 \text{(W.5)} \quad H &= \{0, 0, 0, 1/9, 2/9, 3/9, 4/9, 5/9, 6/9, 7/9, 8/9, 1, 1, 1\}, \\
 \{\bar{\mathbf{d}}_{i,j}\}_{i=1,\dots,3, j=1,\dots,11} &= \\
 &\{(-2.00, -1.00) \quad (-2.00, -1.00) \quad (-2.00, -1.00) \quad (-2.00, -1.00) \\
 &\quad (-2.00, -1.00) \quad (-2.00, -1.00) \quad (-2.00, -1.00) \quad (-2.00, -1.00) \\
 &\quad (-2.00, -1.00) \quad (-2.00, -1.00) \quad (-2.00, -1.00); \\
 &\quad (-2.00, -1.50) \quad (-1.50, -1.50) \quad (-1.00, -1.50) \quad (-0.30, -1.30) \\
 &\quad (-0.30, -1.00) \quad (-0.40, -0.80) \quad (-1.00, -0.70) \quad (-1.00, -0.40) \\
 &\quad (-1.50, 0.00) \quad (-1.80, 0.00) \quad (-2.00, -0.50); \\
 &\quad (-2.00, -2.00) \quad (-1.00, -2.00) \quad (0.00, -2.00) \quad (1.40, -1.60) \\
 &\quad (1.40, -1.00) \quad (1.20, -0.60) \quad (0.00, -0.40) \quad (0.00, 0.20) \\
 &\quad (-1.00, 1.00) \quad (-1.60, 1.00) \quad (-2.00, 0.00)\}.
 \end{aligned}$$

For the test problem on the wedge-shape domain we use a manufactured solution, a bump function with center in $(-1, -1)$ and radius $r = 1/2$:

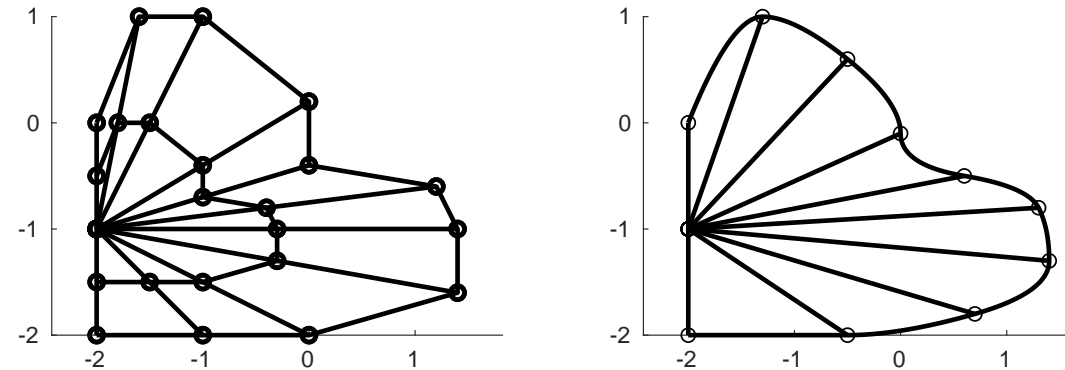
$$u^*(x, y) = \begin{cases} \exp\left(-\frac{1}{1-d^2}\right), & \text{with } d = \frac{\sqrt{(x+1)^2 + (y+1)^2}}{r}, \text{ for } |d| < 1, \\ 0, & \text{elsewhere.} \end{cases}$$



(a) Case (W.1): the scaling center is the centroid of the wedge-shape.



(b) Case (W.4): the scaling center is the southwest corner of the kernel.



(c) Case (W.5): the scaling center is on the left boundary edge of the kernel.

Figure 4.17. Geometry description of the wedge-shape domain using an SB-parametrization: control point grid (left), physical domain with image of knot lines (right)

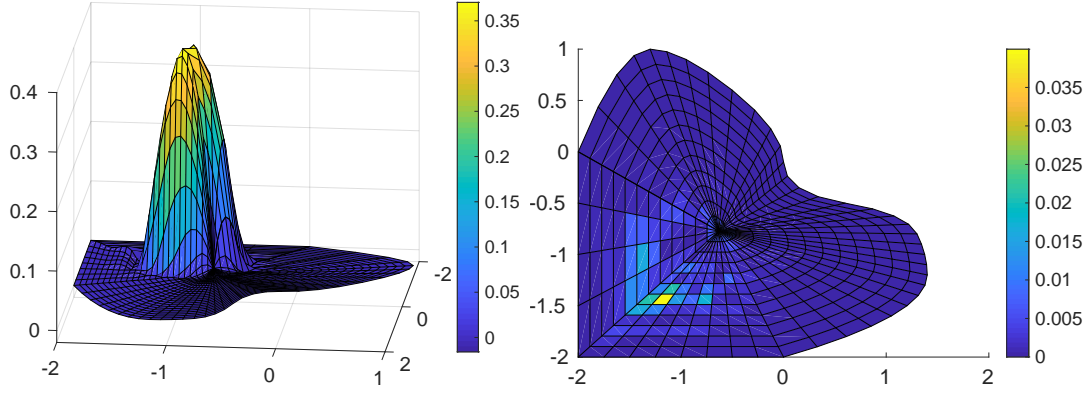


Figure 4.18. Case (W.1): numerical solution (left) and absolute error (right) on the wedge-shape domain after three refinements

The function u^* obviously fulfills the system

$$\begin{cases} -\Delta u = -\Delta u^* & \text{in } \Omega, \\ u = 0 & \text{on } \partial\Omega. \end{cases} \quad (4.47)$$

In Figure 4.18 we plot the numerical solution and the absolute error for the case (W.1). For all the other cases they are similar.

Figure 4.19 depicts the simulation results. All the parametrizations show optimal convergence rates of order three for the global L^2 -error norm. The best choice seems to be the case (W.1), i.e., when the scaling center is in the centroid of the domain. It is important to notice that, even though the case (W.2) has the closest point to the center of the bump function, this is not the best choice. This guarantees us that the position of the bump function in the domain does not influence the results that we have obtained. As expected the energy norm of all the parametrizations converges to the same value. The condition number has a growth rate of $1/h^3$, except for the last case (W.7), where it has rate $1/h^4$. However we cannot explain why the condition number of this last case behaves differently. We can just observe that the determinant of the Jacobian has bigger values in this last case. Moreover, there is not a general trend regarding the determinant, since the smallest maximum value is for the case (W.5). In Figure 4.20 these determinants have been plotted for four cases.

We construct for the wedge-shape domain also a standard parametrization, in order to solve the problem (4.47) with the standard Galerkin IGA and compare it with the results just obtained. It has to be said that the construction of such parametrization for a wedge-shape domain is less natural than a scaled one. Indeed, it was trickier to construct, since the usage of open knot vectors leads up to associate the curved segment to only one edge of the parameter domain. While the two straight lines are associated to the remaining three edges of the parameter domain. We consider degree two in both directions, $p, q = 2$, and knot vectors $\Xi = \{0, 0, 0, 1, 1, 1\}$ and $H = \{0, 0, 0, 1/7, 2/7, 3/7, 4/7, 5/7, 6/7, 1, 1, 1\}$.

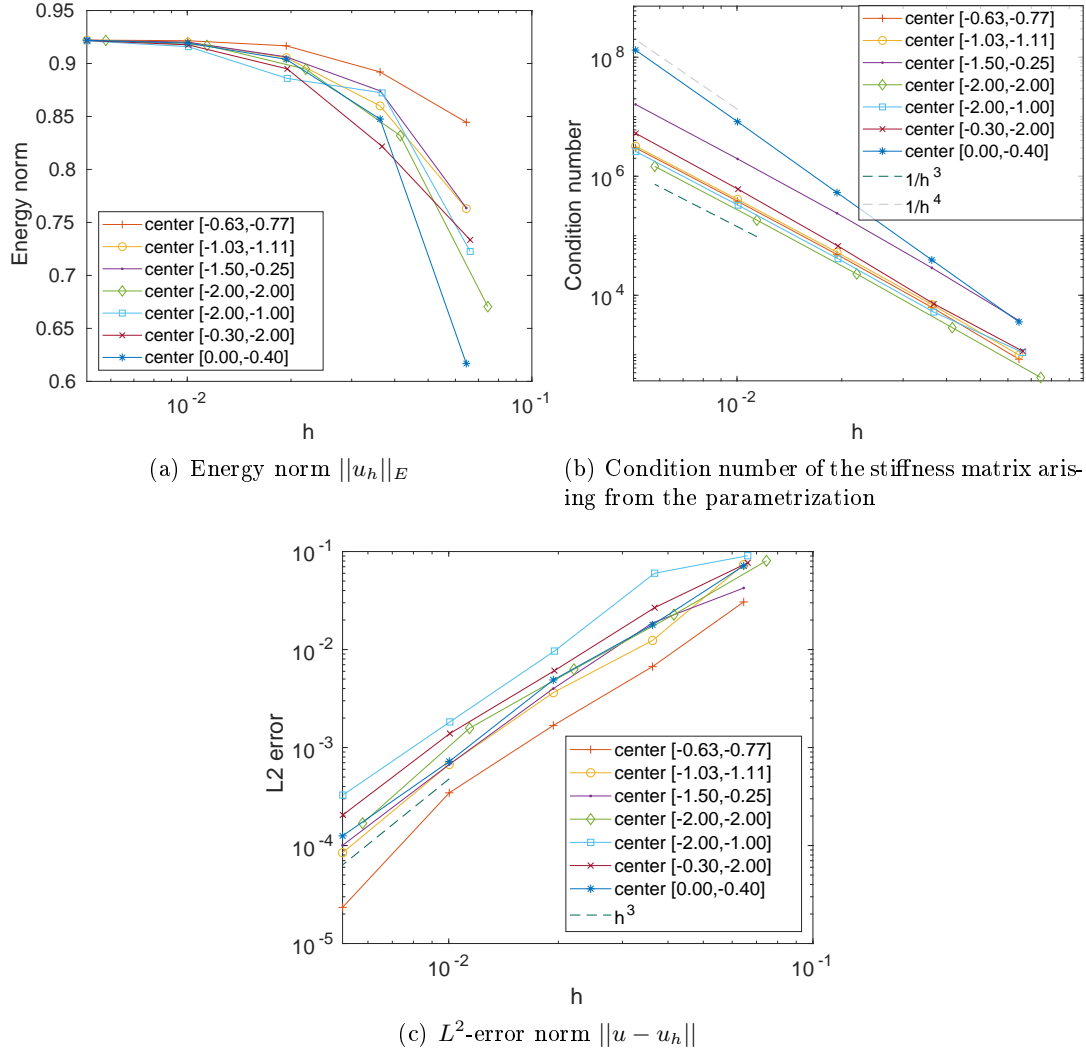


Figure 4.19. Comparison of the energy norm, L^2 -error norm and condition number for the seven different SB-parametrizations of the wedge-shape. For this geometry the best choice results in the centroid of the domain.

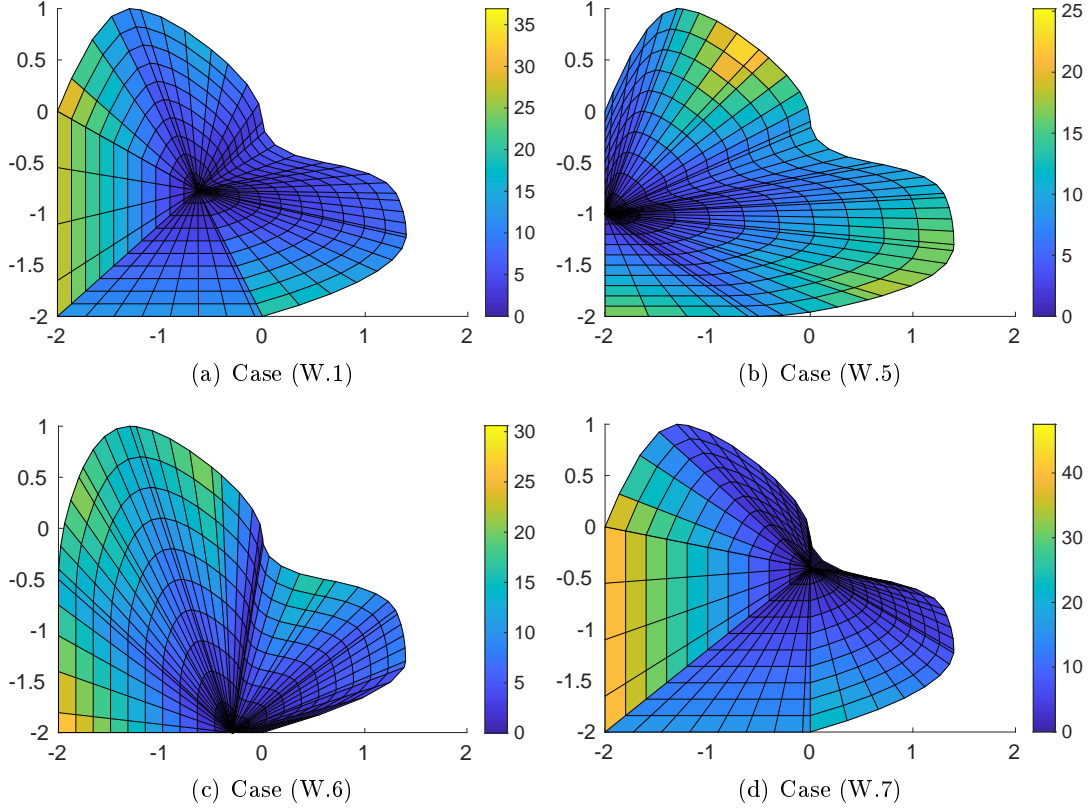


Figure 4.20. Determinant of the Jacobian of the geometry function for the SB-parametrizations of the wedge-shape

The control points are

$$\begin{aligned} &\{(-2.00, -0.50) \quad (-2.00, -1.00) \quad (-2.00, -1.50) \quad (-2.00, -1.85) \\ &\quad (-2.00, -2.00) \quad (-2.00, -2.00) \quad (-1.50, -2.00) \quad (-1.00, -2.00) \quad (-0.50, -2.00); \\ &\quad (-2.00, -0.25) \quad (-1.80, 0.00) \quad (-1.50, -0.25) \quad (-1.00, -0.83) \\ &\quad (-1.00, -1.20) \quad (-0.40, -1.30) \quad (-0.05, -1.50) \quad (0.20, -1.80) \quad (-0.25, -2.00); \\ &\quad (-2.00, 0.00) \quad (-1.60, 1.00) \quad (-1.00, 1.00) \quad (0.00, 0.20) \\ &\quad (0.00, -0.40) \quad (1.20, -0.60) \quad (1.40, -1.00) \quad (1.40, -1.60) \quad (0.00, -2.00)\}. \end{aligned}$$

In Figure 4.21 the control point grid and the physical domain with image of knot lines have been plotted. The errors and the condition number of the stiffness matrix are in Figure 4.22. The energy norm converges to the same value seen in Figure 4.19(a) for the SB-parametrization. While the condition number has the same convergence rate, $1/h^3$. This rate derives from the fact that a singularity occurs in the parametrization. Indeed, in the construction of the standard parametrization a control point had multiplicity two, the corner $(-2, -2)$. Moreover, in other two points there is a singularity, as depicted in Figure 4.23, where we have plotted the determinant of the Jacobian of the stiffness matrix. These points are the control points $(-0.5, -2)$ and $(-2, -0.5)$. The L^2 -error norm has the expected convergence rate of order three. If we compared the value at the mesh-size $h \approx 5 \cdot 10^{-3}$, we can see that the L^2 -error norm for the standard parametrization is approximately $2 \cdot 10^{-4}$, that was one of the value obtained in one of the worst cases for the SB-parametrization at that mesh-size. Indeed, the best case had error equal to circa $2 \cdot 10^{-5}$ for $h \approx 5 \cdot 10^{-3}$.

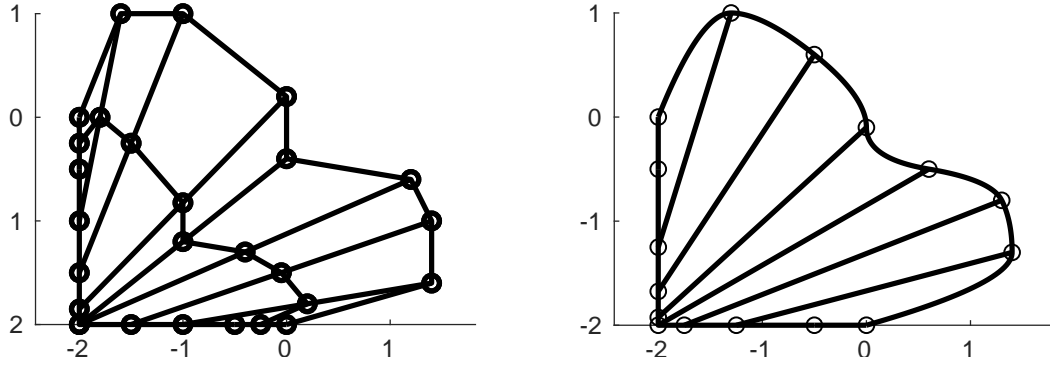


Figure 4.21. Geometry description of the wedge-shape using a standard parametrization: control point grid (left), physical domain with image of knot lines (right)

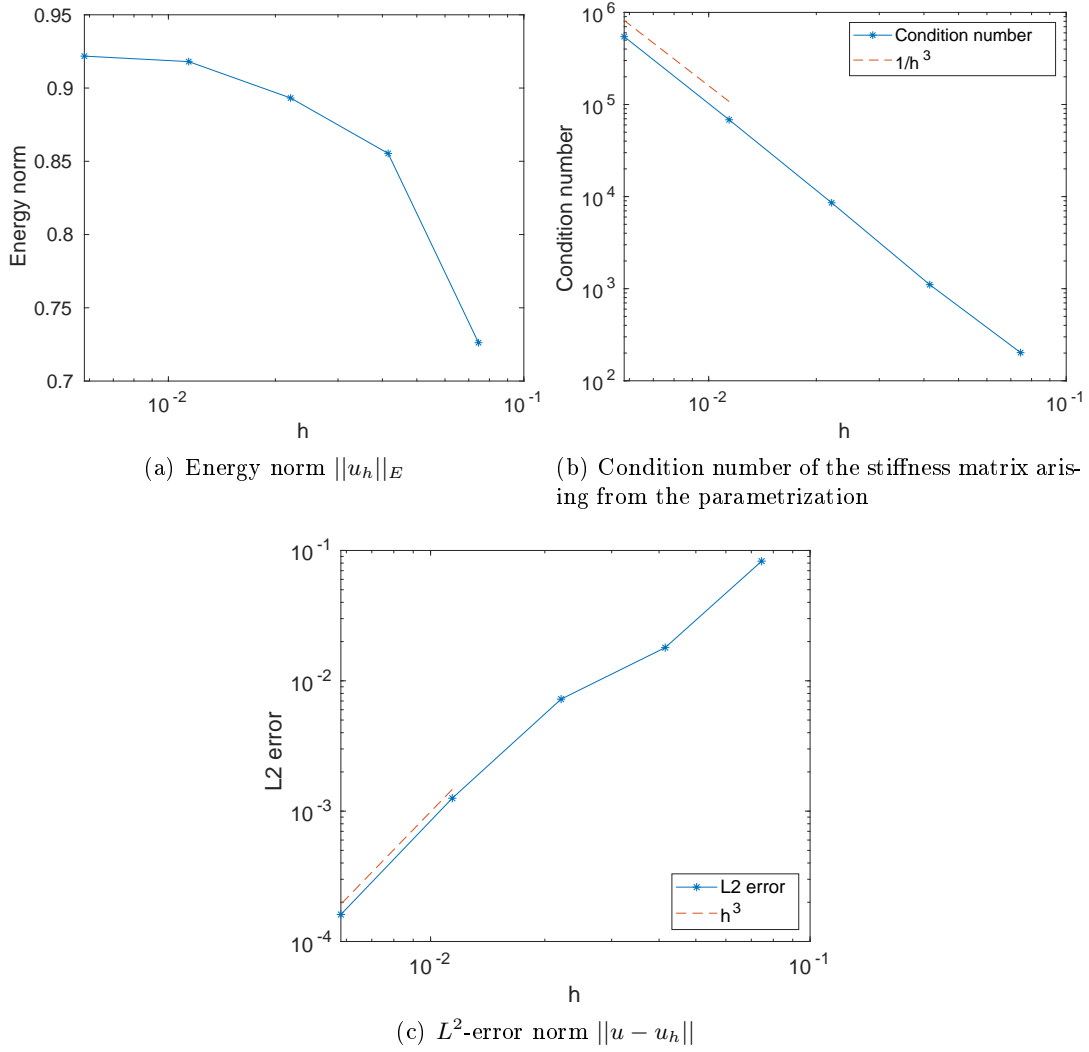


Figure 4.22. Energy norm, L^2 -error norm and condition number for the standard parametrization of the wedge-shape

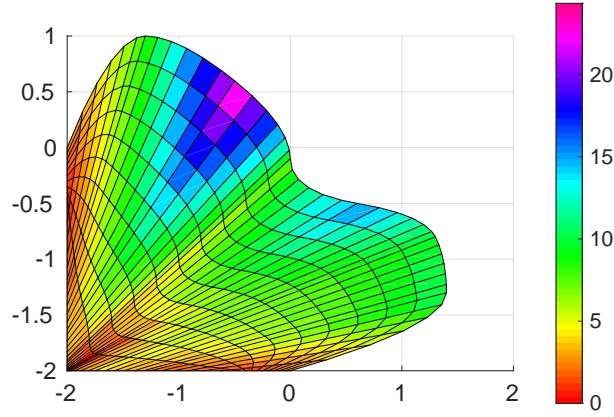


Figure 4.23. Determinant of the Jacobian of the geometry function for the standard parametrization of the wedge-shape

4.4.4 Summary

In the previous examples we have constructed different SB-parametrizations moving the scaling center in the kernel of the domain. Then we have compared for which center the L^2 -error norm had smaller values. We did not notice a general rule for the choice of the scaling center. However, we can observe that, if the centroid of the domain is inside the kernel, this can be a good scaling center. In two of our examples it was the best choice, while for the L-shape domain we could achieve good results even if it was not the best. Furthermore, points on the edges of the kernel that are also on the boundary of the domain should be avoided, since the errors are larger and the condition number of the stiffness matrix could have a larger growth rate.

All the geometries that we have considered were star-shaped, as it was required by the SB-IGA. However, to overcome this limitation, new strategies have been recently proposed. For example, in [35] they propose to increase the flexibility of a polar parametrization by considering circular arcs that connect the center with the points on the boundary of the domain. Another option would be to divide the initial domain into patches such that each subdomain is star-shaped. In [5] the domain decomposition is done with two techniques, the first one is based on the quadtree decomposition and the second one on the art gallery problem.

Conclusion

Finally, we conclude this thesis with a summary of the main points. We have introduced the basic concepts of isogeometric analysis, focusing on the usage of a Galerkin projection method for the discretization step. We have seen that the physical domain is parametrized through a geometry function that goes from the parameter domain, e.g. the unit square or the unit cube, to the physical one. We also gave some insights on a priori error estimates. We presented an interesting class of parametrizations not so widely used in IGA, the scaled boundary parametrizations. These can be seen as a generalization of the classical polar coordinates and they are particularly attractive since objects in CAGD are usually defined by a boundary representation, where only the information related to the boundary is stored. Indeed, an SB-parametrization constructs the mesh inside the domain considering the rays going from a chosen point in the kernel to points on the boundary. We defined then the geometry function for such parametrizations and we studied a standard Galerkin-based IGA in combination with them. At the same time, we introduced the scaled boundary IGA that differs from a standard approach in the derivation of the weak form of the problem. However, for a linear problem we showed that these methods lead to the same weak form in parametric coordinates and we stated an equivalence theorem also for the discretized linear system, having used a Galerkin projection in the finite-dimensional space. Furthermore, we studied the singularity of the parametrization in the scaling center. Actually, we noticed that there is no singularity in the treatment of the integrals of the weak form, both analytically and with a semi-discretization approach. Moreover, also in the numerical integration, the computation of the stiffness matrix is not affected by the singularity when a quadrature rule with quadrature points inside the interval of integration is chosen.

In the numerical examples, we have solved Poisson's equation with zero Dirichlet boundary conditions on three different star-shaped geometries: the unit disk, an L-shape and a wedge-shape domain. We parametrized them with an SB-parametrization and with the standard tensor product of B-splines and NURBS. We compared the results looking at the energy norm, the L^2 -error norm and the condition number of the stiffness matrix. We noticed that, for domains that present a natural behavior in being parametrized using a scaled boundary approach, an SB-parametrization performs better, while on the L-shape, for example, the standard parametrization shows better results. Furthermore, the convergence rate for the L^2 -error norm follows the expected theoretical results for both approaches. Even if we considered different SB-parametrizations moving the scaling center in the kernel, we could not get a real answer to which position gives better numerical results. However, we observed that when the centroid of the domain was inside the kernel, it could perform better than

the other centers. This situation does not always happen, so we suggest to choose as scaling center the center of the kernel of the domain. Indeed, from our experience, this point was a reasonable choice and it achieved good numerical results.

There are still many extensions to this work that can be developed. One possibility could be the usage of collocation methods instead of Galerkin methods for the discretization step, as well as a combination of these two techniques. Moreover, we have so far considered solely star-shaped domains. The next step would be to solve the problem with SB-IGA on more complicated geometries that are not star-shaped and that, therefore, require to be subdivided into star-shaped subdomains. At the same time, different linear equations can be taken into account, such as parabolic equations. Also nonlinear problems could be of interest, however the equivalence theorem proved in this thesis might be not valid anymore.

Bibliography

- [1] M. Abramowitz and I. A. Stegun. *Handbook of mathematical functions with formulas, graphs, and mathematical tables*. Dover, New York City, ninth dover printing, tenth GPO printing edition, 1964.
- [2] C. Arioli, A. Shamanskiy, S. Klinkel, and B. Simeon. Scaled boundary parametrizations in isogeometric analysis. *Computer Methods in Applied Mechanics and Engineering*, 349:576 – 594, 2019.
- [3] F. Auricchio, L. Beirão da Veiga, T. J. R. Hughes, A. Reali, and G. Sangalli. Isogeometric collocation methods. *Mathematical Models & Methods in Applied Sciences - M3AS*, 11 2010.
- [4] P. J. Barendrecht. Isogeometric analysis for subdivision surfaces. Master’s thesis, Eindhoven University of Technology, 2013.
- [5] B. Bauer, C. Arioli, and B. Simeon. Generating star-shaped blocks for scaled boundary multipatch IGA. To appear in *Lecture Notes CSE - Isogeometric Analysis and Applications 2018*, Springer.
- [6] Y. Bazilevs, L. Beirão da Veiga, J. A. Cottrell, T. J. R. Hughes, and G. Sangalli. Isogeometric analysis: approximation, stability and error estimates for h -refined meshes. *Mathematical Models and Methods in Applied Sciences*, 16, 11 2011.
- [7] Y. Bazilevs, V. M. Calo, J. A. Cottrell, J. A. Evans, T. J. R. Hughes, S. Lipton, M. A. Scott, and T. W. Sederberg. Isogeometric analysis using T-splines. *Computer Methods in Applied Mechanics and Engineering*, 199:229–263, 01 2010.
- [8] Y. Bazilevs, V. M. Calo, T. J. R. Hughes, and Y. Zhang. Isogeometric fluid-structure interaction: theory, algorithms, and computations. *Computational Mechanics*, 43:3–37, 12 2008.
- [9] M. H. Bazyar and A. Talebi. Scaled boundary finite-element method for solving non-homogeneous anisotropic heat conduction problems. *Applied Mathematical Modelling*, 39(23):7583 – 7599, 2015.
- [10] M. Berger. *A panoramic view of Riemannian geometry*. Springer, 2007.
- [11] W. Boehm. Inserting new knots into B-spline curves. *Computer-Aided Design*, 12(4):199 – 201, 1980.

- [12] H. Brezis. *Functional analysis, Sobolev spaces and partial differential equations*. Universitext. Springer New York, 2010.
- [13] M. Chasapi and S. Klinkel. A scaled boundary isogeometric formulation for the elasto-plastic analysis of solids in boundary representation. *Computer Methods in Applied Mechanics and Engineering*, 333:475–496, 2018.
- [14] L. Chen, W. Dornisch, and S. Klinkel. Hybrid collocation-Galerkin approach for the analysis of surface represented 3D-solids employing SB-FEM. *Computer Methods in Applied Mechanics and Engineering*, 295:268–289, 2015.
- [15] L. Chen, B. Simeon, and S. Klinkel. A NURBS based Galerkin approach for the analysis of solids in boundary representation. *Computer Methods in Applied Mechanics and Engineering*, 305:777–805, 2016.
- [16] F. Cirak, M. Ortiz, and P. Schröder. Subdivision surfaces: a new paradigm for thin-shell finite-element analysis. *International Journal for Numerical Methods in Engineering*, 47, 09 2000.
- [17] J. A. Cottrell, T. J. R. Hughes, and Y. Bazilevs. *Isogeometric analysis: toward integration of CAD and FEA*. Wiley Publishing, 1st edition, 2009.
- [18] J. A. Cottrell, A. Reali, Y. Bazilevs, and T. J. R. Hughes. Isogeometric analysis of structural vibrations. *Computer Methods in Applied Mechanics and Engineering*, 195, 08 2006.
- [19] L. Beirão da Veiga, A. Buffa, G. Sangalli, and R. Vázquez. Mathematical analysis of variational isogeometric methods. *Acta Numerica*, 23:157–287, 2014.
- [20] C. De Boor. *A practical guide to splines; rev. ed.* Applied mathematical sciences. Springer, Berlin, 2001.
- [21] L. Dedè and A. Quarteroni. Isogeometric analysis for second order partial differential equations on surfaces. *Computer Methods in Applied Mechanics and Engineering*, 284:807–834, 2015. Isogeometric Analysis Special Issue.
- [22] A. J. Deeks. Prescribed side-face displacements in the scaled boundary finite-element method. *Computers & Structures*, 82(15):1153 – 1165, 2004.
- [23] T. Elguedj, Y. Bazilevs, V. M. Calo, and T. J. R. Hughes. B-bar and F-bar projection methods for nearly incompressible linear and non linear elasticity and plasticity using higher order NURBS element. *Computer Methods in Applied Mechanics and Engineering*, 197, 02 2008.
- [24] L. C. Evans. *Partial differential equations*. Graduate studies in mathematics. American Mathematical Society, 1998.
- [25] D. Fußeder. *Isogeometric finite element methods for shape optimization*. PhD thesis, TU Kaiserslautern, 10 2015.
- [26] M. H. Gfrerer and M. Schanz. High order exact geometry finite elements for seven-parameter shells with parametric and implicit reference surfaces. *Computational Mechanics*, 12 2018.
- [27] W. J. Gordon and R. F. Riesenfeld. B-spline curves and surfaces. In R. E. Barnhill and R. F. Riesenfeld, editors, *Computer Aided Geometric Design*, pages 95 – 126. Academic Press, 1974.

-
- [28] J. Gravesen, A. Evgrafov, D.-M. Nguyen, and P. Nørtoft. Planar parametrization in isogeometric analysis. In M. Floater, T. Lyche, M.-L. Mazure, K. Mørken, and L. L. Schumaker, editors, *Mathematical Methods for Curves and Surfaces: 8th International Conference, MMCS 2012, Oslo, Norway, June 28 – July 3, 2012, Revised Selected Papers*, pages 189–212. Springer Berlin Heidelberg, 2014.
 - [29] J. Gu, T. Yu, L. Van Lich, T.-T. Nguyen, and T. Q. Bui. Adaptive multi-patch isogeometric analysis based on locally refined B-splines. *Computer Methods in Applied Mechanics and Engineering*, 339, 04 2018.
 - [30] C. Heinrich, B. Simeon, and S. Boschert. A finite volume method on NURBS geometries and its application in isogeometric fluid–structure interaction. *Mathematics and Computers in Simulation*, 82:1645–1666, 05 2012.
 - [31] T. J. R. Hughes. *The finite element method: linear static and dynamic finite element analysis*. Courier Dover Publications, 2000.
 - [32] T. J. R. Hughes, J. A. Cottrell, and Y. Bazilevs. Isogeometric analysis: CAD, finite elements, NURBS, exact geometry and mesh refinement. *Computer Methods in Applied Mechanics and Engineering*, 194(39):4135 – 4195, 2005.
 - [33] T. J. R. Hughes, A. Reali, and G. Sangalli. Efficient quadrature for NURBS-based isogeometric analysis. *Computer Methods in Applied Mechanics and Engineering*, 199(5):301 – 313, 2010. Computational Geometry and Analysis.
 - [34] B. Jüttler, A. Mantzaflaris, R. Perl, and M. Rumpf. On numerical integration in isogeometric subdivision methods for PDEs on surfaces. *Computer Methods in Applied Mechanics and Engineering*, 302:131 – 146, 2016.
 - [35] B. Jüttler, S. Maroscheck, M.-S. Kim, and Q Y. Hong. Arc fibrations of planar domains. *Computer Aided Geometric Design*, 71:105 – 118, 2019.
 - [36] P. Kagan, A. Fischer, and P. Z. Bar-Yoseph. New B-spline finite element approach for geometrical design and mechanical analysis. *International Journal for Numerical Methods in Engineering*, 41:435 – 458, 02 1998.
 - [37] J. Kiendl, K.-U. Bletzinger, J. Linhard, and R. Wüchner. Isogeometric shell analysis with Kirchhoff–Love elements. *Computer Methods in Applied Mechanics and Engineering*, 198(49):3902 – 3914, 2009.
 - [38] S. Larsson and V. Thomée. *Partial differential equations with numerical methods*. Texts in applied mathematics. Springer, 2003.
 - [39] P. Li, J. Liu, G. Lin, P. Zhang, and B. Xu. A combination of isogeometric technique and scaled boundary method for the solution of the steady-state heat transfer problems in arbitrary plane domain with Robin boundary. *Engineering Analysis with Boundary Elements*, 82:43–56, 2017.
 - [40] P. Li, J. Liu, G. Lin, P. Zhang, and G. Yang. A NURBS-based scaled boundary finite element method for the analysis of heat conduction problems with heat fluxes and temperatures on side-faces. *International Journal of Heat and Mass Transfer*, 113:764 – 779, 2017.
 - [41] A. Mantzaflaris, B. Jüttler, B. N. Khoromskij, and U. Langer. Low rank tensor methods in Galerkin-based isogeometric analysis. *Computer Methods in Applied Mechanics and Engineering*, 316:1062–1085, 2017.

- [42] A. Mantzaflaris, B. Jüttler, B. N. Khoromskij, and U. Langer. Matrix generation in isogeometric analysis by low rank tensor approximation. In J.-D. Boissonnat, A. Cohen, O. Gibaru, C. Gout, T. Lyche, M.-L. Mazure, and L. L. Schumaker, editors, *Curves and Surfaces*, volume 9213, pages 321–340. LNCS, Springer, 2015.
- [43] S. Natarajan, J. C. Wang, C. Song, and C. Birk. Isogeometric analysis enhanced by the scaled boundary finite element method. *Computer Methods in Applied Mechanics and Engineering*, 283:733–762, 2015.
- [44] D.-M. Nguyen, A. Evgrafov, and J. Gravesen. Isogeometric shape optimization for electromagnetic scattering problems. *Progress in Electromagnetics Research B*, 45:117–146, 2012.
- [45] Q. Pan, G. Xu, G. Xu, and Y. Zhang. Isogeometric analysis based on extended Loop’s subdivision. *Journal of Computational Physics*, 299:731 – 746, 2015.
- [46] Q. Pan, G. Xu, G. Xu, and Y. Zhang. Isogeometric analysis based on extended Catmull–Clark subdivision. *Computers & Mathematics with Applications*, 71(1):105 – 119, 2016.
- [47] L. Piegl and W. Tiller. *The NURBS book (2nd ed.)*. Springer-Verlag, Berlin, Heidelberg, 1997.
- [48] H. Prautzsch and T. Gallagher. Is there a geometric variation diminishing property for B-spline or Bézier surfaces? *Computer Aided Geometric Design*, 9(2):119 – 124, 1992.
- [49] A. Reali and T. J. R. Hughes. An introduction to isogeometric collocation methods. In G. Beer and S. Bordas, editors, *Isogeometric Methods for Numerical Simulation*, pages 173–204. Springer Vienna, Vienna, 2015.
- [50] I. J. Schoenberg. Contributions to the problem of approximation of equidistant data by analytic functions. *Quarterly of Applied Mathematics*, 4(1):45–99, 1946.
- [51] T. Sederberg, J. Zheng, A. Bakenov, and A. Nasri. T-splines and T-NURCCs. *ACM Transactions on Graphics (TOG)*, 22:477–484, 07 2003.
- [52] A. Shamanskiy, M. H. Gfrerer, J. Hinz, and B. Simeon. Isogeometric parametrization inspired by large elastic deformation. *Computer Methods in Applied Mechanics and Engineering*, 363:112920, 2020.
- [53] R. N. Simpson, S. P. A. Bordas, J. Trevelyan, and T. Rabczuk. A two-dimensional isogeometric boundary element method for elastostatic analysis. *Computer Methods in Applied Mechanics and Engineering*, 209-212:87 – 100, 2012.
- [54] C. Song. A matrix function solution for the scaled boundary finite-element equation in statics. *Computer Methods in Applied Mechanics and Engineering*, 193(23):2325–2356, 2004.
- [55] C. Song and J. P. Wolf. The scaled boundary finite-element method—alias consistent infinitesimal finite-element cell method—for elastodynamics. *Computer Methods in Applied Mechanics and Engineering*, 147:329–355, 1997.
- [56] C. Song and J. P. Wolf. The scaled boundary finite-element method—a primer: solution procedures. *Computers & Structures*, 78(1):211–225, 2000.

-
- [57] J. R. Stewart and T. J. R. Hughes. A tutorial in elementary finite element error analysis: a systematic presentation of a priori and a posteriori error estimates. *Computer Methods in Applied Mechanics and Engineering*, 158(1):1 – 22, 1998.
 - [58] I. Stroud. *Boundary representation modelling techniques*. Springer, 2006.
 - [59] T. Takacs and B. Jüttler. Existence of stiffness matrix integrals for singularly parameterized domains in isogeometric analysis. *Computer Methods in Applied Mechanics and Engineering*, 200(49-52):3568–3582, 2011.
 - [60] T. Takacs and B. Jüttler. H2 regularity properties of singular parameterizations in isogeometric analysis. *Graphical Models*, 74(6):361–372, 2012.
 - [61] D. Toshniwal, H. Speleers, R. R. Hiemstra, and T. J. R. Hughes. Multi-degree smooth polar splines: a framework for geometric modeling and isogeometric analysis. *Computer Methods in Applied Mechanics and Engineering*, 316:1005–1061, 2017. Special Issue on Isogeometric Analysis: Progress and Challenges.
 - [62] A.-V. Vuong, C. Giannelli, B. Jüttler, and B. Simeon. A hierarchical approach to adaptive local refinement in isogeometric analysis. *Computer Methods in Applied Mechanics and Engineering*, 200(49):3554 – 3567, 2011.
 - [63] A.-V. Vuong, C. Heinrich, and B. Simeon. ISOGAT: A 2D tutorial MATLAB code for isogeometric analysis. *Computer Aided Geometric Design*, 27(8):644 – 655, 2010. Advances in Applied Geometry.
 - [64] R. Vázquez and A. Buffa. Isogeometric analysis for electromagnetic problems. *IEEE Transactions on Magnetics*, 46(8):3305–3308, Aug 2010.
 - [65] W. A. Wall, M. A. Frenzel, and C. Cyron. Isogeometric structural shape optimization. *Computer Methods in Applied Mechanics and Engineering*, 197(33):2976 – 2988, 2008.
 - [66] P. Wang, J. Xu, J. Deng, and F. Chen. Adaptive isogeometric analysis using rational PHT-splines. *Computer-Aided Design*, 43(11):1438 – 1448, 2011. Solid and Physical Modeling 2011.
 - [67] Z.-P. Wang and S. Turteltaub. Isogeometric shape optimization for quasi-static processes. *International Journal for Numerical Methods in Engineering*, 104(5):347–371, 2015.
 - [68] O. Weeger. *Isogeometric finite element analysis of nonlinear structural vibrations*. PhD thesis, TU Kaiserslautern, 04 2015.
 - [69] G. Xu, M. Li, B. Mourrain, T. Rabczuk, J. Xu, and S. P. A. Bordas. Constructing IGA-suitable planar parameterization from complex CAD boundary by domain partition and global/local optimization. *Computer Methods in Applied Mechanics and Engineering*, 328:175 – 200, 2018.
 - [70] G. Xu, B. Mourrain, R. Duvigneau, and A. Galligo. Parameterization of computational domain in isogeometric analysis: methods and comparison. *Computer Methods in Applied Mechanics and Engineering*, 200(23):2021 – 2031, 2011.

Academic Curriculum Vitae

Oct. 2016 – Aug. 2020	Technische Universität Kaiserslautern, Germany <i>Doctorate in mathematics</i>
Oct. 2014 – Sept. 2016	Università degli studi di Milano-Bicocca, Italy <i>Master in mathematics</i>
Oct. 2015 – Mar. 2016	Technische Universität Kaiserslautern, Germany <i>Erasmus+ programme</i>
Sept. 2011 – Sept. 2014	Università degli studi di Milano-Bicocca, Italy <i>Bachelor in mathematics</i>
Sept. 2006 – July 2011	Liceo scientifico Lorenzo Mascheroni, Bergamo, Italy <i>Scientific high school diploma</i>

Akademischer Lebenslauf

Okt. 2016 – Aug. 2020	Technische Universität Kaiserslautern <i>Promotion in Mathematik</i>
Okt. 2014 – Sept. 2016	Università degli studi di Milano-Bicocca, Italien <i>Masterstudiengang Mathematik</i>
Okt. 2015 – März 2016	Technische Universität Kaiserslautern <i>Erasmus+ Programm</i>
Sept. 2011 – Sept. 2014	Università degli studi di Milano-Bicocca, Italien <i>Bachelorstudiengang Mathematik</i>
Sept. 2006 – Juli 2011	Liceo scientifico Lorenzo Mascheroni, Bergamo, Italien <i>Abitur</i>